CELLULAR STIFFNESS AS A SORTING-COMPATIBLE INDICATOR OF STEM CELL POTENCY

A Dissertation
Presented to
The Academic Faculty

by

Tom Bongiorno

In Partial Fulfillment
of the Requirements for the Degree
Doctor of Philosophy in
Bioengineering

School of Mechanical Engineering
Georgia Institute of Technology
December 2016

CELLULAR STIFFNESS AS A SORTING-COMPATIBLE INDICATOR OF STEM CELL POTENCY

Approved by:

Professor Todd Sulchek, Advisor
School of Mechanical Engineering
Georgia Institute of Technology

Professor John F. McDonald
School of Biology
Georgia Institute of Technology

Professor Wilbur A. Lam
Department of Biomedical Engineering
Georgia Institute of Technology & Emory University School of Medicine

Professor Paula M. Vertino
Department of Radiation Oncology
Emory University School of Medicine

Professor Todd C. McDevitt
Department of Bioengineering and Therapeutic Sciences
University of California, San Francisco

Date Approved: September 22, 2016

I dedicate my thesis work to my family, my fiancée, Jennifer, and my advisor, Todd Sulchek; without their influence, I would not have developed into the researcher I am now. Jennifer and my family were always there to support me throughout my graduate school journey. Dr. Sulchek challenged me to consistently improve my work, especially my experimental design and scientific communication.

ACKNOWLEDGMENTS

- Todd Sulchek, my advisor, for his guidance and support throughout my graduate career.

- The remainder of my committee, Wilbur Lam, Todd McDevitt, John McDonald, and Paula Vertino, for their insight and strategic guidance of my research project.

- Undergraduate research assistants Christine Garcia, Jeremy Gura, Jake Kazlow, and Pri Talwar for their dedication to producing results from challenging research experiments.

- Jena Chojnowski for her experimental assistance with limbal stem cell culture and biomolecular staining.

- Barbara Boyan, Jena Chojnowski, Sarah Griffiths, James Lauderdale, Roman Mezencev, Rene Olivares-Navarrete, and Zvi Schwartz for their invaluable advice on experimental design and feedback on written communication.

- The Sulchek lab, especially Betsy Campbell, Billy Wang, Katie Young, and Patricia Pacheco, for experimental advice and assistance.

- James Wade for assistance with receiver operating characteristic analysis.

- Dwight Chambers for assistance with primer design.

- Emily Jackson-Holms, Chad Glen, Jenna Wilson, and Anh Nguyen for assistance with embryonic stem cell culture.

- Alice Cheng for assistance with scanning electron microscopy.

- Priya Baraniak for helpful discussions on mesenchymal stem cell culture.
- Wenwei Xu for assistance with atomic force microscopy.
- Russ Bell, Bill Campbell, Andrés García, Pam Lin, and Bob Nerem for their mentorship and career guidance.
- Core facilities staff Nadia Boguslavsky, Sommer Durham, Dalia Gulick, and Andrew Shaw for assistance with flow cytometry, PCR, and microscopy.
- The National Science Foundation Integrative Graduate Education and Research Traineeship (IGERT) in stem cell biomanufacturing and the National Institutes of Health NIGMS Biotechnology Training Grant on cell and tissue engineering (T32-GM008433) for financial and professional support.
- The Center for Regenerative Engineering and Medicine (REM), the National Science Foundation, and the National Institutes of Health for research funding.

TABLE OF CONTENTS

LIST OF TABLES

LIST OF FIGURES

SUMMARY

Due to their characteristic properties of self-renewal and differentiation, stem cells hold the capacity to serve as phenotype-specific cell factories for various regenerative medicine and tissue engineering applications. However, current phenotyping techniques, which typically employ multiple surface protein-specific antibodies, are often insufficient to identify or enrich cells of a target phenotype. An improved technique that could select target cells could be used to purify starting cell populations for directed differentiation protocols or to enrich specific terminally differentiated phenotypes for tissue engineering.

The goal of this project is to investigate cellular mechanical parameters as stem cell phenotype markers to complement the currently available biomolecular markers. This objective was accomplished through 1) the establishment of cell stiffness as a single-cell marker of potency in both mesenchymal stem cells, which give rise to cells of the connective tissue, and limbal stem cells, which replenish the cornea, 2) the development of a method to compare cell mechanics and gene expression at the single-cell level, which will enable more detailed studies of the relationships between cell phenotype, mechanics, and structure, and 3) the determination that pluripotent embryonic stem cells, which are softer than their differentiated progeny, can be enriched using a cell stiffness-based microfluidic sorting device, as assessed by potency-related morphological and genetic factors. Ultimately, this project established cell stiffness as a marker of stem cell differentiation in various cell systems, with applications to label-free selection of target cell phenotypes.

CHAPTER I

INTRODUCTION

This chapter begins with an overview of the cell mechanics field. The significance of studying cell mechanics and sorting cell phenotypes based on mechanical properties is then addressed. Finally, an overview of the dissertation is provided.

1.1 A Brief History of Cell Mechanics

Atomic force microscopy (AFM) was invented in 1986 by Binnig, Quate, and Gerber for measurement of attonewton-scale forces and surface imaging [17]. AFM functionality has since been extended to the study of the structure and mechanical properties of biological entities ranging from single nucleic acids and proteins to cells and tissue sections [61, 107].

A great deal of work in stem cell mechanotransduction focuses on the effects of substrate stiffness and biochemistry on differentiation, as well as the forces exerted by cells [8, 46, 52, 64, 141]. In contrast, this work examines endogenous cell stiffness as stem cells differentiate in order to evaluate stiffness as a possible differentiation marker with applications to high-throughput cell identification. Cellular stiffness has been proposed as an indicator of multiple cellular processes, including cancer metastasis [31, 35, 136, 162] and apoptosis [70, 84], as well as stem cell differentiation [24, 101, 106, 112, 139] and differentiation potential [59, 65].

Common techniques to assess cell mechanical properties include micropipette aspiration, optical tweezers, and atomic force microscopy (AFM), which is employed throughout the present work. Micropipette aspiration employs a glass capillary with a diameter smaller than the cell diameter to apply a known negative pressure to a cell. The measurements are tensile and tend to be better representative of membrane

mechanics or localized cell structural mechanics, rather than overall mechanical properties. Optical tweezers employ pairs of microbeads, which are adhered to or partially phagocytosed by a cell. The beads are then optically manipulated and the movements can be calibrated to calculate known applied forces and cell mechanical parameters. AFM was chosen for the purposes of this work, as a method to obtain highly repeatable, compressive mechanics measurements. By attaching a large bead to the AFM cantilever, global mechanics measurements were obtained, which are particularly pertinent to the microfluidic device employed later in the study.

1.2 Research Motivation and Significance

Cell mechanics offer the opportunity for label-free markers that complement existing biomolecular markers. The most common methods to identify phenotype, including RNA-, DNA-, and protein-based methods, are not readily compatible with high-throughput cell sorting. Current sorting-compatible phenotype identification techniques, most commonly fluorescence- or magnetic-activated cell sorting (FACS or MACS), rely on one or multiple antibodies. In turn, the antibodies depend upon the presence of phenotype-specific surface proteins, which can be transient and difficult to identify [39]. The lack of reliable cell-surface or intracellular markers of terminal stem cell differentiation precludes techniques such as fluorescence-activated cell sorting from successful phenotype identification. The use of antibodies to identify stem cells is cumbersome, requiring approximately 15 hours of laborious cell processing, and can subsequently affect cellular physiology if the epitope is associated with a functionally important protein domain [36, 68, 105].

Promising fields, such as tissue engineering and regenerative medicine require advances in cell phenotyping to succeed. Controlling both potency and lineage specification in stem cell-derived cell populations is paramount for tissue engineering and

regenerative medicine. Tissue engineering requires highly pure starting cell populations with fine control over cell position and phenotype. Currently, tissue engineering approaches are generally confined to structurally simple organs containing few cell types, such as the bladder, the first organ to be successfully tissue engineered. To engineer more complex organs from highly proliferative stem cells, strict control over cell phenotype is paramount to match *in vivo* physiology. Thus, methods to identify or enrich target cell phenotypes will be invaluable to the future of tissue engineering.

Regenerative medicine also requires extremely pure starting cell populations and can endanger patients if proper precautions are not taken. Excessive potency can cause dangerous teratomas, whereas deficient potency is associated with low proliferative potential, which can limit the efficacy of a cell therapy [67]. Additionally, lineage specification must be controlled to obtain starting cell populations with sufficient phenotypic purity, which are required to generate functional tissue-engineered organs and efficient cell therapies. Even with extensive efforts to engineer the cellular microenvironment, directed differentiation protocols are generally low yield or time consuming. Thus, a complementary method of phenotype control is important to select target cell types from a heterogeneous population, which requires an understanding of the cell subsets that exist for each selection basis (e.g. gene or protein expression).

After validating biophysical markers as phenotype-specific indicators of cell state, microfluidic technology can be used to enrich for target cell types. Microfluidics can also be used to divide cell populations into biophysical subsets, enabling investigation of the relationship between biological and mechanical subsets of larger populations. Such studies begin to address the confounding mechanical heterogeneity of cell populations and, in the case of stem cell studies, asynchronous differentiation kinetics, which complicate current understanding. Ideally, investigations of single-cell relationships between mechanical properties and traditional biomarkers can be performed to

best determine how effectively individual parameters indicate the differentiation state. The capability to produce subpopulations of naive and differentiated stem cells will enable more accurate study of the biology of differentiation. For example, nuclear restructuring, including chromatin condensation [106, 112, 159] and increased lamin A/C protein expression [106, 112], has been implicated in the ESC differentiation-associated stiffening mechanism. Stiffness changes during differentiation have also been hypothesized to be caused by cytoskeletal rearrangement [117, 142, 165].

The control and understanding of stem cell differentiation through purification of heterogeneous populations will ultimately enable the biomanufacturing of desired differentiated lineages and facilitate the clinical potential of stem cells.

1.3 Dissertation Overview

This dissertation presents cellular stiffness as a means both to identify the potency of stem cells and to sort cells based on potency at the single-cell level, as summarized in Fig. 1.1.

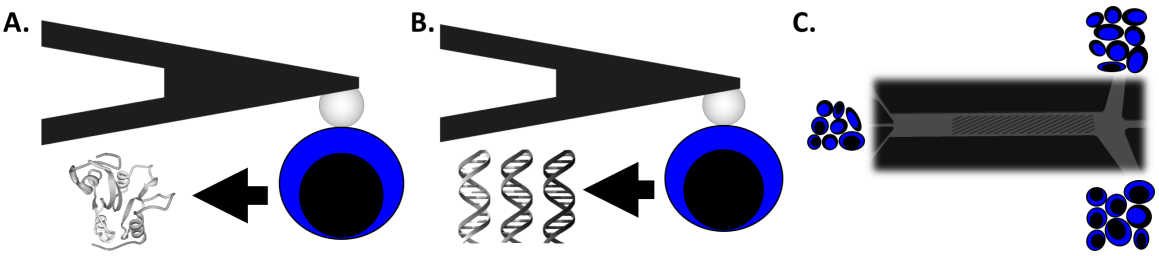

Figure 1.1: Dissertation Overview. A. The relationship between cell mechanics and protein expression was assessed during the differentiation of both mesenchymal stem cells and limbal stem cells. **B.** A new technique, single-cell genomechanics, was created to assess the relationship between gene expression and cell mechanics at the single-cell level. **C.** Microfluidic sorting was employed to enrich pluripotent embryonic stem cells from their differentiated progeny.

Chapter 2 provides background information on stem cell biology and mechanics and establishes the need for additional differentiation biomarkers and sorting methods. Chapter 3 investigates mesenchymal stem cell differentiation to the osteoblast

lineage and demonstrates the use of cellular stiffness as an indicator of differentiation relative to traditional protein markers. Chapter 4 evidences cellular stiffness as a differentiation marker in stem cells from the corneal limbus and employs sensitivity analysis to provide a direct link between differences in cellular stiffness and the ability to sort using a stiffness-based microfluidic device. Chapter 5 details the biophysical characterization of differentiating embryonic stem cells and subsequent mechanics-based microfluidic sorting to enrich for pluripotent cells. Chapter 6 presents a novel method to measure both the mechanics and multiplexed gene expression of individual cells, enabling improved understanding of the relationships among stem cell mechanics, structure, and differentiation.

Chapter 7 summarizes the research findings and concludes with a discussion of technological limitations and directions for future research.

CHAPTER II

BACKGROUND

2.1 Stem Cell Biology

Due to their inherent properties of self-replication and differentiation (Fig. 2.1), stem cells can be engineered to serve as "factories" that produce large numbers of cells of a desired phenotype. Thus, stem cells hold great potential in tissue engineering and patient-specific cell therapy. However, the lack of phenotype-specific molecular markers hinders purification of target cell types for safe and efficient therapeutic technologies. Current markers to identify target phenotypes after differentiation of stem cells are not sufficiently specific to select cells of interest. Selection of specific cell phenotypes will improve tissue engineering and cell therapies that depend on highly pure starting cell populations.

To assess a broad range of potencies, mesenchymal stem cells (MSCs; middle potency), limbal stem cells (LSCs; middle-low potency), and embryonic stem cells (ESCs; high potency) were chosen for study. MSCs are considered multipotent and can differentiate to osteoblasts, adipocytes, chondrocytes, and several other cell types. LSCs are mainly responsible for producing corneal epithelial cells, but may also have the capability of producing buccal cells, skin stem cells, or conjunctiva; thus, it is unclear whether LSCs are considered multipotent or unipotent. ESCs are known to be pluripotent and can differentiate into any somatic cell type.

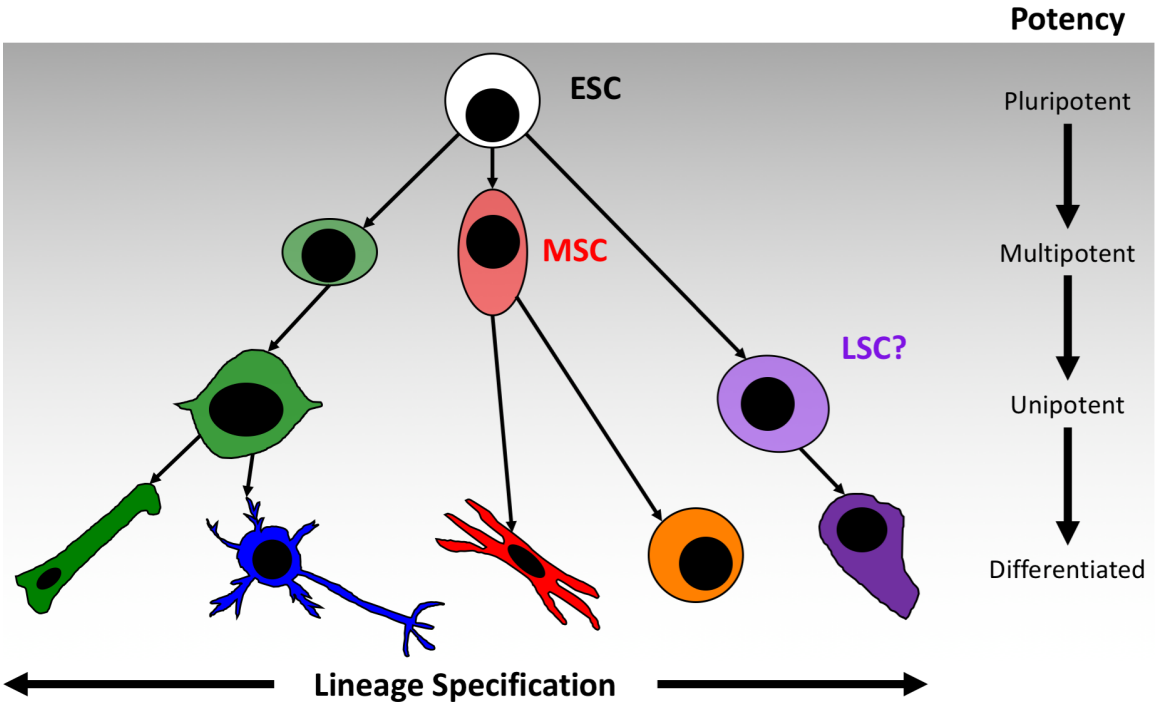

Figure 2.1: Stem Cell Potency. Stem cells range in potency from pluripotent (dark gray) to multipotent (medium gray) to unipotent (light gray) based on the number of cell types to which they can differentiate. As a stem cell differentiates, it specifies into one of many lineages, as represented by different hues.

2.1.1 Mesenchymal Stem Cells

Human mesenchymal stem cells (hMSCs) hold great potential for autologous therapy, highlighted by the properties of immunosuppression, migration to injured tissues, and tissue repair via soluble factor secretion [75]. The immunosuppressive effect exhibited by MSCs reduces the risk of transplant rejection highlighting MSCs as suitable candidates for transplantation to repair damaged tissue [7]. MSC osteoblast differentiation following bone graft incorporation may facilitate subsequent bone formation [4]. Current techniques to isolate MSCs from bone marrow involve removal of non-adherent cells via media change 3 h after plating on polystyrene dishes [129]. Such passive, adhesion-based separation permits only binary control over the removal of undesired cell phenotypes, such as hematopoietic stem cells, and may not result in optimal purity [129].

MSCs can be challenging to scale up, as MSC culturing is limited to about 40 population doublings in vitro. The process is also tedious, as the MSC isolation process requires 3 weeks for completion [129]. Furthermore, the absence of donor- and anatomical location-independent MSC biomarkers hampers MSC collection from bone marrow or adipose tissue for clinical therapies [4], which establishes a need to improve phenotype detection by identifying additional MSC biomarkers. Thus, there exists a need to efficiently purify MSCs from bone marrow or adipose tissue in high throughput in order to achieve the MSC clinical dose, which requires the infusion of on the order of 10^8 cells [91].

2.1.2 Limbal Stem Cells

Limbal stem cells (LSCs) are found in the corneal limbus, which serves as the boundary between the cornea and the sclera. LSCs are responsible for replenishing corneal cells, and LSC deficiency (LSCD) or dysfunction is known to result in reduced eyesight caused by aging, chronic contact lens use, or traumatic injury, typically caused by chemical or laser burns.

LSC tissue therapy is a promising option for restoring eyesight in patients with LSCD. Indeed, Holoclar®, an ex vivo-expanded autologous LSC product, was the first stem cell-based product to be clinically approved in Europe in February 2015. The portion of the tissue graft comprised of stem cells is vitally important to the clinical success of the implant. Patients with low numbers of LSCs in the healthy, contralateral eye may be unable to benefit from the therapy. Thus, methods to improve the number or fraction of LSCs in the implant are needed to improve effectiveness for all patients.

2.1.3 Embryonic Stem Cells

The ability of embryonic stem cells (ESCs) to self-renew and differentiate to virtually all somatic cell types demonstrates fantastic capacity to improve tissue engineering

and regenerative medicine. Efficient differentiation control technologies will permit the use of ESCs as phenotype-specific cell factories to treat diseases characterized by decreased functionality or quantity of a particular cell type [12] through stem cell-enabled regeneration of target tissues, such as articular cartilage [103], bone [25], liver [27], neurons [22], or heart tissue [93]. However, the elusiveness of efficient, directed stem cell differentiation is a prime limitation in the study and therapeutic use of ESCs.

Currently, expression of markers such as SSEA4, OCT4, and Nanog is used to identify pluripotent ESCs within heterogeneously differentiated cell populations. However, these pluripotency markers exhibit significant overlap and highly variable expression [60], highlighting the need for improved differentiation indicators. While expression of pluripotency genes in ESCs has been well studied, markers of specific differentiation lineages are still poorly defined.

Certain methods are successful in moderate enrichment of target phenotype differentiation, but are not scalable to clinical cell quantities [14]. Growth factors or small molecules may be used to direct ESC differentiation, but certain signaling pathways do not have well defined chemical modifiers [12]. Differentiation is a step-wise process, and directed differentiation becomes less efficient with each step [12], highlighting the need to efficiently purify differentiated cells of target lineages, such as pancreatic, cardiac, retinal pigment epithelium, and mechanosensitive hair cells [12].

Contamination of differentiated populations with pluripotent stem cells is a major problem in stem cell biomanufacturing that poses considerable safety concerns, particularly due to the tumorigenicity of pluripotent ESCs [125]. In concert with future advances in directed ESC differentiation, technologies to remove contaminating pluripotent ESCs from differentiated cell populations will potentially reduce teratoma formation, thereby improving the safety and efficiency of clinical stem cell treatments.

Embryonic stem cells (ESCs), which normally grow in suspension, will be used as

a model system to study single-cell correlations between cell mechanics and biological states. ESCs also have well-established pluripotency biomarkers, including Oct4, Nanog, and Sox2. Lamin A is known to both modulate cell stiffness and regulate phenotypic stem cell gene expression [137], implying a connection between differentiation state and cell stiffness. However, the mechanisms underlying these changes are not well understood.

2.2 Stem Cell Mechanics

As an inherent property of individual cells, Young's modulus holds great potential as a single-cell, label-free differentiation biomarker with direct applications to microfluidic cell sorting and phenotype identification. Compared to extracellular protein markers, which are commonly used to distinguish cell phenotype in a sorting context, cellular stiffness is easily attributable to individual cells, and thus may serve as a candidate differentiation marker.

The differentiation potential of adipose-derived stem cells has previously been correlated with cell mechanical properties [59], which serves as a proof-of-concept that cell stiffness may be employed to create pure cells of a desired differentiation state. Furthermore, recent technologies have permitted high throughput probing of cell mechanical properties such as deformability [60] as well as sorting based on cell stiffness [156] or adhesion strength [128]. Continued study is needed to further hone the existing technologies for application to specific identification and enrichment of desired stem cell phenotypes.

Young's modulus is attributable to individual suspended cells, and thus potentially lends itself to phenotypic cell sorting applications. Recent developments in cell separation by adhesion [128] and stiffness [72, 156] indicate future label-free cell sorting capabilities, even where molecular biomarkers are not fully established.

2.3 The Need for Novel Biomarkers and Sorting Methods

Cellular stiffness, an intrinsic cell property, may serve as a novel biomarker that can be used to improve phenotype identification and purification methods, in addition to established molecular biomarkers and cellular morphological indicators. Therefore, the objective of this work is to employ mechanical characterization and microfluidic technology to assay cell mechanical properties and sort heterogeneous cell populations by mechanical stiffness and according to phenotype. The central hypothesis is that differential cell stiffness may be harnessed to obtain enriched populations of desired cell phenotypes. Utilization of cell mechanical properties may represent a novel approach to identify and purify target cells, derived from more potent cells such as embryonic stem cells, even though appropriate phenotypic biomarkers are not well established. Although it has been shown that cellular stiffness can change as a stem cell differentiates, the precise relationship between cell mechanics and other phenotypic properties remains unclear. Single-cell analysis will be employed to determine how changes in cell stiffness correlate with changes in molecular biomarkers during differentiation.

The lack of reliable cell-surface or intracellular phenotype markers precludes current techniques from successful phenotype identification. The efficiency of the widely used affinity-based cell separation methods, such as florescence- and magnetic-activated cell sorting, is limited by the specificity of cell surface differentiation markers [39]. The current phenotype identification methods require well-defined molecular biomarkers, fluorescent-labeled antibodies, and trained scientists to stain the cells and analyze the results. Furthermore, isolation of extracellular matrix constituents, which are commonly used to identify phenotype of large populations of cells, requires dissociative, cell-destructive methods to implement. Thus, locally synthesized proteins are difficult to distinguish from matrix-trapped proteins derived from other sources, such as serum. Altogether, these facts emphasize a need for additional cell-specific markers

to identify cell phenotype.

Therefore, a device that does not rely on cell surface markers was developed to be used in addition to or in replacement of affinity-based methods. Employment of cell stiffness, an intrinsic biophysical marker, as a basis for cell sorting, also circumvents costly antibody labeling and laborious sample preparation. Cell stiffness represents a single, integrated measure of the complicated physiology occurring within a cell and thus offers a unique opportunity to probe complex biology via a single parameter. Microfluidic technology will therefore be utilized to enrich target cell types based on their mechanical properties. Revelation of additional differentiation indicators, such as cell stiffness, can improve identification and collection of starting cell populations, with applications to stem cell-based therapies and tissue engineering.

CHAPTER III

MECHANICAL STIFFNESS AS AN IMPROVED SINGLE-CELL INDICATOR OF OSTEOBLASTIC HUMAN MESENCHYMAL STEM CELL DIFFERENTIATION[1]

3.1 Abstract

Although it has been established that cellular stiffness can change as a stem cell differentiates, the precise relationship between cell mechanics and other phenotypic properties remains unclear. Inherent cell heterogeneity and asynchronous differentiation complicate population analysis; therefore, single-cell analysis was employed to determine how changes in cell stiffness correlate with changes in molecular biomarkers during differentiation. Design of a custom gridded tissue culture dish facilitated single-cell comparisons between cell mechanics and other differentiation biomarkers by enabling sequential measurement of cell mechanics and protein biomarker expression at the single cell level. The Young's modulus of mesenchymal stem cells was shown not only to decrease during chemically-induced osteoblast differentiation, but also to correlate more closely with the day of differentiation than did the relative expression of traditional osteoblast differentiation markers, bone sialoprotein and osteocalcin. Therefore, cell stiffness, a measurable property of individual cells, may serve as an improved indicator of single-cell osteoblast differentiation compared to traditional biological markers. Revelation of additional osteoblast differentiation indicators, such as cell stiffness, can improve identification and collection of starting cell populations,

[1]Portions of this chapter were reproduced from [19].

with applications to mesenchymal stem cell therapies and stem cell-based tissue engineering.

3.2 Introduction

Human mesenchymal stem cells (hMSCs) hold great potential for autologous therapy, highlighted by the properties of immunosuppression, migration to injured tissues, and tissue repair via soluble factor secretion [75]. MSC osteoblast differentiation following bone graft incorporation may facilitate subsequent bone formation [4]. However, the absence of donor- and anatomical location-independent MSC biomarkers hampers the collection of MSCs from bone marrow or adipose tissue for clinical therapies [4], which establishes a need to improve phenotype detection by identifying additional MSC biomarkers.

The lack of reliable cell-surface or intracellular markers of terminal MSC osteoblast differentiation precludes techniques such as fluorescence-activated cell sorting from successful phenotype identification. Common markers of MSC osteoblast differentiation, including alkaline phosphatase, osteopontin, and osteonectin, peak prior to mineralization of the extracellular matrix [6, 152], and are therefore not optimal for definitive phenotype identification. Two other MSC osteoblast differentiation markers, bone sialoprotein (BSP) and osteocalcin (OCN), are considered to be late osteogenesis markers, but are produced by other cells that form the mineralized matrix [6, 152]. Isolation of extracellular matrix constituents, such as BSP, OCN, and other common osteoblastic proteins, requires dissociative, cell-destructive methods. Therefore, locally synthesized proteins are difficult to distinguish from matrix-trapped proteins derived from other sources, such as serum. Altogether, these facts emphasize a need for additional cell-specific osteoblastic markers to identify cell phenotype.

Compared to extracellular protein markers, cellular stiffness is easily attributable to individual cells, and thus may serve as a candidate osteoblastic marker. Cellular

stiffness has been proposed as an indicator of multiple cellular processes, including cancer metastasis [31, 35, 136, 162] and apoptosis [70, 84], as well as stem cell differentiation [24, 101, 106, 112, 139] and differentiation potential [59, 65].

Previous cell mechanics experiments suggest that hMSC stiffness can change during osteoblast differentiation [34, 40, 142, 165, 166], but the network of factors that influences the observed stiffness changes is poorly understood. Moreover, the factors that affect cellular stiffness are confounded by the mechanical heterogeneity of cell populations and, in the case of stem cell studies, asynchronous differentiation kinetics (Fig. 3.1A). Thus, inherent heterogeneity and asynchronous differentiation of stem cell populations motivate the need for single-cell forms of analysis [38].

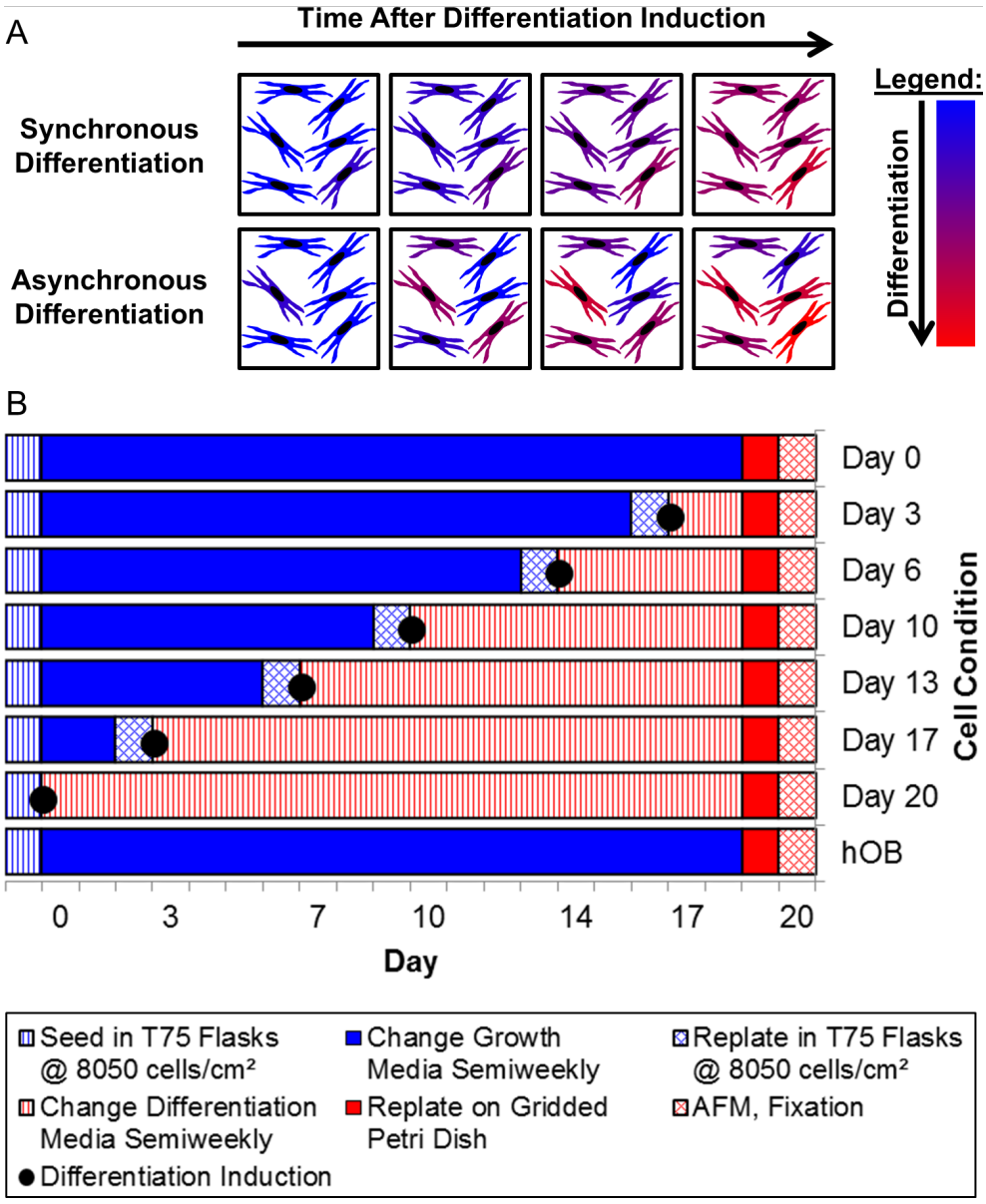

Figure 3.1: hMSC Differentiation. A. Synchronous and asynchronous differentiation modes can result in the same population-average differentiation state. However, the asynchronous differentiation of MSCs necessitates single-cell assays for the most rigorous analysis of differentiation biomarkers. **B.** The staggered differentiation scheme was employed such that earlier time points were induced to differentiate prior to later time points. Thus, all cells completed osteoblast differentiation simultaneously, regardless of the differentiation time point, limiting the confounding effects of substrate-induced stiffening. The scheme permitted the Young's modulus to be measured for all cells during a single AFM session.

In contrast to the population-wide correlations employed by other studies, a recent study elegantly correlated the mechanical properties and differentiation potential of

individual stem cell clones [59]. However, investigations of single-cell relationships between mechanical properties and traditional biomarkers are needed to determine how effectively individual parameters indicate the differentiation state. Consequently, the objective of this study was to evaluate cell stiffness as a single-cell marker of hMSC osteoblast differentiation in comparison to conventional phenotypic markers (BSP and OCN).

The stiffness, morphology, and differentiation state of hMSCs undergoing osteoblast differentiation were assessed via atomic force microscopy (AFM) and imaging of a fluorescent membrane lipid dye and immunofluorescent BSP and OCN stains, respectively. Custom gridded Petri dishes were used to match individual cells measured by AFM to those assayed by subsequent fluorescence imaging. To investigate the utility of cell mechanics in reflecting differentiation state, single-cell correlations between the day of differentiation and either mechanical or molecular markers were compared.

3.3 Methods

3.3.1 Cell Culture

Passage 1 bone marrow-derived hMSCs were obtained from Texas A&M (Donor 8002L). Immunophenotyping after expansion to passage 4 confirmed hMSC phenotype (Fig. 3.2). hMSC growth medium (16% fetal bovine serum [FBS, Atlanta Biologicals, Flowery Branch, GA], 2 mM L-glutamine, and 1% penicillin/streptomycin [P/S] in alpha minimum essential medium) was changed semiweekly. Normal human osteoblasts (hOBs) were obtained from Lonza, and hOB growth medium (10% FBS, 1% P/S in Dulbecco's modified Eagle's medium) was changed every 48 hours. Upon reaching 85% confluency, cells were washed with phosphate buffered saline (PBS), detached using 0.25% trypsin/EDTA, and subpassaged at 60 cells/cm^2 (hMSCs) or 1:2 (hOBs) until passage 4.

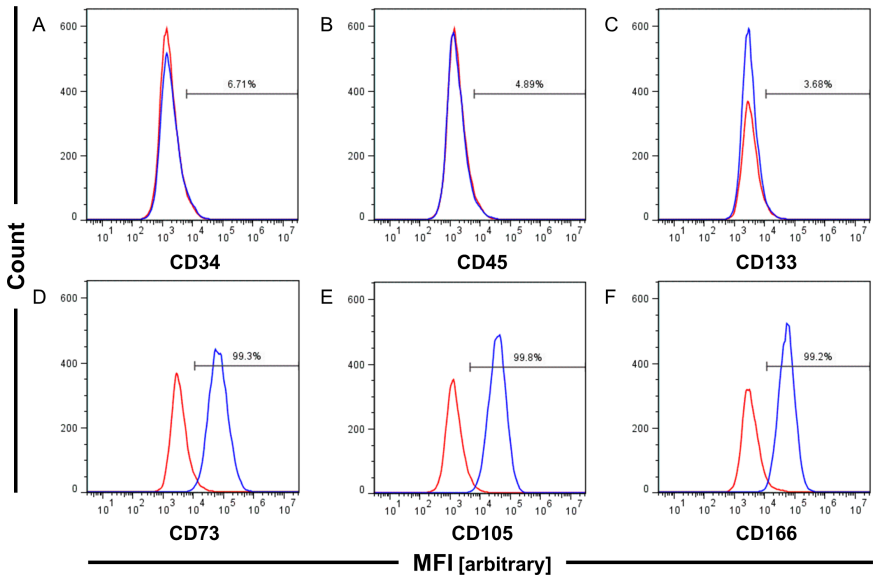

Figure 3.2: hMSC Immunophenotyping. Fluorescence intensity histograms were gated to indicate the percentage of putative hMSCs positive for the indicated antibody (blue) compared to the relevant negative control (red; α=0.05). Putative hMSCs were CD34-, CD45-, CD133-, CD73+, CD105+, and CD166+ (A-F), indicating MSC phenotype.

3.3.2 Osteoblast Differentiation

hMSC osteoblast differentiation was induced by semiweekly media changes of hMSC growth medium supplemented with 10 nM dexamethasone, 20 mM -glycerol phosphate, and 50 μM L-ascorbic acid 2-phosphate [114]. To improve the consistency of the AFM results, a staggered osteoblast differentiation scheme was employed, in which earlier time points were induced to differentiate prior to later time points. Thus, hMSCs undergoing 0, 3, 6, 10, 13, 17, and 20 days of osteoblast differentiation (hMSC-OBs) reached the specified differentiation time points simultaneously (Fig. 3.1B).

3.3.3 Gridded Petri Dishes

Gridded Petri dish manufacture is illustrated in Fig. 3.3A. Petri dishes were engraved with a grid pattern chosen to facilitate matching of AFM cell mechanics data to immunofluorescence images (Figs. 3.3B–3.3D). The grid was engraved using a VLS3.50

laser cutter (Universal Laser Systems, Scottsdale, AZ) with parameters optimized for grid visibility, while minimizing the line width to approximately 75 μm.

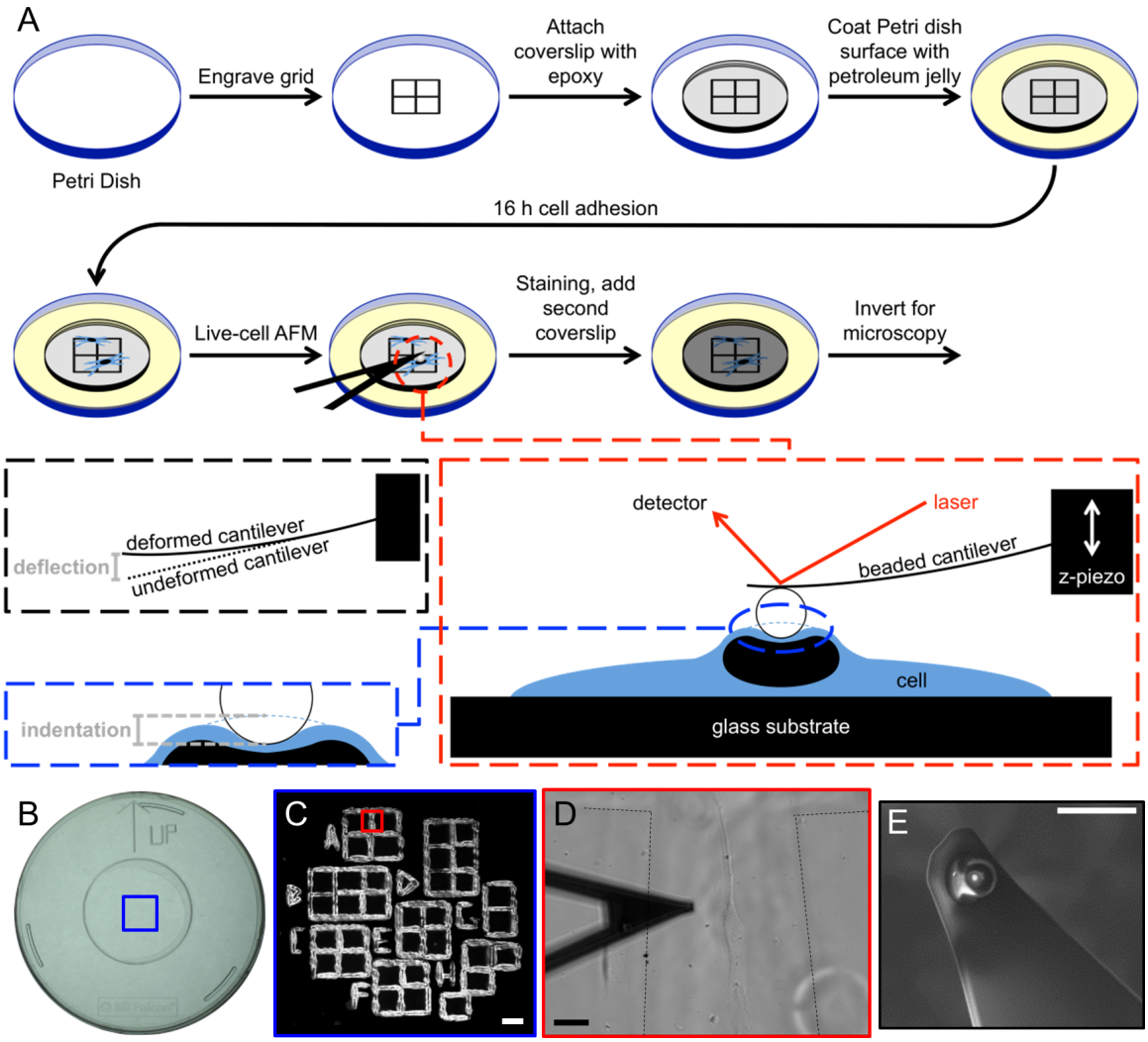

Figure 3.3: Gridded Petri Dish Manufacture. A. The gridded Petri dish design allowed sequential measurement of live-cell stiffness and fluorescent protein biomarker expression at the single cell level, enabling a cell-by-cell analysis of the relationships among differentiation, mechanical, protein staining, and morphological factors. Force-indentation data were used to evaluate the Young's modulus of each cell. **B.** Following engraving, the gridded Petri dish was covered with a glass coverslip, which prevented the grid from influencing morphology during cell attachment. **C.** Magnified region of interest of Panel B, indicated in blue. The design of the grid was chosen to facilitate pinpointing of individual cells during AFM and fluorescence microscopy. Scale bar, 750 μm. **D.** Magnified region of interest of Panel C, indicated in red. The locations of individual cells within the grid were recorded during AFM. Dashed black lines indicate grid; scale bar, 25 μm. **E.** AFM stiffness measurements were taken using a beaded cantilever to increase cell-probe surface area, thereby allowing measurement of bulk cellular Young's modulus. Scanning electron micrograph; scale bar, 10 μm.

To prevent cell attachment to the sites of engraving, each grid was covered with a glass coverslip. Engraved dishes and glass coverslips were soaked in 70% ethanol, sterilized by UV light exposure, and attached using two-part epoxy. After curing for 24 h, sterile technique was used to apply petroleum jelly to the Petri dish surface, but not the coverslip surface, thereby decreasing the effective dish surface area and limiting the required volumes of cells and immunofluorescence reagents. The fully assembled dishes were sterilized by UV light exposure before cell plating. Gridded Petri dishes yielded similar hMSC morphology compared to glass and tissue culture polystyrene surfaces.

3.3.4 Atomic Force Microscopy

Prior to AFM measurements, a 5.5 μm polystyrene bead (Bangs Labs, Fishers, IN) was attached to a tipless silicon nitride cantilever (MLCT-O10, Bruker, Camarillo, CA, Cantilever D, k=10-60 pN/nm) using two-part epoxy with 24 h curing time (Fig. 3.3E). Compared to pyramidal probe geometry, the spherical probe increased the probe-cell contact area and improved the accuracy of global cell stiffness measurements [112, 142].

Approximately 2,500 hMSC-OBs or hOBs were plated onto gridded Petri dishes in their respective growth medium. Cells were adhered for 20-32 h and washed with PBS before mechanical characterization using an atomic force microscope (Asylum Research, Santa Barbara, CA) on a vibration isolation table (Herzan, Laguna Hills, CA). Phase contrast microscopy (Eclipse Ti, Nikon, Melville, NY) was used to locate the cells and to position the beaded probe over the center of each cell. Thermal calibration [74] yielded the cantilever spring constant, k=19.80 pN/nm. A measurement rate of 0.39 Hz and a probe velocity of 2.34 μm/s were used. The 2 nN force trigger resulted in indentations of 250-500 nm for typical cells, corresponding to approximate contact areas of 4.3-8.6 μm^2. To determine cellular Young's modulus, IGOR

software (Wavemetrics, Portland, OR) was used to apply the Hertzian contact model to the portion of the extension force-displacement curves from 50-95% of the maximum indentation, over which range the Young's modulus was generally independent of indentation. The mean Young's modulus of three measurements was calculated for each cell, using indentation offset as a free variable and assuming cellular Poisson's ratio, ν=0.5.

3.3.5 Immunofluorescence Imaging and Image Processing

3.3.5.1 Single-Cell

Cells were fixed, permeabilized, and simultaneously stained for cell membrane (HCS CellMask Blue, Invitrogen, Carlsbad, CA), BSP (anti-BSP and fluorescein isothiocyanate-conjugated secondary antibody), and OCN (phycoerythrin-conjugated anti-OCN), as detailed in the Supplementary Information.

Following immunofluorescence staining, cell identity was determined by location within the grid using a Nikon Eclipse Ti microscope under halogen light illumination and confirmed by comparison to images taken during AFM. Cell membranes and antibody-labeled BSP and OCN were visualized using the 4',6-diamidino-2-phenylindole, fluorescein isothiocyanate, and tetramethylrhodamine isothiocyanate excitation/emission filter sets, respectively. Individual cells were imaged using a CoolSNAP HQ2 camera (Photometrics, Tuscon, AZ).

The relatively high signal-to-noise ratio of the cell membrane images allowed use of the ImageJ rolling ball algorithm to subtract the background from each image. However, due to substantial background autofluorescence, the BSP and OCN images were enhanced using a different method of background subtraction. ImageJ (National Institutes of Health, Bethesda, MD) was used to generate background images for each day of differentiation by averaging the intensity of raw BSP or OCN images and applying a 25 μm Gaussian blur.

Spread cells have previously been shown to be stiffer than spherical cells [34],

indicating that morphology may play an important role in apparent cell stiffness; therefore, the morphology of each cell measured by AFM was quantified. CellProfiler™ [21] was used to identify the boundary of each cell by applying a background global threshold to each corrected cell membrane image. ImageJ was used to characterize cell morphology by calculating the minor and major axes, Feret's diameter, perimeter, area, aspect ratio, circularity, eccentricity, perimeter:area ratio, and roundness of each cell boundary. Quantification of cell membrane images was validated by the expected positive correlations among size descriptors as well as correlations between factors, such as aspect ratio and eccentricity, which are directly mathematically linked (see Supplementary Information). For each BSP and OCN corrected image, protein staining was quantified as the fraction of pixels within the cell boundary that exceeded a threshold value (percent area) [30, 55]. Quantification of single-cell morphology and protein staining is illustrated in Fig. 3.4.

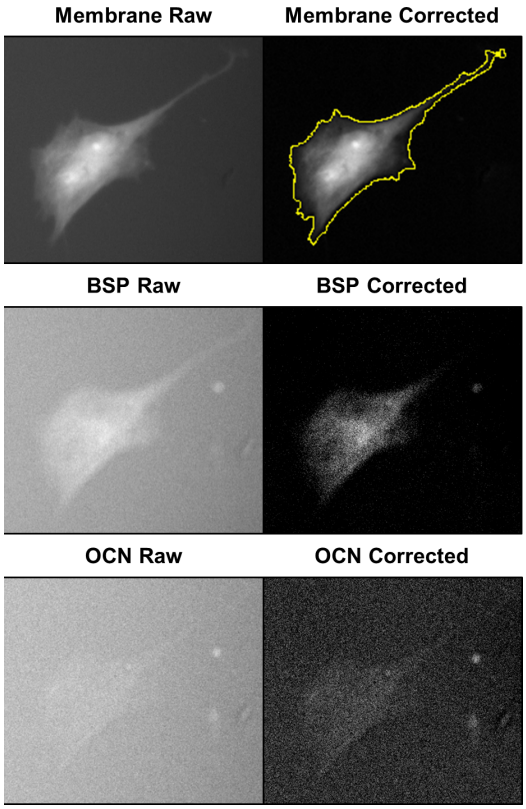

Figure 3.4: Scheme for Quantification of Cell Morphology and Differentiation Biomarkers. 1. Each of three fluorescent channels was imaged to obtain raw images of the cell membrane, bone sialoprotein (BSP), and osteocalcin (OCN) stains. **2.** The rolling ball background correction algorithm was applied to the raw membrane image. **3.** For each day of differentiation, ImageJ was used to average the raw BSP and OCN images and apply a Gaussian blur to generate a background image. The background images were subtracted from the raw images, resulting in the corrected BSP and OCN images. **4.** CellProfiler was used to detect the boundary of the cell using the corrected cell membrane image (yellow). **5.** Morphological factors were determined from the cell boundaries using ImageJ. For each BSP and OCN corrected image, protein staining was quantified as the fraction of pixels within the cell boundary that exceeded a threshold value.

3.3.5.2 Population

hMSC-OBs and hOBs were plated at 8,050 cells/cm^2 on glass coverslips, stained as described above, and mounted on glass slides prior to imaging. Cell membranes, BSP, and OCN were imaged and background corrected a priori. The boundaries of naive hMSCs were identified using a classifier generated by ilastik software [131] and 3-class Otsu global thresholding in CellProfiler™, and the identified region was used for quantification. Since all other hMSC-OBs and hOBs were confluent, the entire image was used for quantification. BSP and OCN staining was quantified as described above. Threshold values for each fluorescent channel were identical for single-cell and cell population images.

3.3.6 Statistics

Due to the unequal sample size, heteroscedasticity, and non-normal distribution of the AFM data, parametric bootstrapping was performed (10,000 iterations) using a MATLAB (MathWorks, Natick, MA) routine. Differences in mean Young's moduli for the 7 hMSC-OB time points and the hOB sample were compared by bootstrapping one-way ANOVA, yielding p=0.0002. Post-hoc analysis was performed using pairwise, heteroscedastic bootstrapping Student's t-tests.

225 total cells from the 7 hMSC-OB time points and the hOB sample were tested

for pairwise correlations among phenotypic properties. Using JMP software (SAS Institute, Cary, NC), pairwise, nonparametric Spearman's correlation coefficients were calculated to test for monotonic trends among the 14 single-cell differentiation, mechanical, protein staining, and morphological variables and among the day of differentiation and population protein staining variables. For the purposes of correlation calculations, the hOB time point was considered to be after Day 20 of hMSC differentiation. Two-tailed p-values (H_0: ρ=0) were calculated for each correlation coefficient using Student's t-test.

All obtained p-values were adjusted using Holm's procedure for multiple comparisons. Since Holm's adjusted p-values tend to be conservative, α=0.10 was chosen. Original and adjusted p-values are listed in the Supplementary Information.

3.4 Results

3.4.1 Cell Mechanics

Before investigating the relationships between cellular stiffness and molecular differentiation biomarkers, stiffness trends during differentiation were examined. The stiffness values of passage 4 hMSCs from two donors were not significantly different (Fig. 3.5, p=0.368), so donor 8002L was used for the remainder of the study. Analysis of force-indentation curves generally yielded higher Young's moduli for hMSCs than hOBs (Fig. 3.6A). Although the stiffness data were highly variable (coefficient of variation>0.5), stiffness generally decreased during osteoblast differentiation (Fig. 3.6B). Importantly, Day 20 hMSC-OBs were significantly softer than naive hMSCs ($p_{adjusted}$=0.083), but not hOBs (Fig. 3.6C, $p_{adjusted}$=1.000).

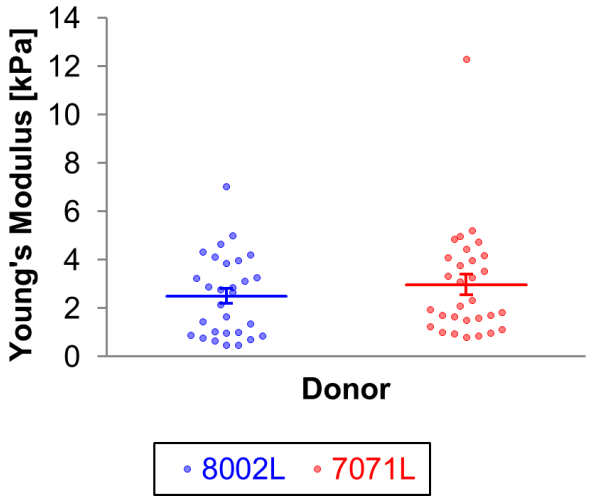

Figure 3.5: Donor-Independent Stiffness. hMSC stiffness was not significantly different for two cell donors (Student's independent t-test; p=0.368, α=0.05, lines indicate mean $\pm$ standard error).

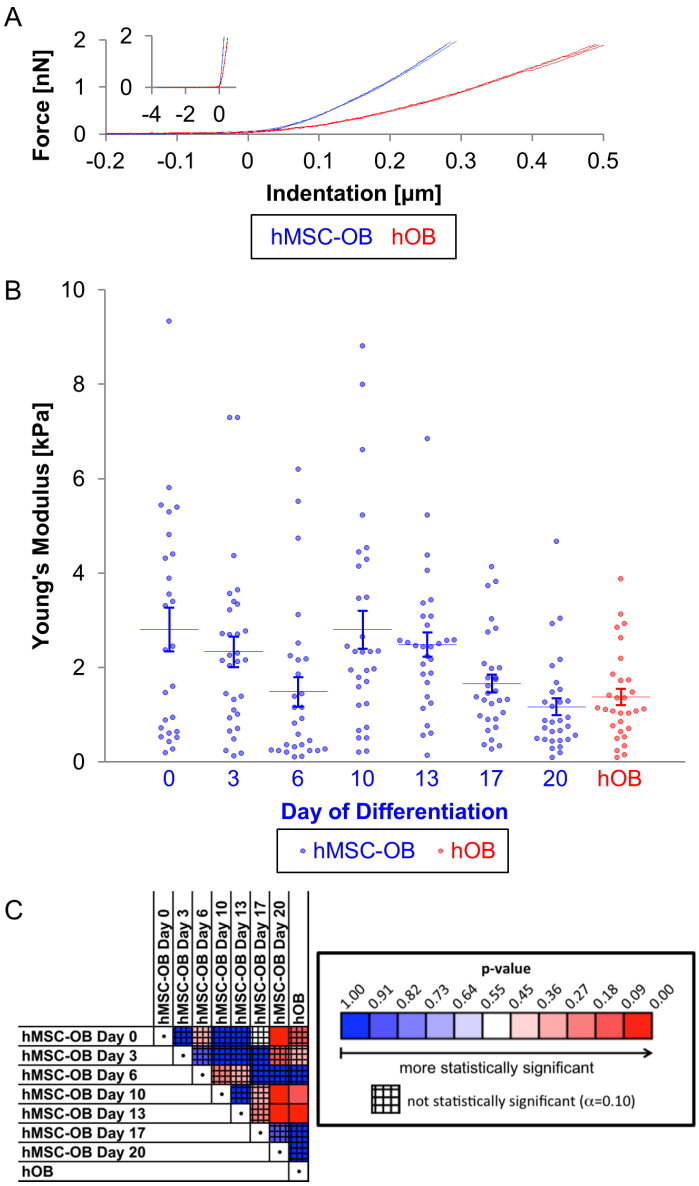

Figure 3.6: Atomic Force Microscopy. A. Three force-indentation curves per cell were fit to the Hertzian contact model to calculate the mean Young's modulus. Representative force-indentation curves yielded mean Young's moduli of approximately 4.3 kPa for the naive hMSC (blue), and 1.9 kPa for the hOB (red). **B.** Young's modulus generally decreased as osteoblast differentiation progressed, although a large degree of variation was observed (coefficient of variation>0.5). Lines indicate mean standard error. Day 0, n=26; Day 6, n=28; others, n=30. **C.** Statistical significance of mean Young's modulus differences among the 8 cell conditions is displayed. Importantly, Day 20 hMSC-OBs were significantly softer than naive hMSCs, but not hOBs. Holm's adjusted p-values range from 0 (bright red) to 1 (bright blue). Crosshatch pattern indicates that the difference between mean Young's moduli is not statistically significant (α=0.10).

3.4.2 Pairwise Correlations Among Single-Cell Parameters

Spearman's correlations were calculated among the differentiation, mechanical, protein staining, and morphological parameters for each cell (Fig. 3.7A). A significant inverse relationship between Young's modulus and the day of differentiation was supported by the Spearman's correlation coefficient (ρ=-0.214, $p_{adjusted}$=0.055) and the partial Spearman's correlation coefficient (r=-0.145,p=0.033, Supplementary Excel Sheet 1), substantiating the observed decrease in stiffness during differentiation. Young's modulus correlated positively and significantly with major axis, Feret's diameter, perimeter, and area, but negatively and significantly with circularity, indicating that the stiffest cells were generally large and elongated (Fig. 3.7A).

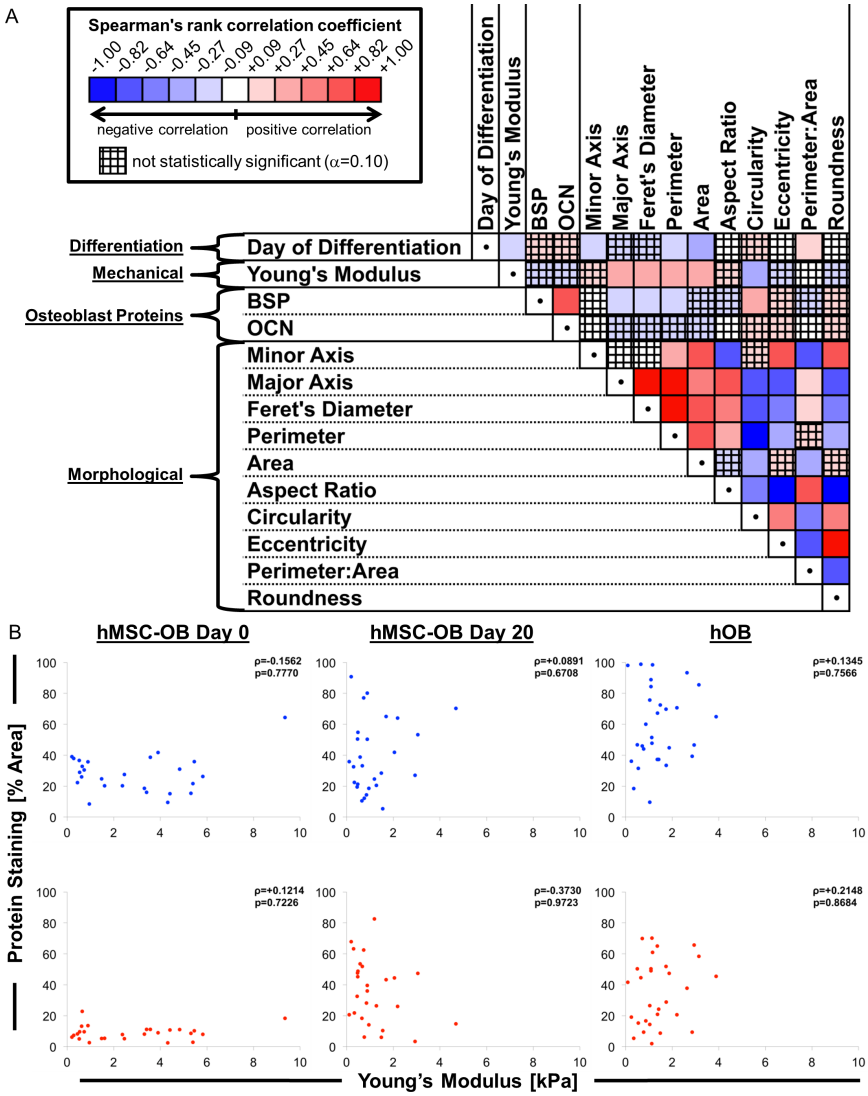

Figure 3.7: Single-Cell Correlation Color Matrix. A. For 225 individual cells, values of the 14 differentiation, mechanical, protein staining, and morphological parameters were determined from AFM data and fluorescence image processing. Staining for BSP and OCN was quantified as the fraction of pixels within the cell boundary that exceeded a threshold value (percent area). Pairwise Spearman's correlation coefficients among the 14 variables are displayed. Spearman's rank correlation coefficients range from -1 (bright blue) to +1 (bright red). Crosshatch pattern indicates a correlation that was not statistically significant based on Holm's adjusted p-values (α=0.10). Day 0, n=26; Day 3, n=29; Day 6, n=24; Day 20, n=27; hOBs, n=29; others, n=30. A significant inverse relationship between Young's modulus and the day of differentiation was observed. The strong, positive correlation between bone sialoprotein (BSP) and osteocalcin (OCN) staining appears to suggest that BSP and OCN staining both reflect osteoblast differentiation as expected. However, correlations between the day of differentiation and protein staining were weak and not statistically significant. **B.** For each cell condition, the correlation between BSP (top, blue) or OCN staining (bottom, red) and Young's modulus was weak ($|\rho| < 0.45$) and not statistically significant (for other time points, see Fig. 3.8).

The strong, positive correlation between single-cell BSP and OCN suggested coordinated protein expression changes, which is expected since BSP and OCN are both osteoblast differentiation markers. However, correlations between the day of differentiation and protein staining for individual cells were weak and not statistically significant (BSP, ρ=0.198, $p_{adjusted}$=0.107; OCN, ρ=0.181, $p_{adjusted}$=0.230). For individual days of differentiation, the correlations between protein staining and Young's modulus were also weak ($|\rho| < 0.45$) and not statistically significant (Figs. 3.7B, 3.8; BSP, $p_{adjusted}$=1.000; OCN, $p_{adjusted}$=0.960).

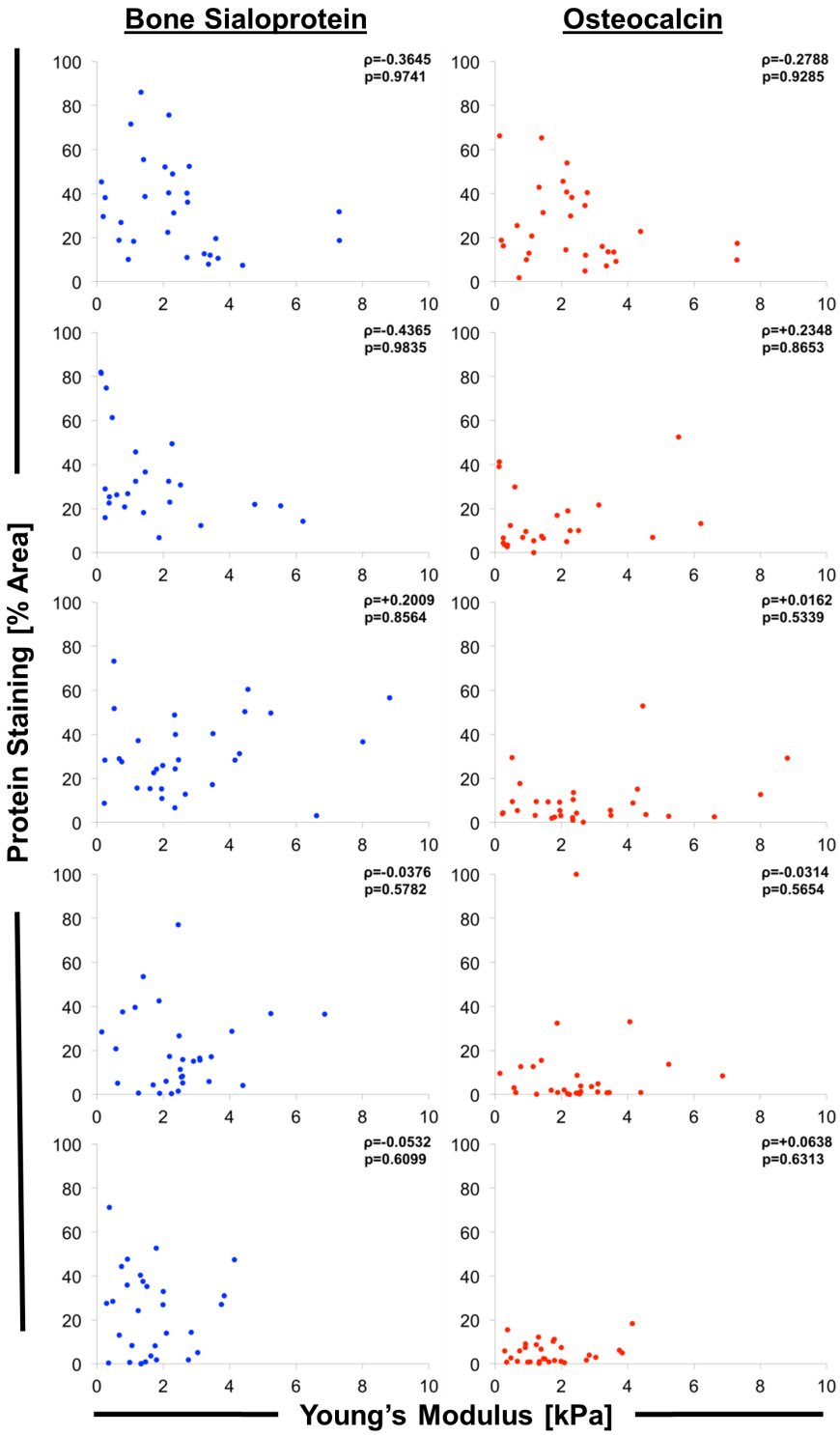

Figure 3.8: Single-Cell Correlation Scatter Plots. For each cell condition, the correlation between Young's modulus and bone sialoprotein (blue) or osteocalcin staining (red) was weak ($|\rho| < 0.45$) and not statistically significant. From top to bottom, the rows indicate hMSC-OBs after 3, 6, 10, 13, and 17 days of differentiation.

The increase in BSP and OCN staining intensity during differentiation was more pronounced for population than single-cell staining (Fig. 3.9). The weak correlations ($|\rho| < 0.2$) between single-cell protein staining and the day of differentiation corroborated the weak, not statistically significant correlations between single-cell protein staining and Young's modulus.

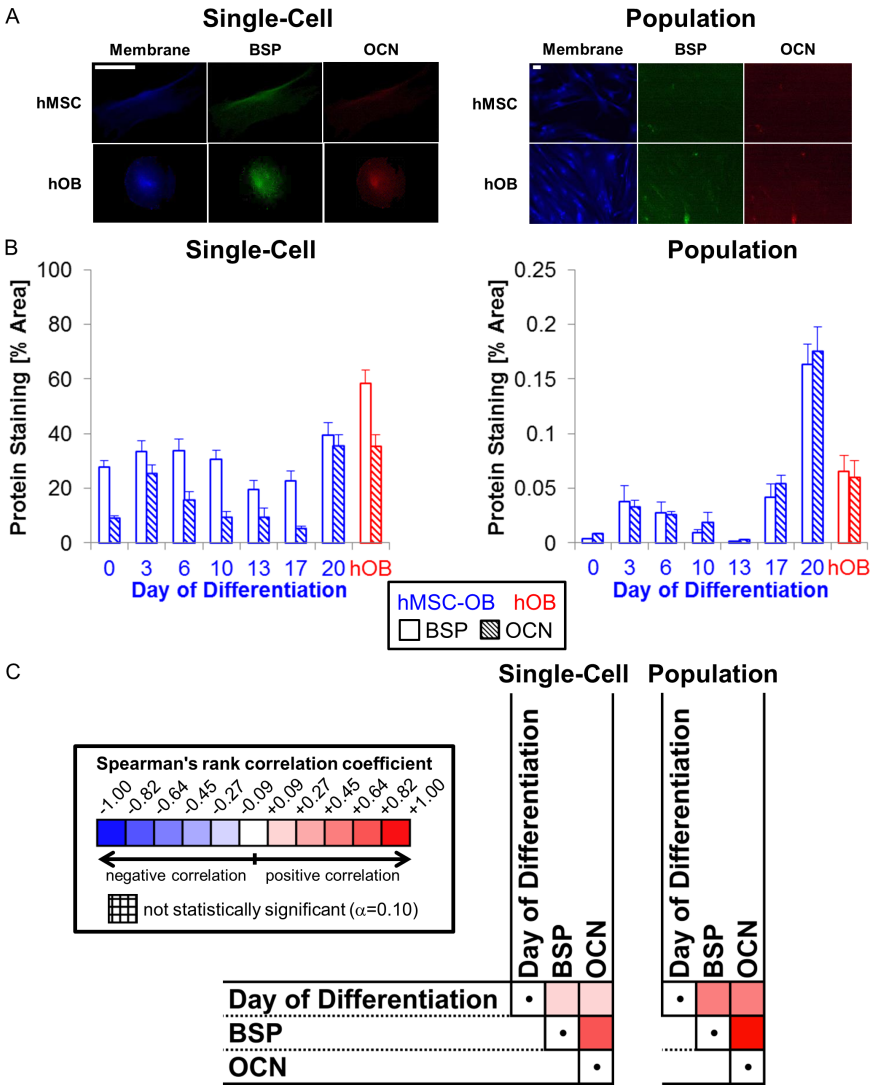

Figure 3.9: Biomarker Changes During hMSC Differentiation. A. The difference in bone sialoprotein (BSP) and osteocalcin (OCN) staining between the representative naive hMSC and hOB images was visually more apparent for population than single-cell images, indicating that BSP and OCN staining may more rigorously indicate osteoblast differentiation for cell populations than single cells. Scale bars, 50 μm. **B.** BSP and OCN staining did not appear to trend strongly with the day of differentiation for single-cell staining, but population staining revealed more abundant protein staining for the later days of differentiation (mean + standard error). **C.** Correlations between the day of differentiation and protein staining were weaker for single-cell than population staining. Spearman's rank correlation coefficients range from -1 (bright blue) to +1 (bright red). Checkerboard pattern indicates a correlation that was not statistically significant based on Holm's adjusted p-values (α=0.10). Single-cell data are repeated from Fig. 3.7A, but Holm's adjustment was reapplied using N=3 for purposes of comparison.

3.5 Discussion

During chemically-induced hMSC osteoblast differentiation, decreases in cellular stiffness, size, and circularity were observed. Whereas Young's modulus indicated differentiation of single cells, staining for BSP and OCN indicated differentiation more robustly at the population than the single-cell level.

The cellular softening observed during hMSC osteoblast differentiation may have resulted from concurrent changes in the underlying cellular structure. Recent studies predicted stem cell differentiation fate based on the combination of several actin filament morphology descriptors [144]. F-actin staining parameters, including mean intensity, total intensity, and the number of F-actin branches, changed during hMSC osteoblast differentiation [144]. Furthermore, the cellular softening observed during osteoblast differentiation has been attributed to a simultaneous transition from many thicker actin fibers to a fewer number of thinner actin fibers in hMSCs [142, 165] and amniotic fluid-derived stem cells [24]. In hMSCs, actin stress fibers were long, thin, parallel, and oriented along the major axis of the cell; cytoskeletal rearrangement during osteoblast differentiation resulted in hMSC-OBs with thicker, disordered actin filaments [117, 142, 165]. Interestingly, the actin organization of the spindle-shaped rapidly self-renewing hMSC subset matched the expected hMSC phenotype, but the flat cell hMSC subset matched the osteoblast phenotype [40]. The presence of hMSC morphology subsets indicates the large degree of hMSC heterogeneity, which may partially explain the large degree of stiffness variation observed in naive hMSCs (Fig. 3.6B).

To further investigate the notion of cytoskeletal rearrangement during osteoblast differentiation, raw gene expression data for Day 0, 1, 7, and 10-14 hMSC-OBs and hOBs [62] were downloaded from the gene expression omnibus dataset GSE 12267

(http://www.ncbi.nlm.nih.gov/geo/) and analyzed by gene set enrichment analysis (GSEA) and differential expression analysis (DEA), as described in the Supplementary Information. GSEA indicated that the chromosome, chromatin, and cytoskeleton cellular component ontologies were relevant to the phenotypic differences between hMSCs and hOBs. Furthermore, genes identified by DEA as differentially expressed between hMSCs and hOBs were found to be significantly enriched in cytoskeleton remodeling-related maps (Figs. 3.10, 3.11). Several genes related to actin binding and regulation of the actin cytoskeleton were decreased (ACTN1 [α-actinin-1], ACTG2, ACTR2, ANLN, FBLIM1) or increased (TWF1 [twinfilin], ADD3, and GSN [gelsolin]) in hOBs relative to hMSCs (Supplementary Excel Sheet 2). Time course analysis also identified 222 genes with consistent expression increase during osteoblast differentiation (Supplementary Excel Sheet 3).

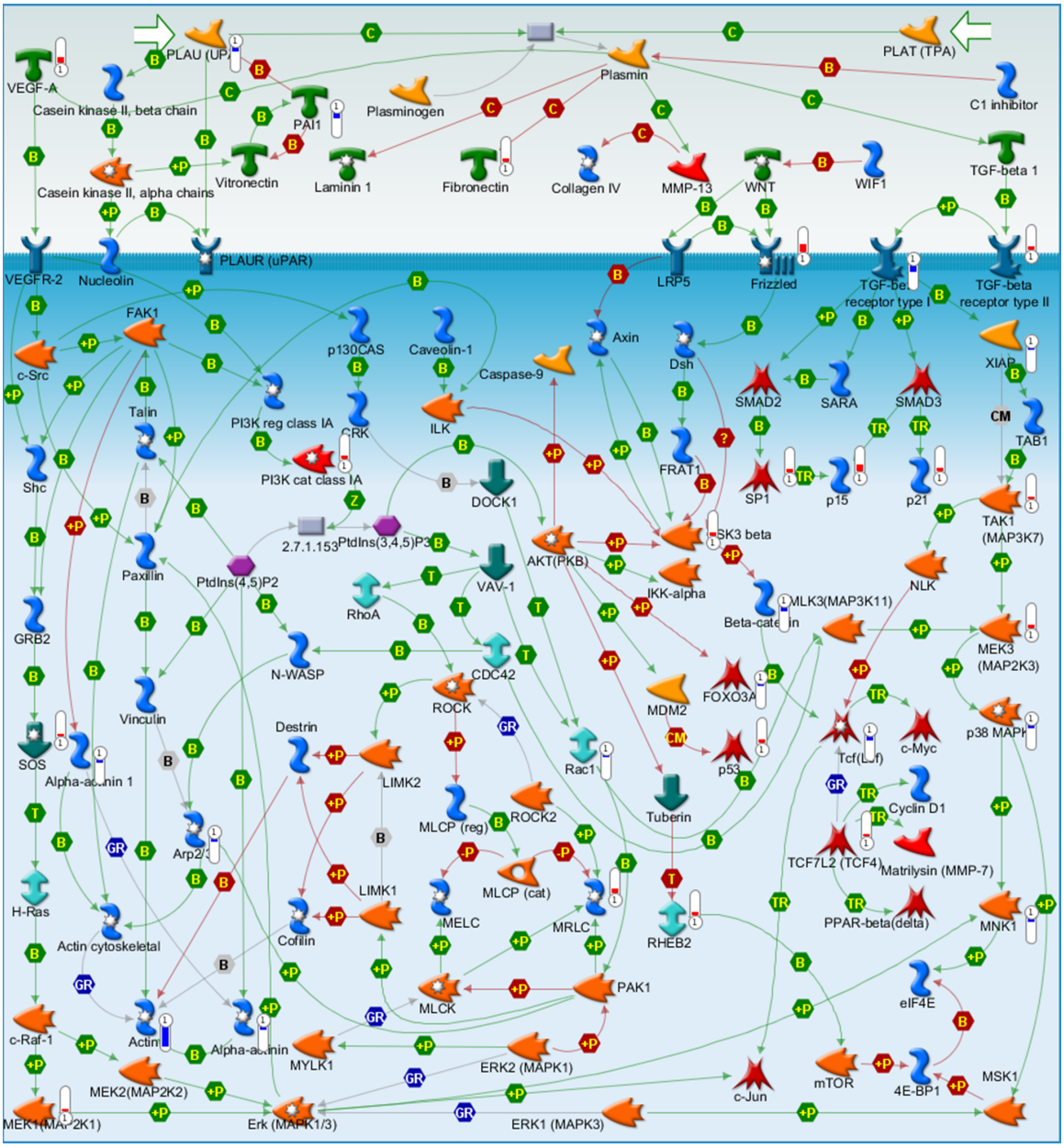

Figure 3.10: Cytoskeleton Remodeling TGF WNT Map. Genes differentially expressed between hMSCs and hOBs are depicted as red thermometers (increased expression in hOBs) or blue thermometers (increased expression in hMSCs).

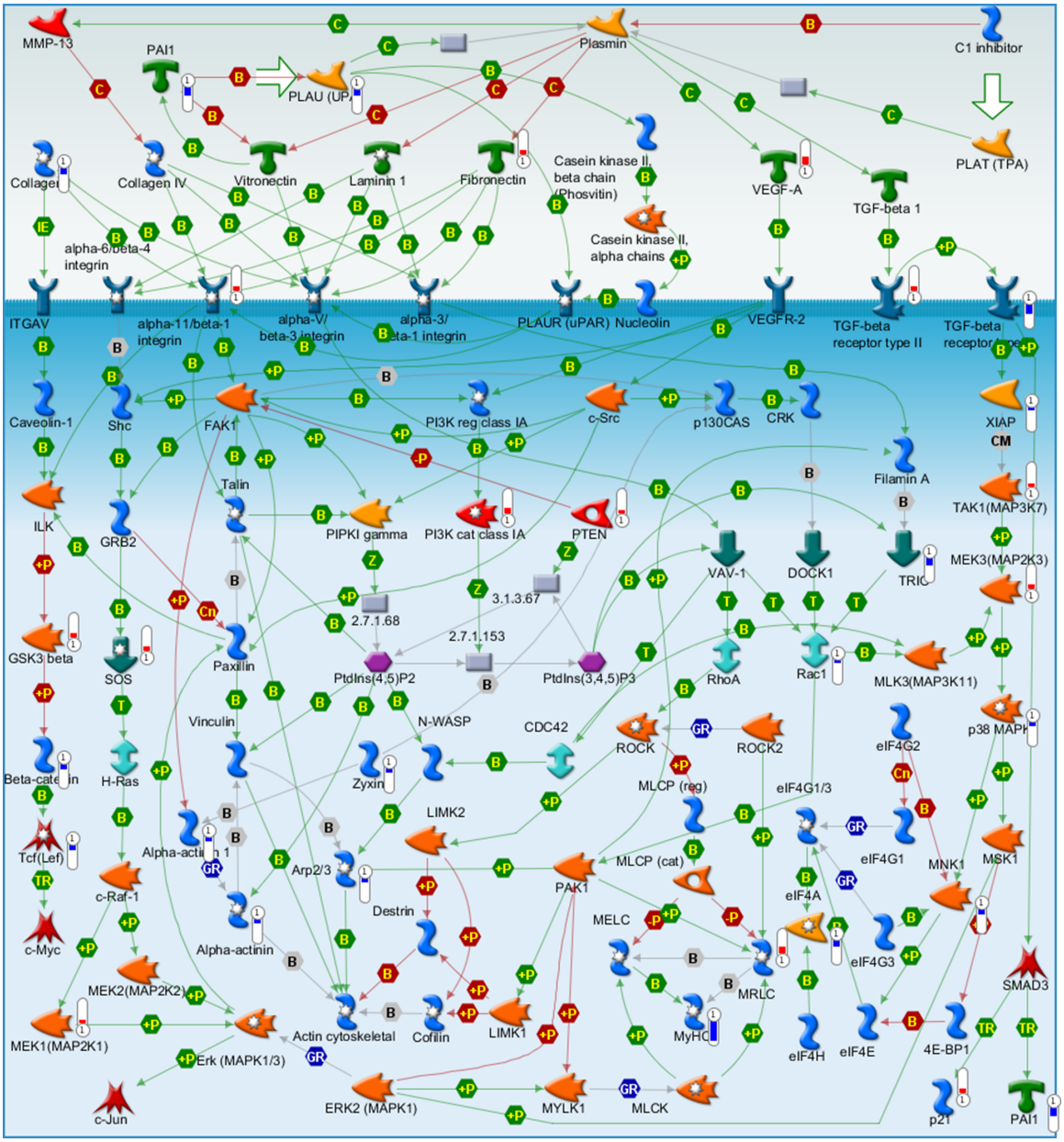

Figure 3.11: Cytoskeleton Remodeling Map. Genes differentially expressed between hMSCs and hOBs are depicted as red thermometers (increased expression in hOBs) or blue thermometers (increased expression in hMSCs).

Gene expression analysis suggested that cytoskeletal remodeling during osteoblast differentiation may result from the combined effects of reduced G-actin polymerization, reduced F-actin cross-linking, and enhanced severing of actin filaments. Reduced G-actin polymerization in hOBs was indicated by decreased expression of actin

monomers (e.g. ACTG2), twinfilin-mediated sequestration of G-actin [102], and decreased activity of the Arp2/3 complex. Reduced F-actin cross-linking in hOBs was indicated by decreased expression of α-actinin-1, which is critical in leading edge focal adhesion maturation during cell spreading [82]. Decreased expression of α-actinin-1 in hOBs may therefore partially explain the positive correlation between cell size and stiffness (Fig. 3.7A). Increased expression of twinfilin and gelsolin suggested enhanced severing of actin filaments in hOBs. Gene expression analysis therefore supported actin cytoskeletal rearrangement during osteoblast differentiation.

Previous work has directly linked actin reorganization to cell stiffness changes. Cells characterized by ordered actin filament geometry tended to be stiffer than cells with disordered actin fibers [79, 162]. Furthermore, α-actinin-1, which was increased in hMSCs relative to hOBs, crosslinks actin filaments and increases the stiffness of the actin filament network [49, 160]. Therefore, based solely on actin fiber organization, hMSCs would be expected to soften during osteoblast differentiation, as shown previously [24, 142] and in the present study. Furthermore, the connections between cellular stiffness and reported changes in cytoskeletal gene expression lend credence to the observed softening during osteoblast differentiation.

The mechanics data of spread morphology hMSCs during osteoblast differentiation is characterized by a large degree of variation [34, 40, 142, 165]. Thus, measures were taken to control substrate-induced stiffening and cell density, which could otherwise confound stiffness data since naive MSC stiffness increases with the duration of growth in vitro [92]. Passage 4 cells were used throughout the study to keep the total amount of time in vitro constant and reduce confounding substrate-induced stiffness changes. Furthermore, a staggered differentiation scheme was employed, allowing all cells to grow on tissue culture polystyrene for an equal amount of time before AFM analysis. Cells were also trypsinized and replated approximately 1 day before AFM measurements. Adhesion of the replated cells may have resulted in some differences in

differentiation from traditional induction assays; however, replating at low cell density limited morphology changes due to uncontrolled cell-cell contact, which can influence cell mechanics measurements [44]. Factors that could otherwise confound stiffness comparisons between differentiation time points were controlled, which strengthens the claim that cell stiffness decreases during osteoblast differentiation.

BSP and OCN are commonly used to indicate osteoblast differentiation, but correlations between the day of differentiation and single-cell protein staining were not significant (Fig. 3.7A). The trend between protein staining and the day of differentiation was stronger for population staining than single-cell staining (Fig. 3.9C), which may reflect the extracellular localization of BSP and OCN as well as the concept of asynchronous osteoblast differentiation. Unlike single-cell staining, population averaged protein staining cannot detect subsets of cells that express BSP or OCN at any one time, as previously observed in the formation of nodules prior to hMSC osteoblast differentiation [6]. Young's modulus may therefore provide additional and improved information on the osteoblastic state of single cells.

As a label-free property of individual cells, Young's modulus holds great potential in phenotype identification. Furthermore, Young's modulus is attributable to individual suspended cells, and thus potentially lends itself to phenotypic cell sorting applications. Recent developments in cell separation by adhesion [128] and stiffness [73, 156] indicate future label-free cell sorting capabilities for cases in which molecular biomarkers are not fully established. Continued investigation of various differentiation lineages, beyond the osteoblast differentiation considered in this study, is required to further understand and use mechanical differentiation indicators. Additional characterization of stiffness and other cell-intrinsic physical properties promises to result in the development of novel, label-free cell identification and sorting capabilities.

CHAPTER IV

CELLULAR STIFFNESS AS A NOVEL STEMNESS MARKER IN THE CORNEAL LIMBUS[1]

4.1 Abstract

Healthy eyes contain a population of limbal stem cells (LSCs) that continuously renew the corneal epithelium. However, each year, 1 million Americans are afflicted with severely reduced visual acuity caused by corneal damage or disease, including limbal stem cell deficiency (LSCD). Recent advances in corneal transplant technology promise to repair the cornea by implanting healthy LSCs to encourage regeneration; however, success is limited to transplanted tissues that contain a sufficiently high percentage of LSCs. Attempts to screen limbal tissues for suitable implants using molecular stemness markers are confounded by the poorly understood signature of the LSC phenotype. For cells derived from the corneal limbus, we show that the performance of cell stiffness as a stemness indicator is on par with the performance of $\Delta NP63\alpha$, a common molecular marker. In combination with recent methods for sorting cells on a biophysical basis, the biomechanical stemness markers presented here hold the potential to rapidly purify LSCs from a heterogeneous population of corneal cells, thus potentially enabling clinicians and researchers to generate corneal transplants with sufficiently high fractions of LSCs, regardless of the LSC percentage in the donor tissue.

[1]Portions of this chapter were reproduced from [18].

4.2 Introduction

Each year, more than 1 million Americans suffer impaired eyesight resulting from cornea damage, which may arise from either a congenital cause, such as aniridia-related keratopathy, or an acquired cause, such as chemical or blast injury and Stevens-Johnson syndrome [147]. The resulting dysfunction of limbal stem cells (LSCs), a population of stem cells located in the basal epithelium at the corneoscleral limbus that maintains the cornea, has been recognized as a major cause of prolonged visual loss and blindness [42, 124]. Such LSC dysfunction results in limbal stem cell deficiency (LSCD), a disease characterized by the loss of corneal integrity and impaired corneal wound healing that can result in blindness (reviewed in [2]). Current treatments for LSCD typically entail transplantation of tissue from allogeneic or autologous donors [66]. Transplants sourced from allogeneic donors are limited by the high risk of immunorejection and the general necessity of a life-long immunosuppressive drug regimen [42]. Autologous transplantations are beneficial for unilateral conditions, which typically result from traumatic eye injury, but have limited benefit in the treatment of bilateral congenital eye diseases [69]. Interestingly, the clinical success of transplantation depends not only on the total number but also on the percentage of stem cells in the graft [110]. Transplant success was found to substantially improve when LSCs, defined as $\Delta NP63\alpha$-positive, holoclone-forming cells, comprised 3% or greater of the transplanted cells [115], further illustrating the importance of sufficiently high LSC percentages. However, the ex vivo expansion and transplantation of autologous limbal tissue acquired from contralateral biopsy is fettered by the laborious collection of sufficiently high numbers and percentages of transplanted LSCs [109, 115, 138], which must be performed rapidly to ensure cell viability. Furthermore, the high patient-to-patient variability in the starting percentage of LSCs taken from the tissue biopsy diminishes the utility of ex vivo culturing to treat LSCD with stem cells [115]. Cell enrichment techniques are therefore vital

to the improved treatment of LSCD. Current enrichment methods, which are based on the use of antibodies to select for limbal stem or progenitor cells, include magnetic bead capture and flow cytometry [3, 83, 146]. Such immunologically-based cell enrichment techniques, while useful, are limited by the need for appropriate cell type-specific antibodies. Antibodies against ATP-binding cassettes sub-family G member 2(ABCG2) and sub-family B member 5 (ABCB5) have been successfully used to enrich the LSC population, but also enrich for other ABCG2- or ABCB5-expressing cells present in the limbus and cornea [5, 53, 83, 108]. The use of antibodies to identify LSCs in the clinic is cumbersome, requiring approximately 15 hours of laborious cell processing, and can subsequently affect cellular physiology if the epitope is associated with a functionally important protein domain [36, 68, 105]. A label-free microfluidic device that sorts based on cellular biomechanical properties offers cost and labour advantages over current methods and may provide sufficient enrichment to serve as an alternative or additional approach to antibody-based techniques. Therefore, coupled with label-free cell enrichment approaches, the identification of new biophysical markers of LSCs could greatly improve LSCD treatment by enabling a faster and cheaper process to collect stem-like cells. Recently, cell mechanical properties, including stiffness (i.e. Young's modulus) and size, have been shown to distinguish stem cell phenotypes from differentiated cells at the single-cell level for various stem cell types [19, 34, 112, 118, 165]. Changes to biomechanical properties during stem cell differentiation could enable microfluidic approaches for on-the-fly analysis and sorting of stem cells from differentiated cells. Although LSCs have been characterized by small diameter and high nucleus-to-cytoplasm ratio in comparison to other cells from the limbal region [5, 10, 118], complete biophysical characterization of LSCs in relation to the surrounding corneal cells has not yet been achieved. We present a complete analysis of LSC mechanics, in congruence with the progenitor marker $\Delta NP63\alpha$, which is expressed in LSCs and progenitor cells but not differentiated

cells. The results indicate that cell deformability represents a distinct biophysical marker for stemness identification of cells derived from the corneal limbus. Thus, cell mechanical properties can potentially be used as phenotypic markers for rapid, label-free, microfluidic enrichment of LSCs from corneal tissue as a step towards improving the clinical treatment of LSCD patients.

4.3 Materials and Methods

4.3.1 Cell Isolation and Cell Culture

Human limbal epithelial cells (LECs; Life Technologies, Carlsbad, CA; #C-018-5C) were obtained from the manufacturer. Each lot was characterized by the manufacturer as positive for cytokeratin 15 and $\Delta NP63\alpha$ immunofluorescent staining. The cells were thawed and cultured as described by the manufacturer. LECs were maintained in culture media with a low calcium concentration (30 M), as previously described [94]. At passage 0, the undifferentiated LECs were stained for $\Delta NP63\alpha$ and ABCG2 (LEC lot 1645759) or mechanically characterized by atomic force microscopy (LEC lot 1163447). Differentiated LECs were obtained by long-term in vitro culture (4 weeks, 2 passages; LEC lot 1163447). The differentiated LECs were either stained for $\Delta NP63\alpha$ and ABCG2 or mechanically characterized. The central cornea was dissected from a 70-year-old cadaveric human cornea within 36 h post-mortem (Georgia Eye Bank, IRB #10336-4). To obtain a dissociated cell suspension, the corneal tissue was cut into 2-4 mm pieces and incubated with 2.4 units/mL Dispase II (Roche Diagnostics, Risch-Rotkreuz, Switzerland) for 1 h at 37°C. Cells were recovered by incubation with 0.5 M ethylenediaminetetraacetic acid (EDTA; Invitrogen, Carlsbad, CA) for 10 min at 37°C, and enzymatic activity was arrested by the addition of serum-containing media.

4.3.2 Immunohistochemistry

LECs and differentiated LECs were adhered to glass coverslips, fixed with 4% paraformaldehyde, permeabilized in a buffer containing 0.5% Triton X-100, and blocked with 6% donkey serum and 0.3% Triton X-100 at room temperature for 1 h. Slides were incubated with primary antibody against human $\Delta NP63\alpha$ (Abcam, Cambridge, United Kingdom; #ab111449; 1:50) or ABCG2 (Abcam #ab24114; 1:20) overnight at 4°C, washed in phosphate buffered saline containing 0.05% Tween (PBST), and incubated with 488 or 594 DyLight-conjugated secondary antibody (Jackson Immunoresearch, West Grove, PA; 1:1000) for 1 h and 4',6-diamidino-2-phenylindole (DAPI; 1:10,000) for 5 min. Images were acquired using a Zeiss LSM510 confocal microscope and Zeiss AxioVision image acquisition software. Cadaveric human cornea tissue was fixed with 4% paraformaldehyde overnight. The tissue was dehydrated using an ethanol gradient (2 h each of 70%, 80%, 90%, 95%, and 100% ethanol) and then embedded in paraffin. 7 μm-thick sections were prepared on a microtome, dewaxed in xylene, and rehydrated through an ethanol gradient to distilled water. The tissue sections were mounted on glass slides, covered with 0.05% trypsin solution, incubated for 5 min at 37°C, and rinsed with PBST. The sections were then stained for $\Delta NP63\alpha$ and imaged, as described above. For clarity, the central cornea images were cropped to remove the stroma.

4.3.3 $\Delta NP63\alpha$ and ABCG2 Image Quantification

To verify the phenotype of each population, the percentage of $\Delta NP63\alpha^{bright}$ cells was quantified (Fig. 4.1A; LEC, n=335; differentiated LEC, n=297). ImageJ (National Institutes of Health, Bethesda, MD) was used to transform the images into the hue-saturation-brightness colour space and extract the brightness channel of both DAPI and $\Delta NP63\alpha$ images for further analysis. CellProfiler [21] was used to identify cell nuclei using the Otsu threshold method on the DAPI images. The $\Delta NP63\alpha$ staining

associated with each nucleus was determined using the background threshold method and the propagation method of secondary object identification [76], seeded by the previously identified nuclei. Cells with nuclei or associated $\Delta NP63\alpha$ staining that touched the border of the image were excluded from quantification. Since images were captured under 10x or 20x magnification, the intensity of the images was normalized by $\frac{NA^4}{M^2}$, where NA and M are the numerical aperture and magnification, respectively, of the objective. Cells were defined as $\Delta NP63\alpha^{bright}$ if the mean intensity exceeded 6.1% dynamic range, at which point the lower confidence interval bound of the diagnostic odds ratio was maximal (see Figs. 4.3D, 4.10E). The chosen threshold thus represents the point at which the confidence in a high diagnostic odds ratio is maximal.

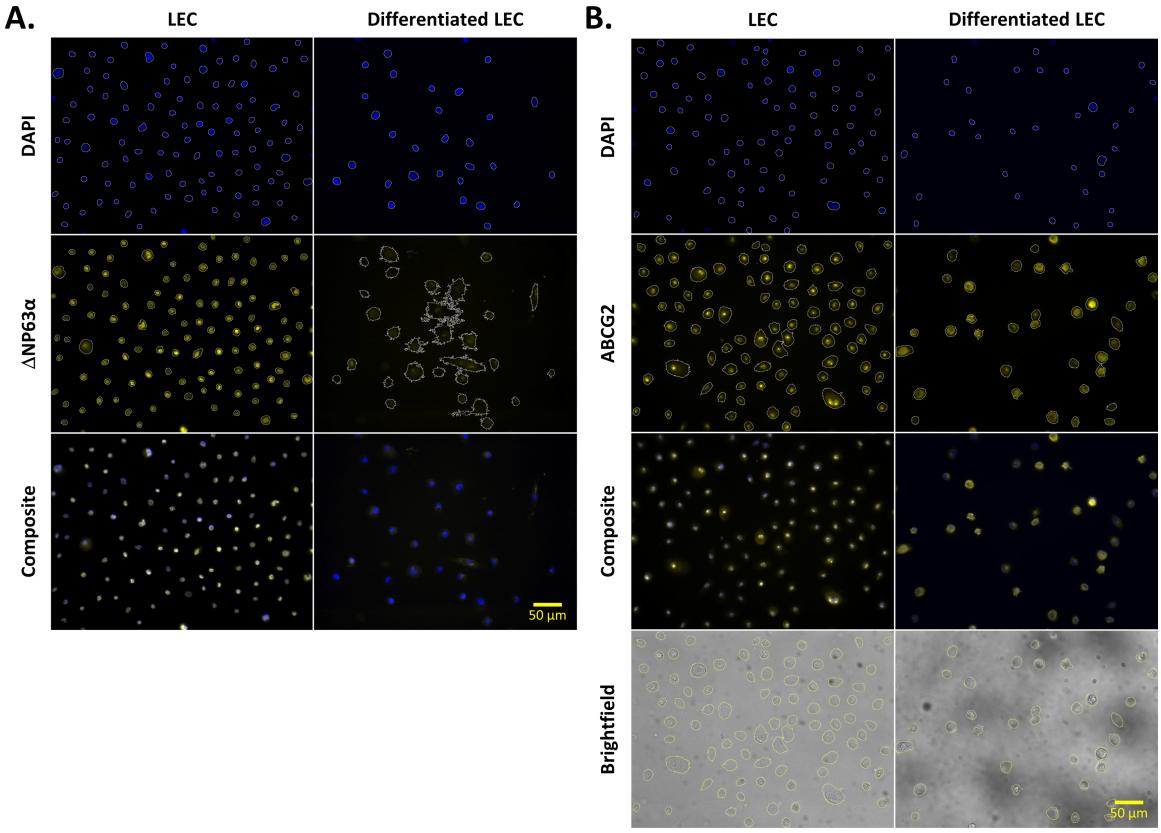

Figure 4.1: Image Quantification. The nuclei of limbal epithelial cells (LECs) and differentiated LECs were first stained with DAPI to serve as a seed for the identification of individual cells. The seeds were used to identify either the $\Delta NP63\alpha$-stained area (panel A, second row, white outlines), as identified by $\Delta NP63\alpha$ intensity (yellow), or the cytoplasmic area (panel B, second row, white outlines), as identified by ABCG2 (yellow). The cellular boundaries are similar whether defined by the brightfield images or the automatically identified cytoplasmic areas (panel B, fourth row, yellow outlines). Scale bars, 50 μm.

Similarly, ABCG2 images were used to identify the cytoplasmic region of each cell (Fig. 4.1B; LEC, n=248; differentiated LEC, n=113). The cytoplasmic area was used to quantify the diameter and aspect ratio of each cell. In combination with the nuclear area identified from the DAPI images, the cytoplasmic area was used to calculate the nucleus-to-cytoplasm ratio. The intact tissue images of the central cornea could not be quantified in comparison to the LECs and differentiated LECs due to the close cell proximity confounded by the high variability in sample thickness.

4.3.4 Atomic Force Microscopy

Cells were plated on poly-L-lysine-coated glass dishes and immobilized during 16-24 h incubation at 37°C. The LECs were immobilized in stem cell maintenance media until immediately before mechanical probing to discourage differentiation. To simplify the tip-cell contact geometry, 5.5 μm polystyrene beads were attached to tipless silica nitride cantilevers (Bruker Probes, Camarillo, CA) using two-part epoxy, and dried overnight. Mechanical properties of individual cells were obtained from force-indentation curves recorded with an atomic force microscope (Asylum Research, Santa Barbara, CA) with an integrated optical microscope (Nikon, Melville, NY) on a vibration isolation table. The Sader calibration method [123] was used to obtain cantilever spring constants ($k \approx 15$ pN/nm) based on the thermal vibration of the cantilever. The positions of the z-piezo and the cantilever deflection, Δx were acquired simultaneously (Fig. 4.2A, blue) to obtain the cell indentation, δ (red). The force, F, exerted on the cell was calculated using the cantilever spring constant, k, by $F = k \cdot \Delta x$. Mechanical analysis of the stiffness and viscoelastic properties is illustrated for an idealized cell in Figs. 4.2B–4.2E.

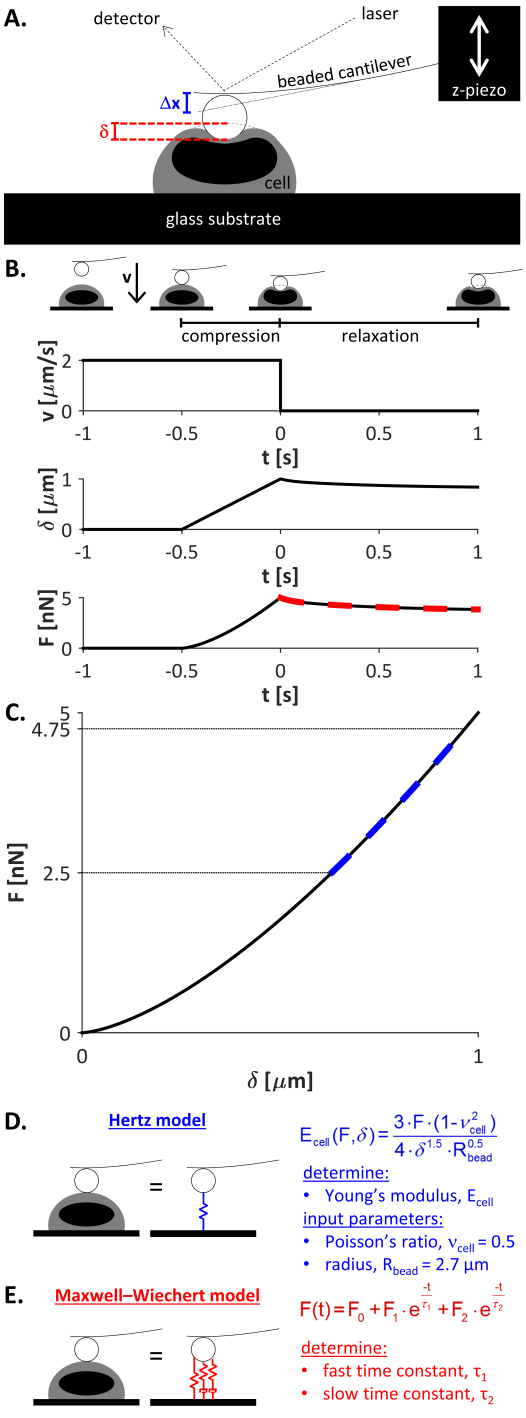
A.
detector
laser
beaded cantilever
z-piezo
Δx
δ
cell
glass substrate
B.
v
compression
relaxation
v [μm/s]
t [s]
δ [μm]
F [nN]
C.
F [nN]
δ [μm]
D.
Hertz model
$E_{cell}(F,\delta) = \frac{3 \cdot F \cdot (1-\nu_{cell}^2)}{4 \cdot \delta^{1.5} \cdot R_{bead}^{0.5}}$
determine:
• Young's modulus, E_{cell}
input parameters:
• Poisson's ratio, $\nu_{cell} = 0.5$
• radius, $R_{bead} = 2.7$ µm
E.
Maxwell–Wiechert model
$F(t) = F_0 + F_1 \cdot e^{\frac{-t}{\tau_1}} + F_2 \cdot e^{\frac{-t}{\tau_2}}$
determine:
• fast time constant, τ_1
• slow time constant, τ_2

Figure 4.2: Mechanical Phenotyping via Atomic Force Microscopy. A. A beaded cantilever was used to probe the mechanical properties of individual cells. The positions of the z-piezo and laser were used to calculate the cantilever deflection, Δx, and the indentation, δ. The force, F, exerted on the cell was calculated from the cantilever spring constant, k, by $F = k \cdot \Delta x$. Panels B-E illustrate the mechanical analysis of an idealized cell with an indentation-independent Young's modulus of 1.7 kPa. **B.** The cantilever was driven toward the cell with a velocity, v, of 2 $\frac{\mu m}{s}$. The increase in indentation at $t = -0.5$ s indicated cantilever-cell contact. The driving velocity was maintained to exert a compressive force on the cell until the force trigger of 5 nN was reached, completing the compression segment of the curve. The cantilever position was then maintained on the surface of the cell for 1 s while the unforced cellular relaxation response was recorded (relaxation segment). **C.** The compression segment of the force-indentation curve was used to determine the cellular Young's modulus, which is directly related to the slope of the curve. **D.** The Hertzian model, which describes sphere-sphere contact, was employed to calculate the cellular Young's modulus, E. The model was fit to the force-indentation curve over the range of 50-95% force (panel C, blue dashed line). **E.** The Maxwell-Wiechert model (with 2 Maxwell elements) was fit to the relaxation segment of the force-time curve (panel B, red dashed line) to calculate the viscoelastic time constants, τ_1 and τ_2.

The cantilever probe was visually aligned with the cell center and translated to indent the cell with a velocity of 2 μm/s (Fig. 4.2B). Contact between the cantilever and the cell was indicated by an increase in indentation. The translation velocity was maintained to exert a steadily increasing compressive force on the cell until a force trigger of 5 nN was reached, completing the compression segment of the curve. To examine the cell relaxation under compression, the cantilever dwelled at the surface of the compressed cell for 1 s by setting the translation velocity to 0 while the cellular relaxation response was recorded (relaxation segment).

4.3.5 Calculation of Young's Modulus

The Hertzian contact model, which describes the force-indentation relationship for deformable, sphere-sphere contact [161], was employed to calculate the cellular Young's modulus (Figs. 4.2C, 4.2D). The model was fit to the compression segment of the force-indentation curve over the applied force range of 2.5-4.75 nN, where the Young's modulus was largely independent of the indentation (Fig. 4.2C, blue dashed line). The

cells were assumed to be incompressible, such that the cellular Poisson's ratio was taken as 0.5. The Young's modulus was calculated as the average of 3 independent measurements taken in the same location on each cell with a pause between measurements so that each measurement produced consistent results.

4.3.6 Calculation of Viscoelastic Relaxation Constants

To calculate the viscoelastic properties of the cells, the spring-damper model was fit to the relaxation segment of the force-time curve (Fig. 4.2B, red dashed line), using the MaxwellWiechert model to calculate the viscoelastic time constants [127] (Fig. 4.2E). Two Maxwell elements were chosen to best fit the data. The fast and slow viscoelastic time constants were designated as 1 and 2, respectively. The viscoelastic properties of each cell were calculated as the averages of 3 independent measurements.

4.3.7 Calculation of Morphological Parameters

To calculate the diameter and aspect ratio of each cell based on the phase contrast images captured immediately following atomic force microscopy probing (see Fig. 4.4A), ImageJ was employed to manually draw a polygon around each cell. The diameter was calculated as the mean of the major and minor axes of the fit ellipse, and the aspect ratio was calculated as major axis divided by the minor axis.

4.3.8 Statistics and Figure Generation

Due to the non-normal distribution of each biophysical parameter (Shapiro-Wilk W Test, α=0.05), bootstrapping ANOVA was performed using a custom MATLAB code to discern statistically significant differences, as previously reported [19]. To assess significance, Holm's adjusted p values were compared to α=0.1. Spearman's rank correlation coefficients were used to assess the relationship between pairs of mechanical properties measured at the single-cell level (LEC, n=36; central cornea, n=40; differentiated LEC, n=60). Coefficients and raw p values were obtained using JMP

statistical software (SAS Institute, Cary, NC), and a custom Microsoft Excel spreadsheet was used to apply the Holm's adjustment and plot the resulting colour matrices (see Fig. 4.6B). Beeswarm plots (e.g., Fig. 4.3D) and semitransparent scatter plots (Fig. 4.6A) were generated using custom MATLAB codes.

4.3.9 Classifier Analysis

To assess the utility of the mechanical parameters as stemness indicators in comparison to conventional markers, each parameter was tested for the ability to distinguish stem-like from differentiated phenotypes. As prevalence-independent measurements, the true positive rate, false positive rate, and diagnostic odds ratio (DOR) were chosen to assess the binary classification of cells based on the parameters measured in the present study. To visualize the impact of the threshold value on the utility of each classifier, receiver operating curves were plotted by comparing the true and false positive rates for the full range of threshold values (see Figs. 4.8A–4.8C). The 95% confidence intervals of the receiver operating curves were calculated by bootstrapping using a custom MATLAB code. The confidence interval bounds of the DOR were calculated by $DOR \pm CI = e^{\ln(DOR) \pm a\sqrt{\frac{1}{TP}+\frac{1}{TN}+\frac{1}{FP}+\frac{1}{FN}}}$, where a is the inverse of the standard normal cumulative distribution evaluated at $1 - \frac{1-CI}{2}$, CI is the confidence interval, and TP, TN, FP, and FN are the frequencies of true positives, true negatives, false positives, and false negatives, respectively [56] (see Fig. 4.10A). Meta-analysis of previously published data [154–157] was used to establish the relationship between microfluidic sorting DORs and DORs based on adherent-cell Young's moduli (see Figs. 4.11, 4.12). For each pair of cell types considered, the soft cell type was taken as condition positive.

4.4 Results

4.4.1 Molecular Characterization

LECs, central cornea cells, and in vitro-differentiated LECs (Fig. 4.3A) were first compared for staining of molecular markers. The stemness of each cell type was assessed based on the percentage of cells that expressed the transcription factor $\Delta NP63\alpha$, a nuclear progenitor marker found in holoclones. In normal central corneal epithelia, $\Delta NP63\alpha$ protein expression is abundant in basal cells and decreases with differentiation [26, 77, 108]. As expected, the basal layer of the central cornea exhibited brighter $\Delta NP63\alpha$ than the apical layer (Fig. 4.3B). Furthermore, the LECs exhibited significantly higher mean $\Delta NP63\alpha$ intensity than the differentiated LECs (9.1% vs. 5.8% dynamic range; Figs. 4.3B–4.3D), indicating that the LECs decreased in stemness over the course of the four-week in vitro culture. 89.9% of LECs were $\Delta NP63\alpha^{bright}$, as expected considering the manufacturer's selection of a $\Delta NP63\alpha^{positive}$ cell population (Fig. 4.3D). Following extended culture, only 30.3% of the differentiated LECs were $\Delta NP63\alpha^{bright}$ (Fig. 4.3D), further supporting the successful differentiation of the LECs during extended culture.

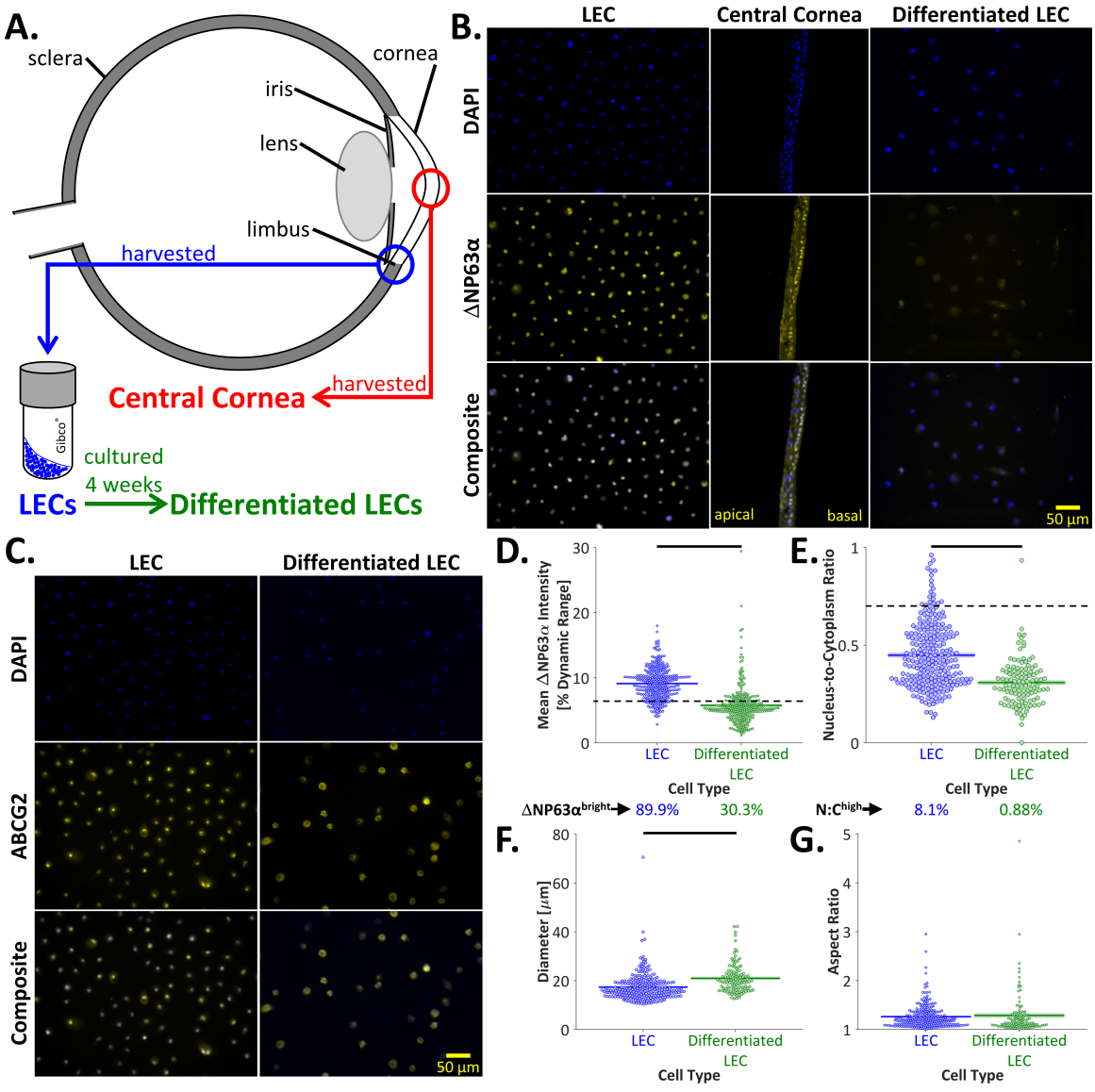
A.
sclera
cornea
iris
lens
limbus
harvested
harvested
Central Cornea
Gibco
cultured
4 weeks
LECs
Differentiated LECs
B.
LEC
Central Cornea
Differentiated LEC
DAPI
ΔNP63α
Composite
apical
basal
50 µm
C.
LEC
Differentiated LEC
DAPI
ABCG2
Composite
50 µm
D.
Mean ΔNP63α Intensity [% Dynamic Range]
30
20
10
0
LEC
Differentiated LEC
Cell Type
E.
Nucleus-to-Cytoplasm Ratio
1
0.5
0
LEC
Differentiated LEC
Cell Type
ΔNP63α^bright
89.9%
30.3%
N:C^high
8.1%
0.88%
F.
Diameter [µm]
80
60
40
20
0
LEC
Differentiated LEC
Cell Type
G.
Aspect Ratio
5
4
3
2
1
LEC
Differentiated LEC
Cell Type

Figure 4.3: Molecular Characterization. **A.** Limbal epithelial cells (LECs, blue) were harvested from the corneal limbus. Differentiated LECs (green) were obtained by culturing the LECs in vitro for 4 weeks. Central cornea cells (red) were harvested from human corneas. **B.** Dissociated LECs, intact central cornea tissue, and dissociated differentiated LECs were stained for nuclear material (DAPI, blue) and the progenitor marker $\Delta NP63\alpha$ (yellow). The stem-like LECs stained more brightly for $\Delta NP63\alpha$ than the differentiated LECs. The central cornea tissue displayed a basal layer of stem-like $\Delta NP63\alpha^{bright}$ cells, whereas the differentiated apical cells were $\Delta NP63\alpha^{dim}$. **C.** To identify the nuclear and cytoplasmic area of the dissociated LECs and differentiated LECs, cells were stained for nuclear material (DAPI, blue) and the cell membrane marker ABCG2 (yellow). Scale bars, 50 μm. **D.** $\Delta NP63\alpha$ was significantly brighter for LECs (blue) than differentiated LECs (green, $p < 10^{-6}$), and a higher percentage of $\Delta NP63\alpha^{bright}$ cells was observed in LECs than differentiated LECs, indicating a decreased percentage of stem-like cells following the 4-week in vitro culture. **E.** The nucleus-to-cytoplasm area ratio, as determined by DAPI and ABCG2 staining, was significantly higher in LECs than differentiated LECs ($p < 10^{-6}$). 8.1% of LECs and 0.88% of differentiated LECs displayed nucleus-to-cytoplasm ratios above the previously described threshold of 0.7 [5], further supporting the higher prevalence of stem-like cells in the LEC population. **F.** The differentiated LECs were significantly larger than the LECs ($p < 10^{-6}$), as quantified by the ABCG2 cytoplasmic stain. **G.** The aspect ratio was not significantly different for LECs and differentiated LECs ($p = 0.61$).

Quantification of the DAPI nuclear stain and ABCG2 cytoplasmic stain (Fig. 4.3C) enabled the calculation of nucleus-to-cytoplasm ratio, diameter, and aspect ratio for each LEC and differentiated LEC. The nucleus-to-cytoplasm ratio was significantly higher for the LECs than the differentiated LECs (Fig. 4.3E). In agreement with a previous study that specifies a nucleus-to-cytoplasm ratio cutoff of 0.7 [5], 8.1% of LECs and 0.88% of differentiated LECs exhibited a high nucleus-to-cytoplasm ratio. The LECs were significantly smaller than the differentiated LECs (Fig. 4.3F), but the cellular aspect ratios were not significantly different (Fig. 4.3G).

4.4.2 Cell Mechanics

The LECs exhibited significantly lower Young's moduli than both the central cornea cells and the differentiated LECs (Figs. 4.4B, 4.5A), indicating that cell stiffness may be used as a stemness indicator for cells derived from the corneal limbus. The

differentiated LECs were significantly larger than the LECs and the central cornea cells, and the LECs were significantly larger than the central cornea cells (Fig. 4.5B). However, there were no significant differences among the cell populations with respect to aspect ratio (Fig. 4.5C) or the fast viscoelastic time constant, 1 (Figs. 4.4C, 4.5D). The slow viscoelastic time constant, 2, was significantly lower for the LECs than the differentiated LECs (Figs. 4.4C, 4.5E), indicating a more viscous behaviour for the differentiated LECs. However, the slow viscoelastic time constant cannot be regarded as an ideal stemness marker because the difference between the LECs and central cornea cells was not significant. Overall, neither aspect ratio nor the viscoelastic time constants serve as specific markers of limbal cell stemness.

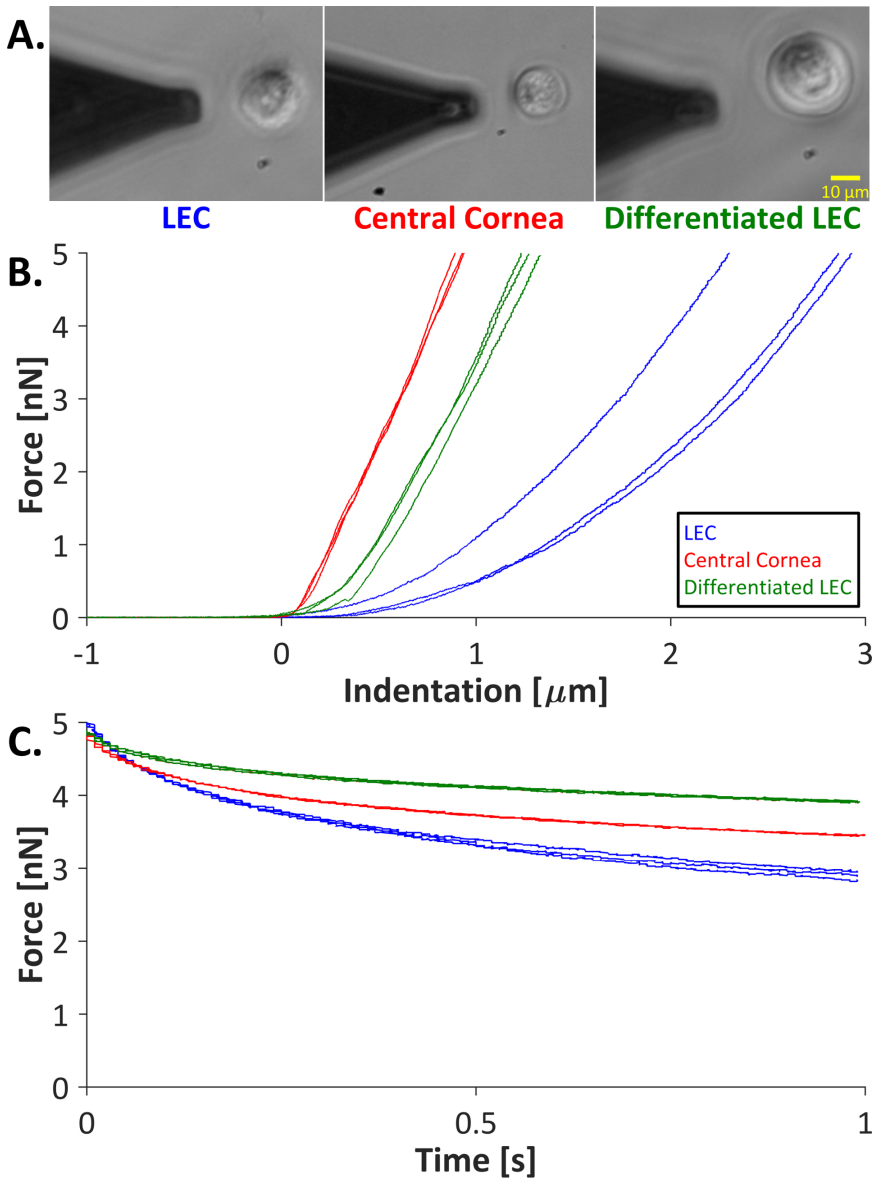

Figure 4.4: Mechanical Phenotyping via Atomic Force Microscopy. **A.** Phase contrast microscopy was used both to position the cantilever over each individual cell and to measure the diameter and aspect ratio of each cell. Scale bar, 10 μm. **B.** Given the direct relationship between cellular Young's modulus and the slope of the force-indentation curve, representative force-indentation curves indicated that the LECs (blue) were softer than the central cornea cells (red) and differentiated LECs (green). **C.** Force-time curves obtained during cell relaxation indicated the viscoelastic properties of the cells. The fast viscoelastic time constant, τ_1, which is inversely related to the slope at the minimum time (t=0 s), was similar for all cell types. The slow viscoelastic time constant, τ_2, which is inversely related to the slope at the maximum time (t=1 s), was qualitatively higher for the differentiated LECs than the LECs and central cornea cells.

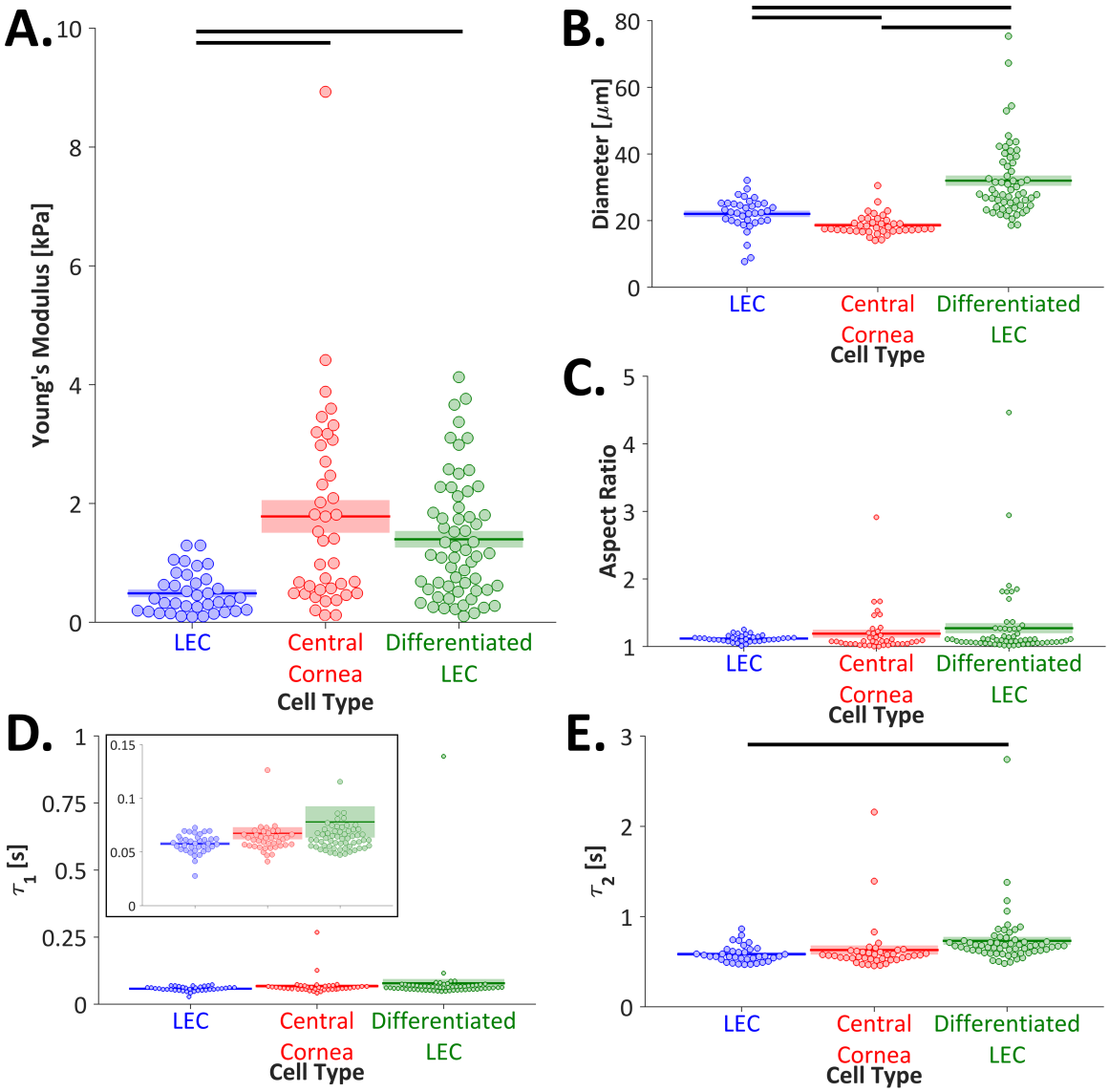

Figure 4.5: Cell Mechanics. A. The LECs were significantly softer than both the central cornea cells ($p_{adjusted}$=0.001) and differentiated LECs ($p_{adjusted} < 10^{-6}$), suggesting that Young's modulus may be used as an indicator for the differentiation state of limbal epithelial cells. **B.** The LECs were significantly larger than the central cornea cells ($p_{adjusted} < 10^{-6}$), but significantly smaller than the differentiated LECs ($p_{adjusted} < 10^{-6}$). The central cornea cells were significantly smaller than the differentiated LECs ($p_{adjusted} < 10^{-6}$). **C–D.** There were no significant differences in aspect ratio or the fast viscoelastic time constant, τ_1. **E.** The LECs had a significantly lower slow viscoelastic time constant, τ_2, than the differentiated LECs ($p_{adjusted}$=0.043). Due to the non-normal distribution of each population (Shapiro-Wilk W Test, α=0.05), bootstrapping ANOVA was used to discern statistically significant differences. Populations connected by black bars are significantly different (Holm's adjusted p-values, α=0.10).

To investigate the relationships between each pair of the mechanical properties, the parameters were compared for each cell type measured (Fig. 4.6A). Cells with the highest aspect ratios (>2) were observed to have low viscoelastic time constants, and cells with the highest viscoelastic time constants tended to have low aspect ratios (<2). However, strong relationships were not observed for any pair of mechanical parameters (Fig. 4.6B), suggesting the potential use of multiple parameters in combination to isolate cell populations of interest. There was a significant, but weak, relationship between the two viscoelastic time constants whether the cell types were considered together or individually (Fig. 4.6B). Interestingly, the Young's modulus and diameter were highly negatively correlated for central cornea cells, but not for LECs, differentiated cells, or all cell types considered together (Fig. 4.6B).

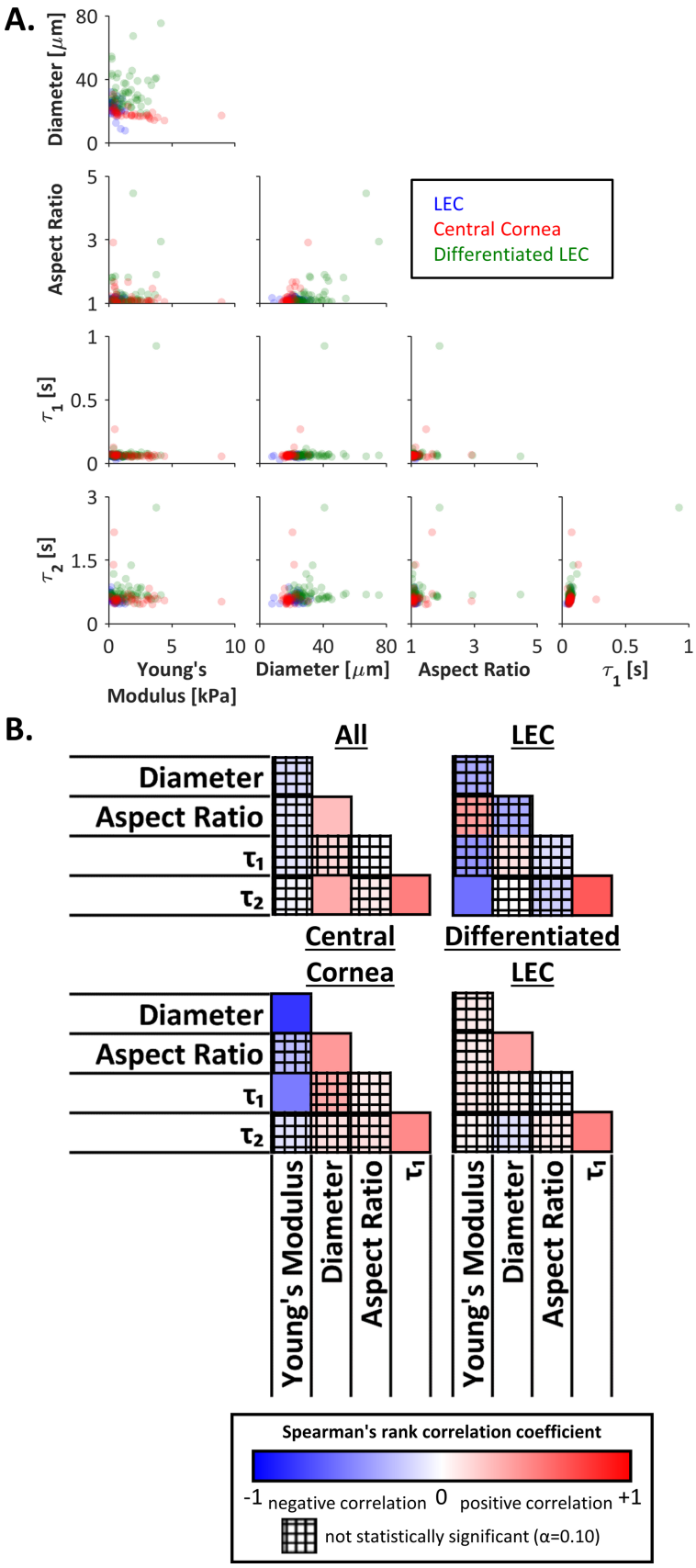
A.
Diameter [μm]
Aspect Ratio
τ1 [s]
τ2 [s]
LEC
Central Cornea
Differentiated LEC
Young's Modulus [kPa]
Diameter [μm]
Aspect Ratio
τ1 [s]
B.
All
LEC
Central Cornea
Differentiated LEC
Diameter
Aspect Ratio
τ1
τ2
Young's Modulus
Spearman's rank correlation coefficient
-1 negative correlation 0 positive correlation +1
not statistically significant (α=0.10)

Figure 4.6: Pairwise Cell Mechanics Comparisons. A. The weak relationships between pairs of mechanical properties indicated that each property may be used independently to identify or isolate a cell population of interest (LEC, blue, n=36; central cornea, red, n=40; differentiated LEC, green, n=60). **B.** The pairwise Spearman's correlation coefficients among the 5 mechanical parameters for all cells (top-left), LECs only (top-right), central cornea cells only (bottom-left), and differentiated LECs only (bottom-right) indicated that correlations were generally weak or not significant. In all cases, the two viscoelastic parameters were positively associated. Interestingly, the Young's modulus and diameter were highly negatively correlated for central cornea cells, but not for LECs, differentiated cells, or all cell types considered together. Spearman's rank correlation coefficients range from -1 (bright blue) to +1 (bright red). The crosshatch pattern indicates a correlation that was not statistically significant based on Holm's adjusted p-values (α=0.10).

4.5 Discussion

For the first time, the mechanical properties of cells derived from the corneal limbus were characterized. The LECs, which were shown to be stem-like based on the high percentage of $\Delta NP63\alpha^{bright}$ cells, were significantly softer than both the central cornea cells and the in vitro-differentiated LECs. Therefore, cell stiffness can be used as a stemness indicator for cells derived from the corneal limbus. Previous studies of stem cell mechanics have shown various properties to change during differentiation. Overall, mechanical comparisons of stem cells and their progeny reveal that cells with epithelial-like morphologies are softer than cells with mesenchymal-like morphologies [34,112]. The epithelial-to-mesenchymal transition observed during limbal epithelial cell differentiation, coupled with the present finding of a corresponding stiffness increase, further supports the contention that cells of mesenchymal morphology are stiffer than epithelial cells. In comparison, the mechanical changes are less clear for cell types that remain mesenchymal-like during differentiation, such as mesenchymal stem cell differentiation to osteoblast lineages [19,34,165]. Studies in which corneal cells were grown on substrates of varying stiffnesses support the finding that the stem-like limbal cells are relatively soft. Corneal epithelial cells grown on low stiffness substrates exhibited the early differentiation marker cytokeratin 19, whereas

cells grown on high stiffness substrates expressed the late differentiation markers cytokeratins 3 and 12 [23,97]. Furthermore, previous studies indicate that the basement membrane is softer than the apical Bowman's layer [86] and that limbal tissue is softer than central cornea tissue [111]. Since cells are known to modulate F-actin organization, and thereby alter their stiffness, in response to the stiffness of the underlying substrate [130], the finding that the limbal niche is softer than the central cornea niche supports the contention that the Young's modulus results reflect differences between the in vivo mechanical environments of the stem-like and differentiated cell types. The slow viscoelastic time constant changed during in vitro differentiation, but the fast viscoelastic time constant did not, suggesting that distinct cellular structures may dominantly underpin each viscoelastic time constant. The nucleus is known to be several orders of magnitude more viscous than the cytoskeleton ($\mu_{nucleus} \approx 5kPa \cdot s$ [63], $\mu_{actin} \approx 1-10mPa \cdot s$ [153], $\mu_{microtubule} 1-100mPa \cdot s$ [153]). Therefore, the observed increase in nuclear area during in vitro LEC differentiation (Fig. 4.7) may partially explain the concomitant increase observed in the slow viscoelastic time constant. Furthermore, a recent study of fibroblasts, which also employed a two time constant relaxation model, found that the actin network governs relaxation behaviour over shorter time scales, whereas the intermediate filament network dictates long-term relaxation [50]. Thus, intermediate filament rearrangement during limbal cell differentiation may play a dominant role in cell relaxation compared to actin rearrangement. Interestingly, cytokeratins 3, 12, and 19, which comprise type I and II intermediate filaments, are commonly used to identify stemness in the limbus [23,97], further emphasising a potential relationship between intermediate filament structure and mechanical properties.

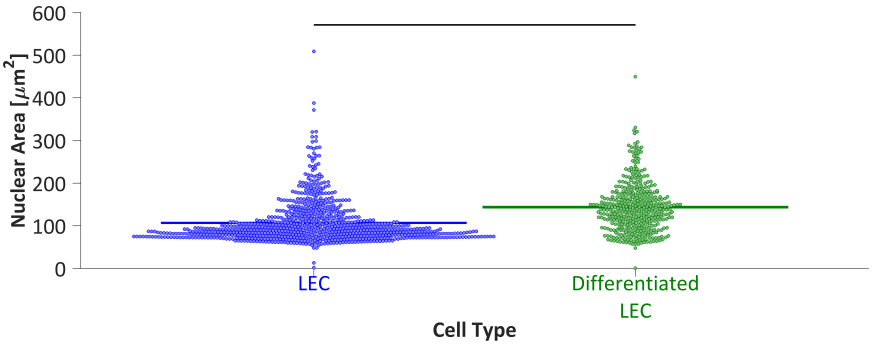

Figure 4.7: Nuclear Area. The nuclear area, as measured from DAPI channel images taken during $\Delta NP63\alpha$ and ABCG2 staining, was significantly higher for differentiated LECs than LECs ($p < 10^{-6}$).

The finding that the differentiated LECs were larger than both the LECs and the central cornea cells is supported by the finding that cells increase in size over the course of in vitro differentiation due to external stressors and the lack of 3D spatial restrictions [120]. The finding that the LECs were larger than the central cornea cells (Fig. 4.5B) conflicts with a previous study that found LECs to be smaller than central cornea cells [118]. However, the previous study used flow cytometry to measure the size of dissociated cells ex vivo as well as in vivo confocal microscopy to investigate only the most basal and superficial layers of intact epithelial tissue [118], whereas the present data refer to rounded, immobilized cells that represent the entirety of each anatomical region. Furthermore, the distribution of cell diameters (Fig. 4.5B) indicated that the LECs include a portion of smaller cells with no counterpart in the central cornea population, similarly to the previously presented data [118]. Quantification of the ABCG2 cell membrane stain and the atomic force microscopy phase contrast images both indicated an increase in cell diameter, with no significant change to aspect ratio, during in vitro LEC differentiation (Figs. 4.3F, 4.3G, 4.5B, 4.5C). Although the LEC diameters were similar (approximately 20 m) for both methods, quantification of the differentiated LEC phase contrast images yielded a 50% larger average diameter than quantification of the ABCG2 images. The apparent diameter discrepancy can be explained by differences in surface coatings, which are known to

affect cell morphology [54, 88, 132, 164], as cells were plated on poly-L-lysine-coated glass for the phase contrast images and on uncoated glass for the ABCG2 images. To determine the utility of each mechanical property as a novel biomarker, each parameter was analysed as a binary classifier of stemness. For a chosen threshold, a contingency table was constructed to compare the test condition to the actual condition (Figs. 4.8A, 4.8B). Receiver operating curves were plotted by calculating the true and false positive rates for the full range of classifier values (Fig. 4.8C). The parameters that best classified stemness (i.e. separated LECs from differentiated LECs) were Young's modulus (Fig. 4.8D), diameter (Fig. 4.8E), the slow viscoelastic time constant (Fig. 4.8F), mean $\Delta NP63\alpha$ intensity (Fig. 4.8G), and nucleus-to-cytoplasm ratio (Fig. 4.8H). The aspect ratio (Fig. 4.9A) and fast viscoelastic time constant (Fig. 4.9B) did not successfully indicate stemness.

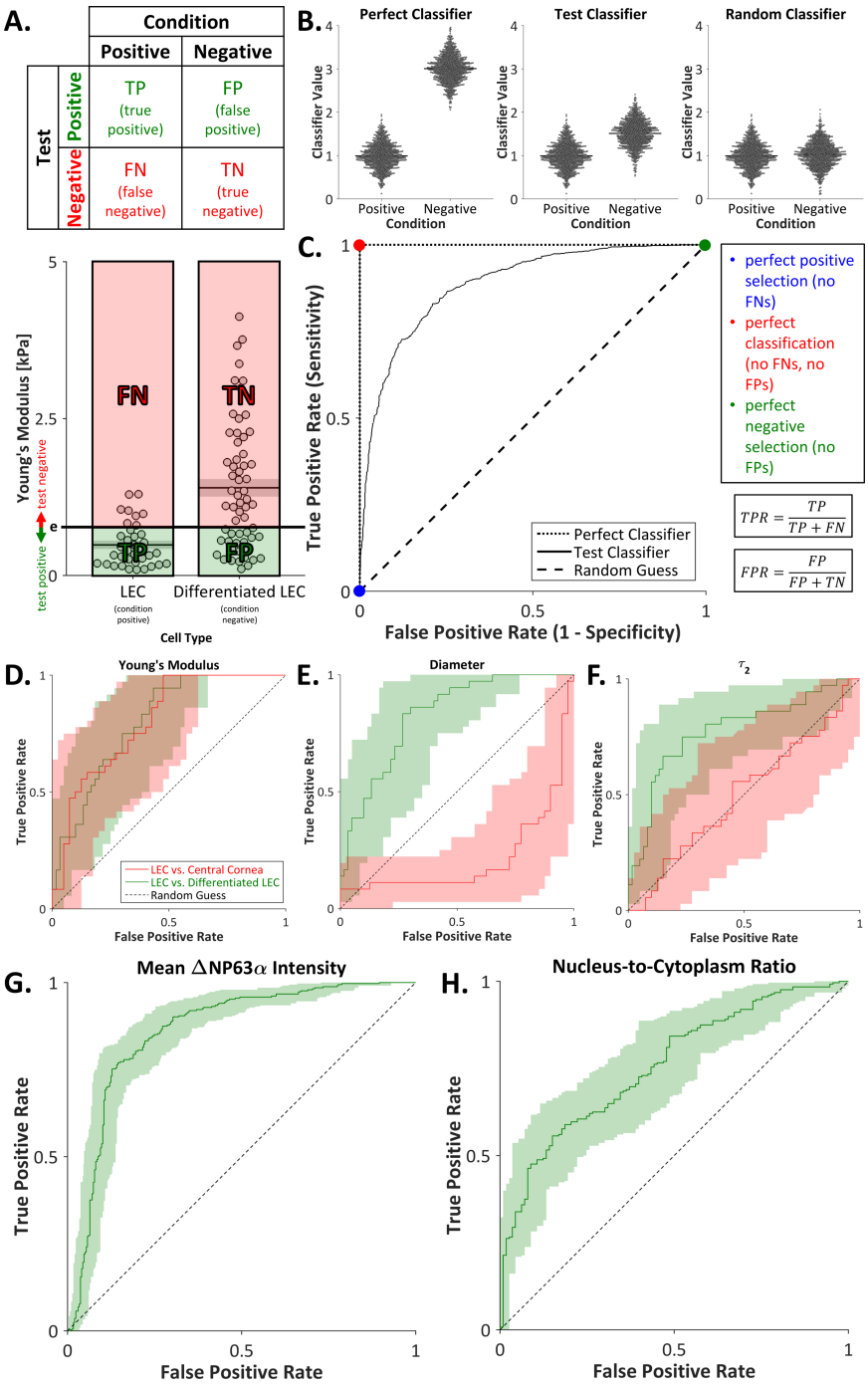
A.
Condition
Positive
Negative
Test
Positive
Negative
TP (true positive)
FP (false positive)
FN (false negative)
TN (true negative)
B.
Perfect Classifier
Test Classifier
Random Classifier
Classifier Value
Positive
Negative
Condition
C.
True Positive Rate (Sensitivity)
False Positive Rate (1 - Specificity)
Perfect Classifier
Test Classifier
Random Guess
perfect positive selection (no FNs)
perfect classification (no FNs, no FPs)
perfect negative selection (no FPs)
$TPR = \frac{TP}{TP + FN}$
$FPR = \frac{FP}{FP + TN}$
Young's Modulus [kPa]
test negative
test positive
FN
TN
TP
FP
LEC
(condition positive)
Differentiated LEC
(condition negative)
Cell Type
D.
Young's Modulus
E.
Diameter
F.
τ_2
True Positive Rate
False Positive Rate
LEC vs. Central Cornea
LEC vs. Differentiated LEC
Random Guess
G.
Mean ΔNP63α Intensity
H.
Nucleus-to-Cytoplasm Ratio

Figure 4.8: Receiver Operating Characteristic (ROC) Curves. A. For a binary classifier, the contingency table separates test subjects into true positives (TPs), false positives (FPs), false negatives (FNs), and true negatives (TNs). Young's modulus was used to select for limbal epithelial cells (LECs, condition positive) and against differentiated LECs (condition negative). Cells below and above the threshold Young's modulus (e) were considered to be test positive (green) and test negative (red), respectively. **B.** A perfect classifier would enable perfect discrimination between condition positive and condition negative cells (no FPs, no FNs), whereas a random classifier would enable no discrimination between condition positive and condition negative cells (TPs=FPs, TNs=FNs). In practice, the threshold value of a test classifier can be shifted to improve positive selection at the cost of reduced negative selection, or vice-versa. **C.** ROC curves (black lines and panels D-H) were generated by calculating the true positive rate (TPR) and the false positive rate (FPR) for all possible threshold values. The ROC curve for a test classifier (solid line) lies between the ROC curves for a perfect classifier (dotted line) and a random guess (dashed line). **D–H.** ROC curves for the selection of LECs against either central cornea cells (red) or differentiated LECs (green) using the test positive conditions of D) low Young's modulus, E) low diameter, F) low slow viscoelastic time constant (τ_2), G) high mean $\Delta NP63\alpha$ intensity, or H) high nucleus-to-cytoplasm ratio indicated that each parameter can be used to discern stemness. Shaded regions indicate 95% confidence interval.

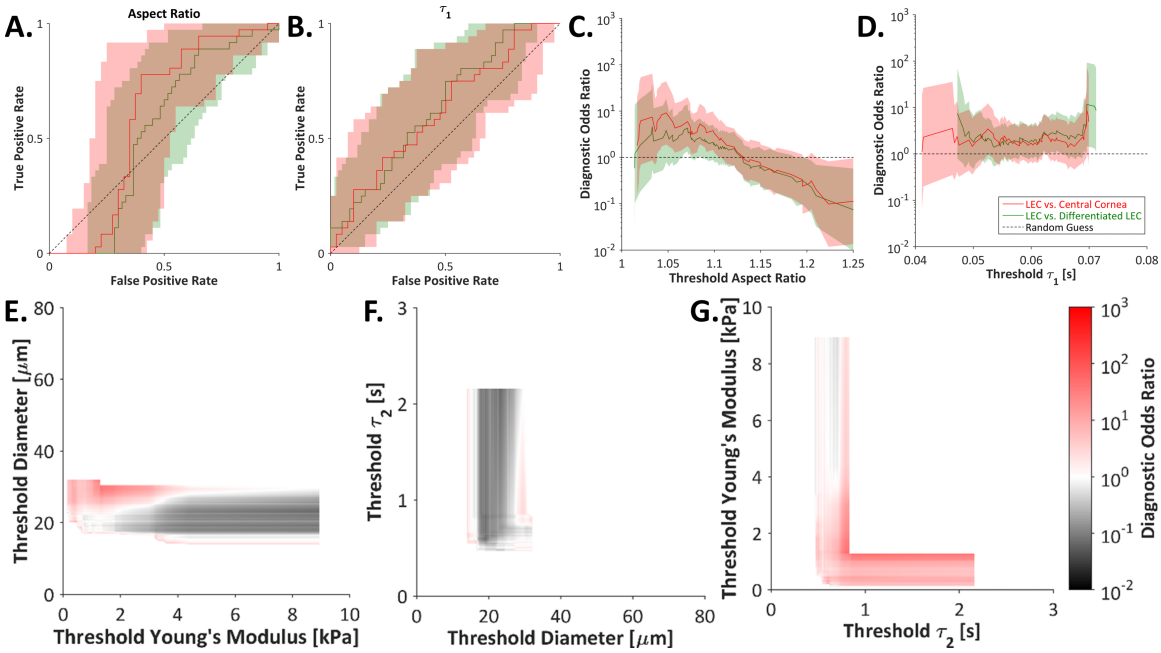

Figure 4.9: Receiver Operating Characteristic (ROC) Curves. A–B. Selection for limbal epithelial cells (LECs) against central cornea cells (red) or differentiated LECs (green) on the basis of A) aspect ratio and B) the fast viscoelastic time constant (τ_1) was poor, as indicated by areas under the curve of only marginally greater than 0.5, which is the area under the curve for a random classifier. **C–D.** The low diagnostic odds ratios (DORs) for classifiers based on C) the aspect ratio and D) the fast viscoelastic time constant further indicate the poor quality of classification. **E–G.** For all possible combinations of E) threshold diameter and threshold Young's modulus, F) threshold slow viscoelastic time constant (2) and threshold diameter, and G) threshold Young's modulus and threshold slow viscoelastic time constant, the DOR was calculated for selection of LECs against central cornea cells. Overall, the DORs were lower for selection of LECs against central cornea cells than against differentiated LECs (Figs. 4.10H–4.10J). The DORs ranged from 0.01 (black) to 1 (white) to 1000 (bright red).

To further understand the binary classification, the diagnostic odds ratio (DOR) was chosen as a single parameter that summarizes the true and false positive rates (Fig. 4.10A). The Young's modulus performed well in the selection of LECs against both central cornea cells and differentiated LECs (Fig. 4.10B), but classification on the basis of diameter or the slow viscoelastic time constant succeeded only in the selection of LECs against differentiated LECs (Figs. 4.10C, 4.10D). The maximum DORs for the selection of LECs against differentiated LECs on the basis of mean $\Delta NP63\alpha$

intensity was approximately 90 (Fig. 4.10E & Table 4.1), indicating that the odds of a positive stemness test among LECs is 90 times higher than the odds of a positive stemness test among differentiated LECs [56]. In comparison, the maximum DOR was approximately 30 for selection on the bases of the nucleus-to-cytoplasm ratio, Young's modulus, or diameter and approximately 14 for selection on the basis of the slow viscoelastic time constant (Figs. 4.10B–4.10D, 4.10F & Table 4.1). However, the DORs for classification based on the aspect ratio (Fig. 4.9C & Table 4.1) or the fast viscoelastic time constant (Fig. 4.9D & Table 4.1) were relatively low, further corroborating the finding that the aspect ratio and fast viscoelastic time constant were not suitable stemness indicators.

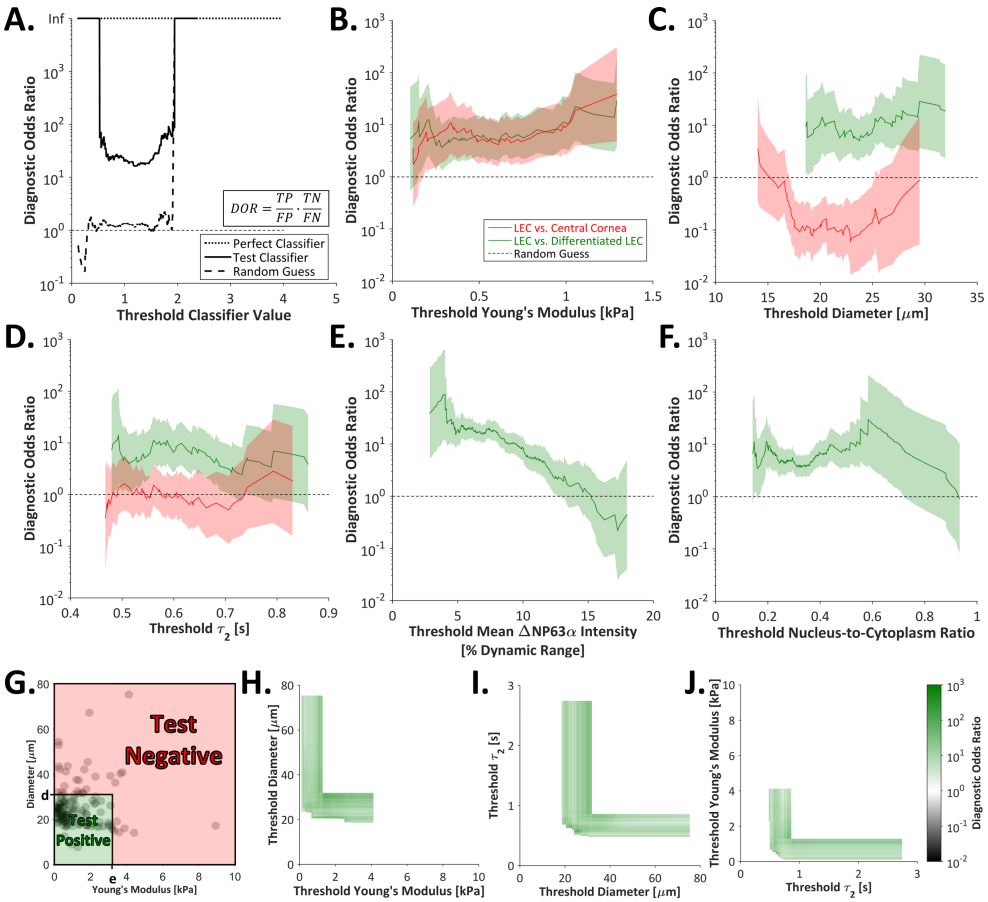

Figure 4.10: Diagnostic Odds Ratio (DOR). A. The DOR measures the overall utility of a binary classifier by $\frac{TP \cdot TN}{FP \cdot FN}$. The DOR of a perfect classifier (dotted line) is infinite for any threshold value, whereas the DOR of a random classifier (dashed line) is approximately 1, and a test classifier (solid line) will have a finite DOR>1. Extreme threshold classifier values yield an infinite DOR (where FP=0 or FN=0). **B–F.** The DORs based on B) Young's modulus, C) diameter, D) slow viscoelastic time constant, E) mean $\Delta NP63\alpha$ intensity, and F) nucleus-to-cytoplasm ratio were generally higher for the selection of LECs against differentiated LECs (green) than against central cornea cells (red). The DOR based on Young's modulus was approximately 10, regardless of the threshold value. Shaded regions indicate 95% confidence interval. **G.** To determine the utility of a two-parameter classifier, cells below both the diameter threshold, d, and the Young's modulus threshold, e, were defined as test positive (green). All other cells were defined as test negative (red). **H–J.** For all possible combinations of H) threshold diameter and threshold Young's modulus, I) threshold slow viscoelastic time constant (τ_2) and threshold diameter, and J) threshold Young's modulus and threshold slow viscoelastic time constant, the DOR was calculated for selection of LECs against differentiated LECs. The increase in DOR upon including a second classifier indicates that the combined classifiers can outperform the single parameter classifiers. The DORs ranged from 0.01 (black) to 1 (white) to 1000 (bright green).

Table 4.1: Diagnostic Odds Ratios for Single Parameters. For each parameter, the maximum and mean diagnostic odds ratios (DORs) were calculated for classifying limbal epithelial cells (LECs) versus differentiated LECs or central cornea cells. The DOR of a perfect classifier is infinite for any threshold value, whereas the DOR of a random classifier is approximately 1, and a test classifier will have a finite DOR>1. τ_1, fast viscoelastic time constant; τ_2, slow viscoelastic time constant.

	Maximum DOR		Mean DOR	
	LEC vs. Differentiated LEC	LEC vs. Central Cornea	LEC vs. Differentiated LEC	LEC vs. Central Cornea
Mean $\Delta NP63\alpha$ Intensity	89.92		16.82	
Nucleus-to-Cytoplasm Ratio	30.44		7.80	
Young's Modulus	28.64	38.68	8.30	7.11
Diameter	28.64	3.55	11.31	0.28
Aspect Ratio	4.62	9.15	1.94	2.96
τ_1	11.67	8.75	2.75	2.31
τ_2	14.24	2.84	6.37	1.03

In addition to the DOR, the area under the receiver operating characteristic curve is commonly used to measure the utility of a classifier. The areas under the curve data support the DOR-based finding that mean $\Delta NP63\alpha$ intensity, diameter, and Young's modulus best identify LECs from a mixed population containing differentiated LECs (Table 4.2).

Table 4.2: Area under the Receiver Operating Curves. For each parameter, the area under the receiver operating curve was calculated for classifying limbal epithelial cells (LECs) versus differentiated LECs or central cornea cells. The area under the curve of a useful test ranges from 0.5 (random classification) to 1 (perfect classification). τ_1, fast viscoelastic time constant; τ_2, slow viscoelastic time constant; CI, confidence interval.

	LEC vs. Differentiated LEC			LEC vs. Central Cornea		
	Area Under Curve	Lower 95% CI	Upper 95% CI	Area Under Curve	Lower 95% CI	Upper 95% CI
Mean $\Delta NP63\alpha$ Intensity	0.860	0.800	0.913			
Nucleus-to-Cytoplasm Ratio	0.757	0.654	0.847			
Young's Modulus	0.801	0.626	0.928	0.802	0.607	0.943
Diameter	0.827	0.654	0.947	0.216	0.051	0.422
Aspect Ratio	0.531	0.344	0.725	0.597	0.381	0.805
τ_1	0.637	0.422	0.823	0.615	0.370	0.827
τ_2	0.777	0.578	0.931	0.500	0.263	0.743

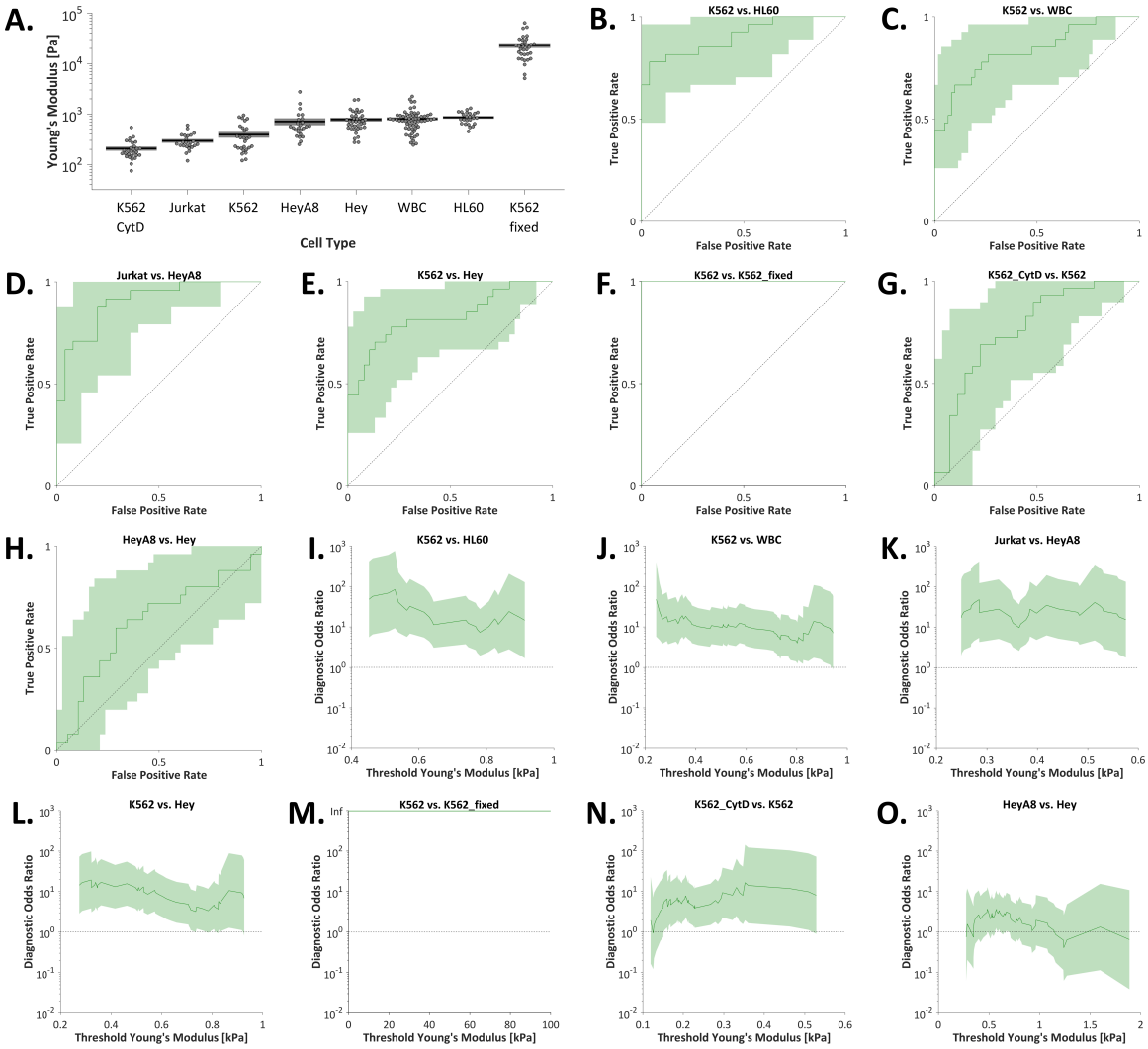

Figure 4.11: Differences in Adherent Cell Young's Moduli are Correlated with the Microfluidic Sorting Diagnostic Odds Ratio. A–G. Cellular Young's moduli ranged from 0.1-100 kPa for cell lines previously sorted using microfluidic technology. **H–N.** For various combinations of cell types, the receiver operating curves based on adherent-cell Young's modulus yielded areas under the curve ranging from 0.626 (H, HeyA8 vs. Hey) to 1 (F, K562 vs. $K562_{fixed}$), where the soft cell type was taken as condition positive. **O.** The maximum diagnostic odds ratio (DOR) based on adherent-cell Young's modulus ranged from 3.713 (O, HeyA8 vs. Hey) to infinity (M, K562 vs. $K562_{fixed}$). Shaded regions indicate 95% confidence interval. WBC, white blood cell; fixed, treatment with 4% paraformaldehyde; CytD, treatment with 2 μM cytochalasin-D. Pre-sort Young's moduli of various cell types (Panel B) replotted from [154–157]. Young's modulus ROC and DOR curves (C-J) calculated from previously published data [154–157].

Previous results further evidence the relationship between adherent cell atomic

force microscopy and microfluidic sorting ability; mechanics data from adhered cells correlate with sorting trajectories within our device, and cells taken from the outlets of our device display distinct mechanical properties after attachment [156]. Specifically, the relatively soft and low viscosity K562 cells have been efficiently sorted from either HL60 cells (sorting DOR = 205 [157]) or leukocytes (sorting DOR = 12.7 [155]). The similar relative mechanical properties reported in the limbal system suggest the applicability of microfluidic sorting technology to enrich for limbal stem-like cells. To quantitatively elucidate the relationship between the adherent cell Young's modulus-based DOR and sorting ability, a meta-analysis of previously published data was conducted (Figs. 4.11, 4.12). The positive correlations between the microfluidic sorting DORs and the DORs predicted from Young's modulus (maximum DOR, ρ=0.831, p=0.011; mean DOR, ρ=0.850, p=0.007; AUC, ρ=0.850, p=0.007) provide evidence that the high Young's modulus-based DORs observed in the limbal system indicate an ability to enrich for stem-like cells form the limbal niche using microfluidics.

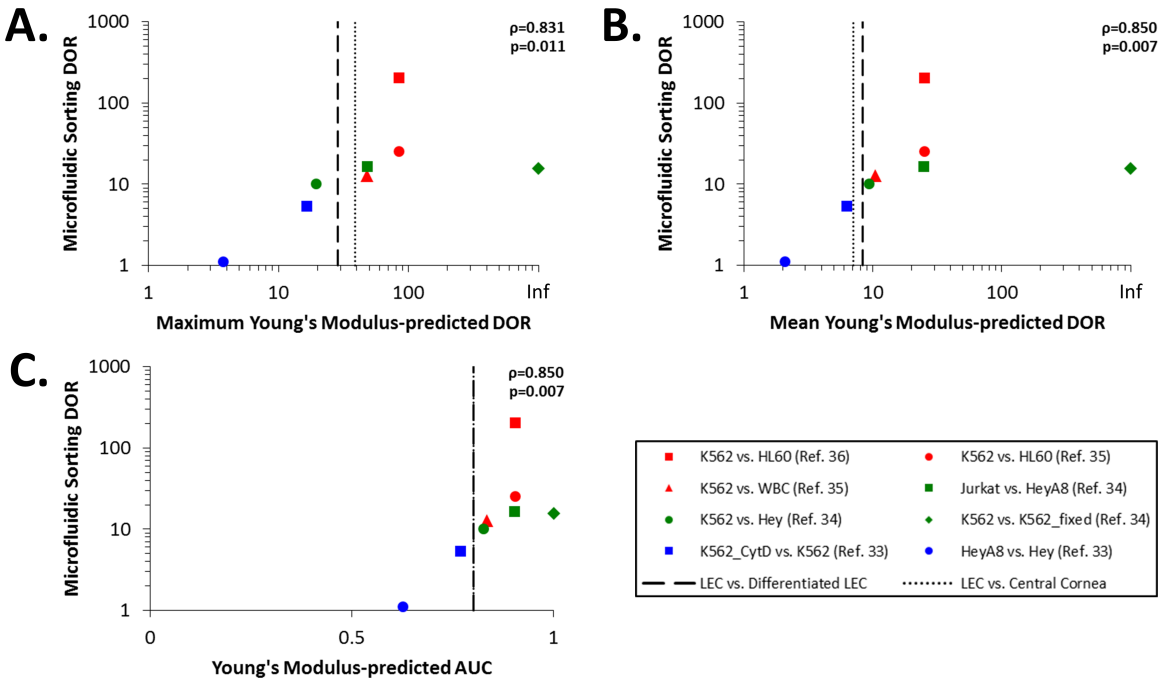

Figure 4.12: Correlation between Adherent Cell Mechanics and Microfluidic Sorting. Sorting for stem-like cells from the limbal region (black vertical lines) is projected to yield a microfluidic sorting DOR of approximately 10, based on positive correlations between microfluidic sorting DORs and either A) the maximum Young's modulus-predicted DOR (ρ=0.831, p=0.11), B) the mean Young's modulus-predicted DOR (ρ=0.850, p=0.007), or C) the area under the curve (AUC) of the Young's modulus receiver operating characteristic (ρ=0.850, p=0.007). DORs and AUCs calculated from previously published data [154–157]. Spearman's correlation coefficient was calculated to test for monotonic trends.

Evaluating parameters on the single-cell level enabled combined classifier analysis. Thus, given the positive performance of Young's modulus, diameter, and the slow viscoelastic time constant as stemness classifiers, the performance of pairwise classifiers was also assessed. Cells with both parameters below the respective thresholds were taken as test positive, and the remainder were taken as test negative (Fig. 4.10G). For Young's modulus, diameter, and the slow viscoelastic time constant, the maximum DOR for each pair of parameters exceeded 35 when selecting for LECs and against differentiated LECs, indicating that the combined classifiers have the potential to classify cells more efficiently than the individual parameters (Figs. 4.10H–4.10J & Table 4.3). The combined classifiers were less successful in selecting for LECs and

against central cornea cells (Figs. 4.9E–4.9G & Table 4.3).

Table 4.3: Diagnostic Odds Ratios for Two-Parameter Combinations. For each pair of parameters, the maximum and mean diagnostic odds ratios (DORs) were calculated for classifying limbal epithelial cells (LECs) versus differentiated LECs or central cornea cells. The DOR of a perfect classifier is infinite for any threshold value, whereas the DOR of a random classifier is approximately 1, and a test classifier will have a finite DOR>1. τ_2, slow viscoelastic time constant.

	Maximum DOR		Mean DOR	
	LEC vs. Differentiated LEC	LEC vs. Central Cornea	LEC vs. Differentiated LEC	LEC vs. Central Cornea
Diameter + Young's Modulus	65.00	42.78	11.89	1.33
τ_2 + Diameter	73.75	3.55	12.23	0.39
Young's Modulus + τ_2	37.55	47.35	8.67	2.74

Although the DOR provides a measure of the utility of a binary classifier, the calculation assumes that false positives (i.e. differentiated cells that are identified as stem-like cells) and false negatives (i.e. stem-like cells that are identified as differentiated cells) are equally problematic. Thus, the ideal scheme to enrich stem-like limbal cells for regenerative medicine does not necessarily maximize the DOR. The presence of stem-like cells in a population may accelerate tissue regeneration (reviewed in [9]), promoting the idea that false negatives may be less desirable than false positives. Contrarily, the low prevalence (1-10%) of stem-like cells in the limbus [115,126] confounds the challenges of removing a large percentage of false positive cells. Therefore, further biological study of the limbal niche will be required to determine the relative importance of minimizing false positives versus false negatives for applications to corneal regeneration using limbal stem cell therapy [115]. Upon determining the ideal balance between false positives and negatives, the results presented in the present study can be used as framework to inform mechanically-driven enrichment of stem-like cells from a heterogeneous corneal cell population.

4.6 Conclusion

We identify cell stiffness as a novel stemness indicator for cells derived from the corneal limbus. Characterization of the mechanical properties of cells derived from the corneal limbus showed that the stem-like LECs were softer than both cells from the central cornea and in vitro-differentiated LECs. Additional biophysical properties, such as size and the slow viscoelastic time constant, can also be utilized to distinguish the stem-like LECs from a mixed cell population. Biophysical markers hold great promise for improving corneal transplant success for LSCD patients. Measuring cellular mechanical properties by atomic force microscopy is low throughput (approximately 3 min/cell), but microfluidics holds great promise for a high-throughput method that combines stiffness-, size-, and viscoelasticity-based sorting to isolate stem-like cells [73,104,140,155–157]. Such high-throughput techniques can be used to generate corneal tissue implants with highly enriched stem-like limbal cell populations, which may yield superior clinical outcomes compared to tissue implants that are directly harvested from the cornea [115].

CHAPTER V

BIOPHYSICAL SUBSETS OF EMBRYONIC STEM CELLS DISPLAY DISTINCT PHENOTYPIC AND MORPHOLOGICAL SIGNATURES

5.1 Introduction

The typical tissue-engineered organ or regenerative medicine therapy requires 10-100 million cells of one or more prescribed cell types [57], which is difficult to achieve using autologous cell sources. Embryonic stem cells (ESCs) hold great potential as scalable, phenotype-specific cell factories, but progress is hampered by the challenge of reliably and efficiently controlling both potency (i.e. the degree of progress toward a terminally differentiated cell; see Fig. 5.1A, illustrated as cell transparency) and lineage specification (i.e. the remaining set of potential differentiated phenotypes; see Fig. 5.1A, illustrated as cell hue).

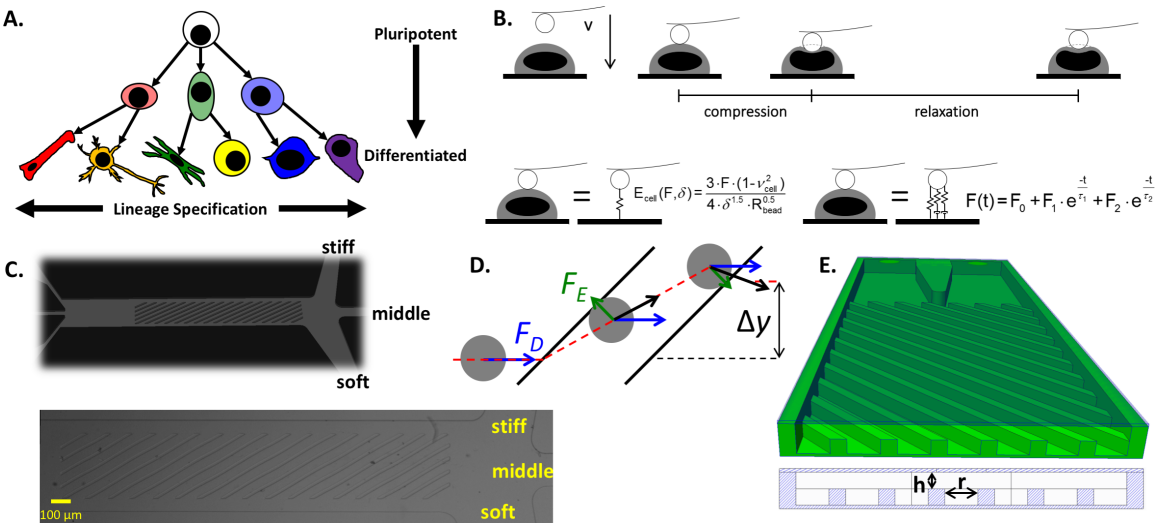

Figure 5.1: Biophysical Characterization and Sorting. **A.** Potency, as illustrated by transparency, is highest for an embryonic stem cell (transparent) and decreases during specification to a terminally differentiated cell (opaque). Lineage specification, as illustrated by hue, changes based on the set of phenotypes to which a given cell can differentiate. **B.** Cell mechanical parameters were assessed by atomic force microscopy using a beaded cantilever. The cantilever was driven toward the cell until a 5 nN trigger was registered, completing the compression region of the force curve; subsequently, the relaxation of the cell was measured over 10 s. The compression region was fit to the Hertzian model to calculate the cellular Young's modulus, E_{cell}. A two Maxwell element viscoelastic model was fit to the relaxation portion of the force curve, yielding two viscoelastic time constants, τ_1 and τ_2. **C.** To sort cells based on biophysical parameters, a microfluidic device with diagonal ridges was employed. **D.** As a cell approaches each diagonal ridge, the ridge compresses the cell, creating an elastic force (F_E). The cell is also exposed to a ridge-generated secondary flow that imposes a hydrodynamic drag force (F_D). The net force, and therefore the trajectory of each cell, is stiffness-dependent. **E.** The critical geometrical parameters were the gap size, h, and the ridge spacing, r. The gap size determines the strain imposed on a cell of a given size. The time a cell takes to travel between ridges (the inter-ridge time), which can be controlled by the overall flow rate or the inter-ridge spacing, affects the dependence of cell trajectory on viscoelastic relaxation.

ESC cultures are remarkably heterogeneous and typically contain not only colonies of pluripotent ESCs, but also outgrowths of their fibroblast-like differentiated progeny [133]. Even within putatively pluripotent ESC colonies, the expression of pluripotency markers is heterogeneous [134]. However, controlling both potency and lineage specification in ESC-derived cell populations is paramount for tissue engineering and

regenerative medicine. Excessive potency can cause dangerous teratomas, whereas deficient potency is associated with low proliferative potential, which can limit the efficacy of a cell therapy. Additionally, lineage specification must be controlled to obtain starting cell populations with sufficient phenotypic purity, which are required to generate functional tissue-engineered organs and efficient cell therapies.

Even with extensive efforts to engineer the cellular microenvironment, directed differentiation protocols are generally low yield (less than 50% target phenotype) or time-consuming (typically greater than 3 weeks). A low yield hampers the ability to use the cell population for applications such as tissue engineering, which requires high purity to create an organ of interest that closely matches *in vivo* physiology. A complementary method of phenotype control is to select target cell types from a heterogeneous population, which requires an understanding of the cell subsets that exist for each selection basis (e.g. gene or protein expression).

Biomolecular subsets of stem cells have been well studied [11] (reviewed in [47]). However, cell identification based on biomolecular expression is limited by the inconsistent and poorly understood expression of protein and gene markers for specific phenotypes. Biomarker expression can be transient, and the absence or presence of multiple markers is typically required to define a phenotype.

To address this problem, we and others [18, 19, 34, 112] have proposed cellular mechanical parameters as additional factors to help identify phenotype. At present, biophysical subsets of stem cells and their relationships with potency and lineage specification are not well studied.

Therefore, the objective of this study was to understand the biological characteristics of distinct biophysical subsets of ESCs. The results indicate that pluripotent cells are softer than differentiating cells and that the soft biophysical subset of partially differentiated cells displays a similar signature to pluripotent cells, with regard to cell mechanics, morphology, and gene expression trends. The present work serves as a

step toward high-throughput enrichment of specified ESC-derived cell phenotypes for tissue engineering and regenerative medicine.

The results of this study highlight cell mechanics as a future basis for efficient, high-throughput isolation of pluripotent ESCs, which will facilitate biological understanding of pluripotency and serve as a step toward realizing the potential of ESCs as cell sources for various applications.

5.2 Methods

5.2.1 Cell Culture

Murine ESCs (D3 cell line, ATCC, Manassas, VA) were cultured in growth media (15% fetal bovine serum [Atlanta Biologicals, Atlanta, GA], 2 mM L-glutamine [ThermoFisher, Waltham, MA], 1x MEM non-essential amino acid solution [Mediatech, Herndon, VA], 0.1 mM 2-mercaptoethanol [ThermoFisher], and 100 U/mL penicillin, 100 μg/mL streptomycin, and 0.25 μg/mL amphotericin [PSA; Mediatech] in Dulbecco's modified Eagle's medium [Sigma-Aldrich, St. Louis, MO]) on polystyrene Petri dishes treated with 0.1% gelatin (Millipore, Billerica, MA). Media was changed every other day, and cells were passaged at approximately 70% confluence. To encourage pluripotency, growth media was supplemented with 1.1 x 10^3 U/mL leukemia inhibitory factor (LIF; Millipore). Upon achieving pluripotent colonies, as identified by rounded morphology, differentiation was induced by culturing the mESCs in LIF- growth media. Alternatively, media containing bone morphogenetic protein 4 (BMP-4) was used to direct differentiation to the mesoderm lineage, as previously described [80]. Briefly, embryoid bodies were formed by centrifugation into Aggrewells™ (Stem Cell Technologies, Vancouver, BC, Canada), maintained on a rotary orbital shaker platform at 65 rpm, and differentiated in mesoderm induction media (10 ng/mL BMP-4 [R&D Systems, Minneapolis, MN], 2 mM L-glutamine [ThermoFisher], and PSA in ESGRO complete basal media [Millipore]).

5.2.2 Preparation of Cell Suspensions

For microfluidics experiments that employed cell staining to identify the day of differentiation, pluripotent LIF+ mESCs were stained with 500 nM CellTracker™ Green CMFDA (ThermoFisher) and differentiating LIF- cells were stained with 5 μM CellTracker™ Red CMTPX dye (ThermoFisher), using the manufacturer's protocol. For the remaining microfluidics experiments and all biophysical characterization experiments, cell dyes were not used. Prior to biophysical characterization or microfluidic sorting, cells were detached from the gelatin-coated dishes using a solution of 0.05% trypsin and 0.53 mM ethylenediaminetetraacetic acid (EDTA; Sigma-Aldrich), pelleted by centrifugation, and dissociated by trituration.

5.2.3 Biophysical Characterization

Approximately 100,000 cells were plated on poly-L-lysine-coated glass dishes and immobilized during 16-24 h incubation at 37°C. Immediately prior to probing, non-adherent cells were removed by wash the dish 2x with PBS (with magnesium and calcium). To simplify the tip-cell contact geometry, 5.5 μm polystyrene beads were attached to tipless silica nitride cantilevers (Bruker Probes, Camarillo, CA) using two-part epoxy, and dried overnight. Mechanical properties of individual cells were obtained from force-indentation curves recorded with an atomic force microscope (Asylum Research, Santa Barbara, CA) with an integrated optical microscope (Nikon, Melville, NY) on a vibration isolation table. Atomic force microscopy is summarized in Fig. 5.1B. The Sader calibration method [123] was used to obtain cantilever spring constants (k=6-14 pN/nm) based on the thermal vibration of the cantilever. The cantilever probe was visually aligned with the cell center and translated to indent the cell with a velocity of 2 μm/s until a force trigger of 5 nN was reached. To examine the cell relaxation under compression, the cantilever dwelled at the surface of the compressed cell for 10 s while the cellular relaxation response was recorded.

To calculate the cellular Young's modulus, the Hertzian contact model was fit to the compression segment of the force-indentation curve over the applied force range of 2.5-4.75 nN, where the Young's modulus was largely independent of the indentation. The cells were taken to be incompressible (cellular Poisson's ratio = 0.5). The Young's modulus of each cell was calculated as the average of 3 independent measurements.

To calculate the viscoelastic properties of the cells, the spring-damper model was fit to the relaxation segment of the force-time curve, using the MaxwellWiechert model to calculate the viscoelastic time constants [127]. Two Maxwell elements were chosen to best fit the data. The fast and slow viscoelastic time constants were designated as 1 and 2, respectively. The viscoelastic properties of each cell were calculated as the averages of 3 independent measurements.

To calculate the spread area and aspect ratio of each cell based on the phase contrast images captured during atomic force microscopy (see Fig. 5.10G), ImageJ was employed to manually draw a polygon around each cell. The spread area was calculated as the area within the polygon, and the aspect ratio was calculated as major axis divided by the minor axis of the fit ellipse.

5.2.4 Morphology Characterization

Suspended cell size histograms were obtained using a Multisizer Coulter Counter, which was calibrated using microspheres of known sizes.

5.2.5 Collection of Biophysical Subsets

Microfluidic sorting devices with 2 or 3 outlets were fabricated, as previously described [155–157]. A reusable SU-8 mold (Microchem Corp.) containing the device features was formed using standard two-step photolithography on a silicon wafer. A mixture of polydimethylsiloxane pre-polymer and curing agent (PDMS; 10:1 v:v; Sylgard 184, Dow Corning) was used for replica molding with curing at 60°C for 6 h. After curing, the 1 mm inlet holes and 3 mm outlets holes were punched, enabling each outlet to

serve as a reservoir for cell collection. PDMS was treated with air plasma using a plasma cleaner (Harrick) and bonded to a glass slide to form the microfluidic chip. After plasma bonding, the channel was incubated at 60°C for 1 h to further strengthen the bond.

The sorting buffer consisted of 87.5 nL/mL Tween-20, 40 μg/mL EDTA, and 1 mg/mL bovine serum albumin (BSA) in a 3:7 (v:v) mixture of Percoll (GE Life Sciences, Pittsburgh, PA) and phosphate buffered saline (PBS, without magnesium and calcium). Prior to sorting, the buffer was pH adjusted to 7.4 and filtered with a 0.22 μm pore filter. To keep the cell concentration constant during sorting, the ratio of Percoll to PBS was tuned such that the buffer density matched the cell density. The ratio optimized using density centrifugation with various Percoll:PBS ratios. Maintaining the buffer at 4°C and including BSA, EDTA, and Tween-20 facilitated a single-cell suspension. The inlet flow rates were controlled using syringe pumps (Harvard Apparatus).

For the cell system described in this study, the gap size, which controls the strain experienced by each cell (see Figs. 5.1C–5.1E), and the overall flow rate, which controls the inter-ridge relaxation time for each cell, were optimized to maximize separation.

To optimize the total flow rate, videos were recorded using a high-speed camera (Vision Research, Wayne, NJ) during individual sorts of unstained cells after either 0 or 5 days of differentiation. For various total flow rates, cells reaching each outlet were counted manually. In all cases considered, the fraction of cells reaching the stiff outlet was negligible.

Cells were manually collected from the outlet reservoirs and periodically transferred to uncoated polystyrene Petri dishes containing growth media. Prior to characterization, cells were transferred to a tube and pelleted.

5.2.6 Biophysical Subset Characterization

One day after sorting, the mechanics and morphology of single cells taken from each biophysical subset were probed by atomic force microscopy and phase contrast microscopy, as described above.

Primers were obtained from Invitrogen, as listed in Table 5.1, and resuspended in DNA suspension buffer (Teknova, Hollister, CA).

Table 5.1: Primer Sequences. Primers employed for pre-amplification and PCR.

Gene	Forward Sequence (5' to 3')	Reverse Sequence (5' to 3')
mACTN1	TTAACACGCTGCAGACCAAG	TCTCTAGCCTCCGGATCTCA
mGAPDH	CATGGCCTTCCGTGTTCCTA	CCTGCTTCACCACCTTCTTGAT
mISL1	ATGATGGTGGTTTACAGGC	TCGATGCTACTTCACTGCC
mLMNA	TGAGTACAACCTGCGCTCAC	TGACTAGGTTGTCCCCGAAG
mMAP2	AGTGGCACCTCCACACCTAC	CGGATGATGGCAACTTTCTT
mNANOG	GAAATCCCTTCCCTCGCCATC	CTCAGTAGCAGACCCTTGTAAGC
mPOU5F1	CCGTGTGAGGTGGAGTCTGGAG	GCGATGTGAGTGATCTGCTGTAGG
mS18	CTCTAGTGATCCCTGAGAAGTTCC	ACTCGCTCCACCTCATCCTC
mSOX2	CTCGCAGACCTACATGAACG	AGTGGGAGGAAGAGGTAACC

Primer pairs were designed using Primer3 and validated for RT-qPCR through amplification of cDNA prepared with the CellsDirect™ One-Step qRT-PCR kit (ThermoFisher) and run on a StepOne Plus with SYBR Green detection chemistry (ThermoFisher). Amplification traces were baseline corrected and amplification efficiencies were measured using LinRegPCR software [121, 122, 149]. Melt curves were used

for preliminary screening of primer pairs for primer dimers and multi-product reactions, and all primer products were validated for length and specificity using gel electrophoresis on a 1% agarose gel run in 1.5x TAE buffer.

To prepare samples for gene expression measurements, 100 cells from each sample replicate were dispensed into CellsDirect™ 2x reaction mix (ThermoFisher) containing 1 U/μL SUPERase In™ RNase inhibitor (ThermoFisher) to prevent degradation using a FACSAria Fusion™ cell sorter (BD Biosciences, San Jose, CA).

The lysed cells were mixed with the pooled set of primers (normalized to 500 nM), SuperScript® III RT Platinum® Taq Mix, and nuclease-free water. A thermocycler was used to convert RNA to cDNA, with reverse transcription occurring at 50°C for 15 min, followed by reverse transcriptase inactivation and Taq activation at 95°C for 2 min. To amplify the cDNA using the pooled primers, the sample was exposed to 20 cycles of 15 s at 95°C and 4 min at 60°C. The cDNA samples were stored at 4°C.

cDNA samples were then processed with exonulcease I to remove any unincorporated primer and diluted 5-fold. 3 μL of each sample and primer mix was prepared for the Fluidigm FLEXsixIFC chip. Finally, a Fluidigm Biomark was used to thermal cycle the chip 30 times and read the amplification via EvaGreen® fluorescence.

C_t values and threshold fluorescence signals were obtained using the Fluidigm Real-Time PCR Analysis software package with automatic detector thresholds. Initial target DNA concentrations were calculated as previously described [78], using $N_0 = \frac{t}{\epsilon^{C_\mathrm{t}}}$, where t is the threshold fluorescence signal for each target, C_t is the threshold cycle for each sample, and ϵ is the reaction efficiency, assessed as the mean efficiency calculated using LinRegPCR software. Gene expression fold-changes were calculated using the $\Delta\Delta C_\mathrm{t}$ method, with the housekeeping gene as the geometric mean of mGAPDH and mS18, as previously described [151], and the control sample as day 0 for differentiation time point samples or as the soft outlet for samples collected after biophysical sorting. To simplify analysis, the 100-cell samples collected

from 4 different separation experiments (3 experiments, n=1; 1 experiment, n=3) were combined as a single set with n=6, as between-experiment and between-replicate gene expression variabilities were similar (Fig. 5.2).

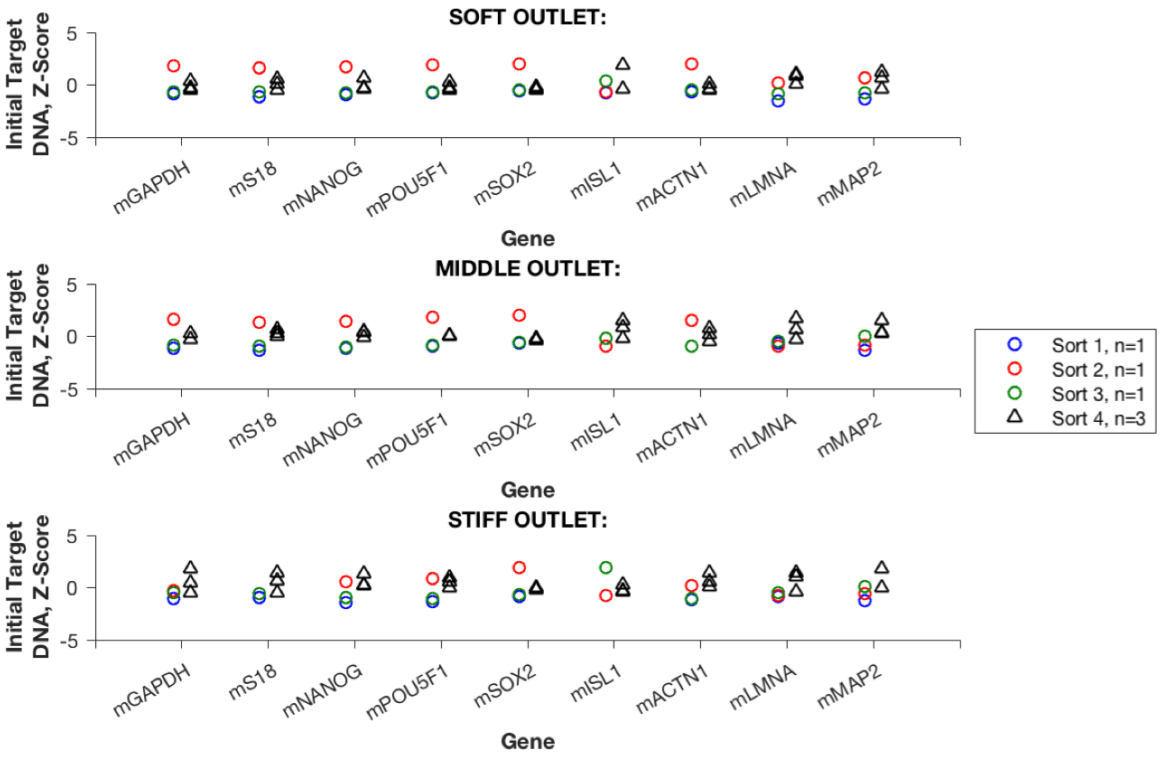

Figure 5.2: Combination of Biophysical Subset Gene Expression Replicates. Following biophysical separation, 100-cell samples were collected for gene expression analysis. For the first 3 separation experiments (blue, red, and green circles), n=1 100-cell replicate was collected per outlet. For the fourth separation experiment (black triangles), n=3 100-cell replicates were collected. As the range and distribution of initial target DNA z-scores was not substantially different between separation experiments vs. between replicates, further analyses were conducted using the pooled set of n=6 100-cell samples.

Initially, the expression levels of m18S, mPAX6, and mMYF5 were also measured. However, the extremely high abundance of m18S caused exponential amplification by cycle 2, resulting in highly variable threshold cycle readings. The low abundance of mMYF5 and mPAX6 precluded PCR amplification in most samples. Therefore, m18S, mPAX6, and mMYF5 were removed from the analysis.

5.2.7 Statistics and Figure Generation

In total, paired stiffness-morphology data were obtained for 359 cells. Data were grouped by differentiation method and day of differentiation; 80 of the cells were undifferentiated (day 0), 162 were differentiated by LIF removal in monolayer (day 1, n=29; day 2, n=30; day 3, n=30; day 4, n=29; day 5, n=28; day 6, n=16), 59 were differentiated by LIF removal in embryoid body format (day 6, n=29; day 10, n=30), and 58 were differentiated by BMP-4 treatment in embryoid body format (day 6, n=29; day 10, n=29). Paired stiffness-viscosity-morphology data were available for 192 of the cells measured, of which 30 were undifferentiated (day 0) and 162 were differentiated by LIF removal in monolayer (day 1, n=29; day 2, n=30; day 3, n=30; day 4, n=29; day 5, n=28; day 6, n=16).

Bootstrapping ANOVA was performed using a custom code in MATLAB (MathWorks, Natick, MA) to discern statistically significant differences and apply Holm's p-value adjustment (α=0.1), as previously reported [19]. Spearman's rank correlations were assessed by first using JMP statistical software (SAS Institute, Cary, NC) to obtain coefficients and raw p values and subsequently using a custom Microsoft Excel spreadsheet to apply Holm's p-value adjustment (α=0.1) and plot the resulting color matrices (e.g., Fig. 5.4C). For differentiation studies, pluripotent cells were coded as 0 and differentiating cells were coded as 1. For biophysical subset studies, the soft subset was coded as -1, the middle subset was coded as 0, and the stiff subset was coded as 1. When comparing the day of differentiation and the differentiation state, the Pearson's correlation coefficient is +1.0, as expected; however, the Spearman's rank correlation coefficient is lower due to the method JMP invokes to break ties.

Beeswarm plots (e.g., Fig. 5.4A), semitransparent scatter plots (e.g., Fig. 5.13A), and semitransparent radar plots (Fig. 5.11B) were generated using custom MATLAB codes.

5.3 Results

5.3.1 Biophysical Characterization of Embryonic Stem Cells during Differentiation

Before addressing the biological properties of ESC biophysical subsets, the characteristics of ESCs with a known day of differentiation were first considered. Analysis of cell stiffness for the full set of paired stiffness-morphology data (N=359) revealed that pluripotent ESCs were softer than differentiated ESCs, with minimal effects of the cantilever spring constant, day 0 passage number, and differentiation method (Fig. 5.3). As the differentiation method was not an important factor to cell mechanics, all subsequent analyses and experiments were confined to the LIF removal differentiation method (N=242).

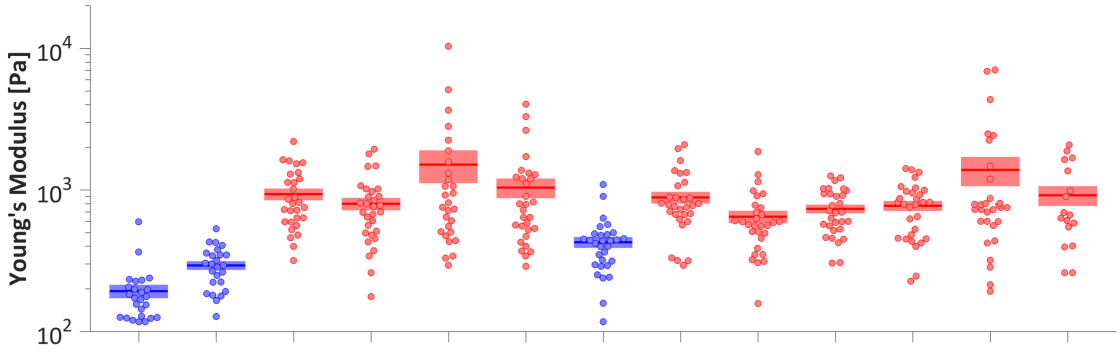

Sample	A	B	C	D	E	F	G	H	I	J	K	L	M
Day 0 Session	1	2	3	3	3	3	4	4	4	4	4	4	4
Day 0 Passage	27	18	44	44	44	44	28	28	28	28	28	28	28
Day of Diff.	0	0	6	6	10	10	0	1	2	3	4	5	6
Diff. Method	LIF-, FBS+	LIF-, FBS+	BMP4+, ESGRO	LIF-, FBS+	BMP4+, ESGRO	LIF-, FBS+	LIF-, FBS+	LIF-, FBS+	LIF-, FBS+	LIF-, FBS+	LIF-, FBS+	LIF-, FBS+	LIF-, FBS+

Figure 5.3: The Young's Modulus Depended More on Differentiation State than Other Factors. Among the 13 samples probed during 4 atomic force microscopy sessions, effects of the day 0 passage number and the differentiation method were dominated by the effect of the differentiation state, i.e. pluripotent (blue) vs. differentiating (red). LIF, leukemia inhibitory factor; FBS, fetal bovine serum; BMP4, bone morphogenetic protein 4; ESGRO, Millipore ESGRO complete basal medium.

Analysis of cell stiffness revealed that ESCs became stiffer during differentiation, with a substantial stiffness increase after only one day of differentiation (Figs. 5.4A–5.4C).

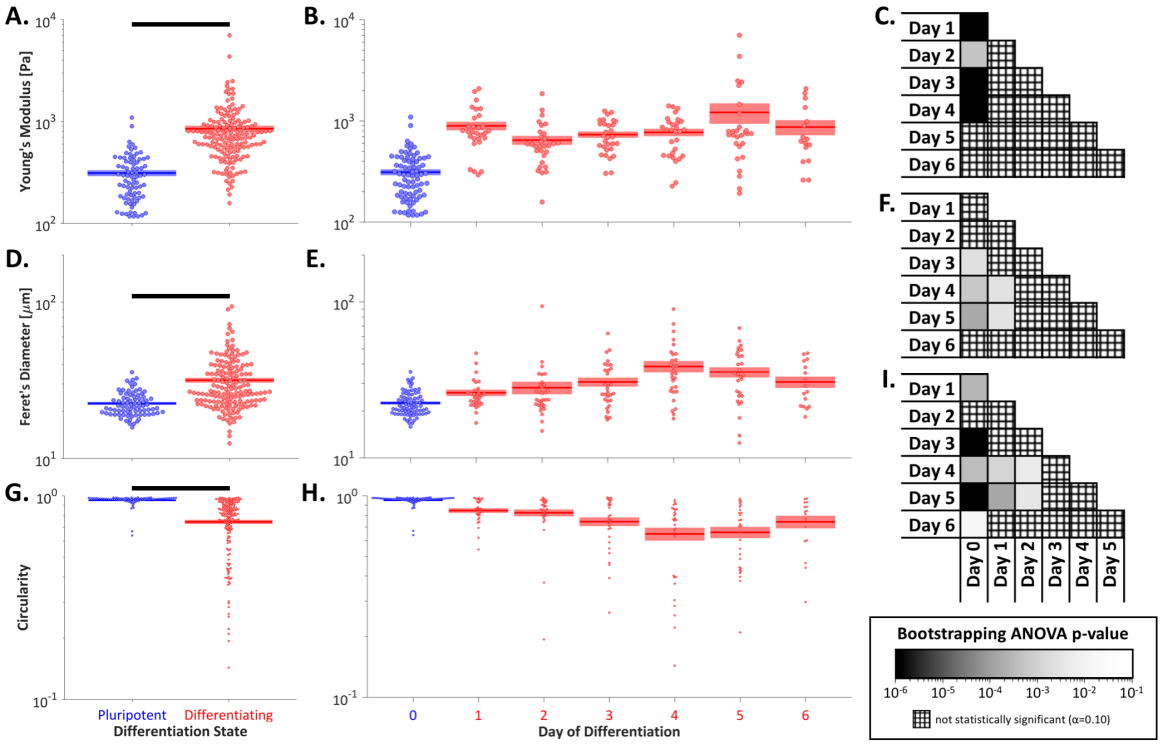

Figure 5.4: Embryonic Stem Cells become Stiffer, Larger, and Less Circular during Differentiation. A. Pluripotent ESCs were significantly softer than the pool of all differentiating cells ($p < 10^{-6}$). **B.** Cellular Young's modulus increased after 1 day of differentiation, and no substantial subsequent change was observed through 6 days of differentiation, indicating the potential utility of Young's modulus as a specific marker of ESC differentiation. **C.** Pluripotent cells were significantly softer than days 1-4 of differentiation. **D.** Pluripotent ESCs had a significantly smaller Feret's diameter than the pool of all differentiating cells ($p < 10^{-6}$). **E.** Cell size, as assessed by Feret's diameter, increased and then decreased over the course of 6 days of differentiation. **F.** Pluripotent cells were significantly smaller than cells after days 3-5 of differentiation, and day 1 cells were significantly softer than day 4-5 cells. **G.** Pluripotent ESCs were significantly more circular than the pool of all differentiating cells ($p < 10^{-6}$). **H.** Cell shape, as assessed by circularity, decreased and then increased over the course of 6 days of differentiation. **I.** Pluripotent cells were significantly more circular than cells after days 3-6 of differentiation, and day 1 and 2 cells were significantly more circular than day 4-5 cells. Populations connected by black bars are significantly different (α=0.1). Blue, pluripotent cells; red, differentiating cells; black, $p \leq 10^{-6}$; white, $p \geq 10^{-1}$; cross-hatch, non-significant p-value.

The quantification of phase contrast images taken during atomic force microscopy yielded various morphological parameters, which were divided into size- and shape-related factors. The Feret's diameter, which represents the longest distance between

any two points on the cell border, correlated more strongly with the day of differentiation than any other size factor (see Fig. 5.11C). The circularity, which is defined as $\frac{4 \cdot \pi \cdot \text{area}}{\text{perimeter}^2}$ and ranges from 0 for an elongated polygon to 1 for a perfect circle, correlated more strongly with the day of differentiation than any other shape factor (see Fig. 5.11C). Analysis of the morphological factors revealed that ESCs became larger (i.e. increased Feret's diameter) and less circular during differentiation (Figs. 5.4D, 5.4G). Interestingly, the Feret's diameter increased and then decreased during differentiation, whereas the circularity decreased and then increased during differentiation. The extrema of the mean Feret's diameter and circularity both occurred at day 4 (Figs. 5.4E, 5.4F, 5.4H, 5.4I). The inverse relationship between Feret's diameter and circularity may reflect the tendency for ESCs to become fibroblatic (i.e. spread, high aspect ratio) during differentiation.

Analysis of the smaller set of paired stiffness-viscosity-morphology data (N=192) revealed that the fast and slow viscoelastic time constants were both lower for pluripotent than differentiated cells; however, significant differences in the time constants between individual days of differentiation were not generally observed (Fig. 5.5). The paired stiffness-viscosity-morphology data with sample letters matched to the samples in Fig. 5.3 were re-plotted in Figs. 5.6, 5.7.

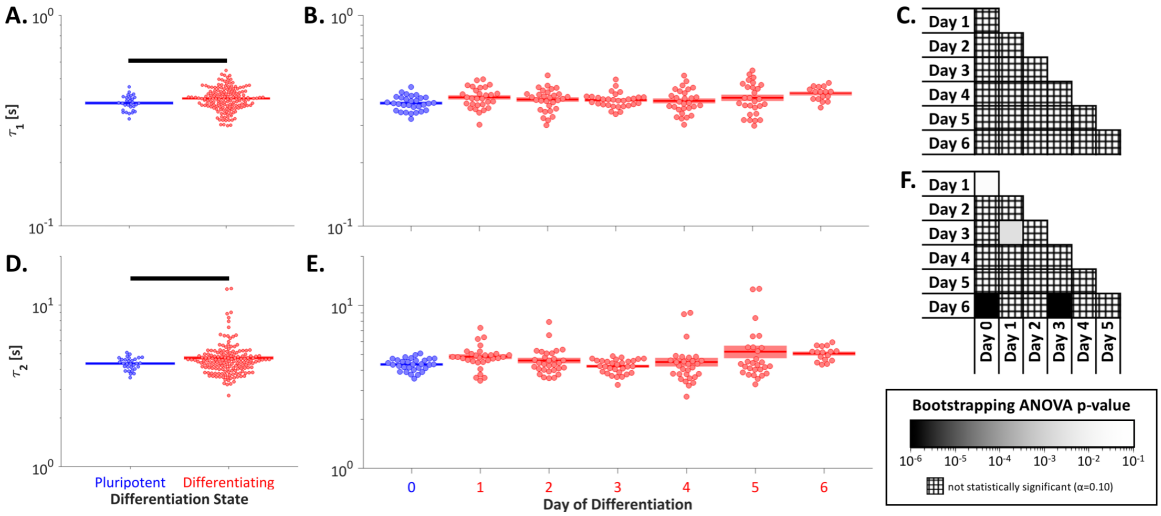

Figure 5.5: Changes to Embryonic Stem Cell Viscoelastic Relaxation during Differentiation were Minimal. **A.** Pluripotent ESCs had a significantly smaller fast viscoelastic time constant (τ_1) than the pool of all differentiating cells ($p = 0.005$). **B.** Changes to the fast viscoelastic time constant were not observed during 6 days of differentiation. **C.** The fast viscoelastic time constant was not significantly different between any two days of differentiation ($p_{\text{ANOVA}} = 0.10$). **D.** Pluripotent ESCs had a significantly smaller slow viscoelastic time constant (τ_2) than the pool of all differentiating cells ($p = 0.007$). **E.** The slow viscoelastic time constant changed only subtly during 6 days of differentiation. **F.** Pluripotent ESCs had a significantly smaller slow viscoelastic time constant than day 1 and 6 cells. Significant differences also existed between day 1 and 3 cells and between day 3 and 6 cells. Populations connected by black bars are significantly different (α=0.1). Blue, pluripotent cells; red, differentiating cells; black, $p \leq 10^{-6}$; white, $p \geq 10^{-1}$; cross-hatch, non-significant p-value.

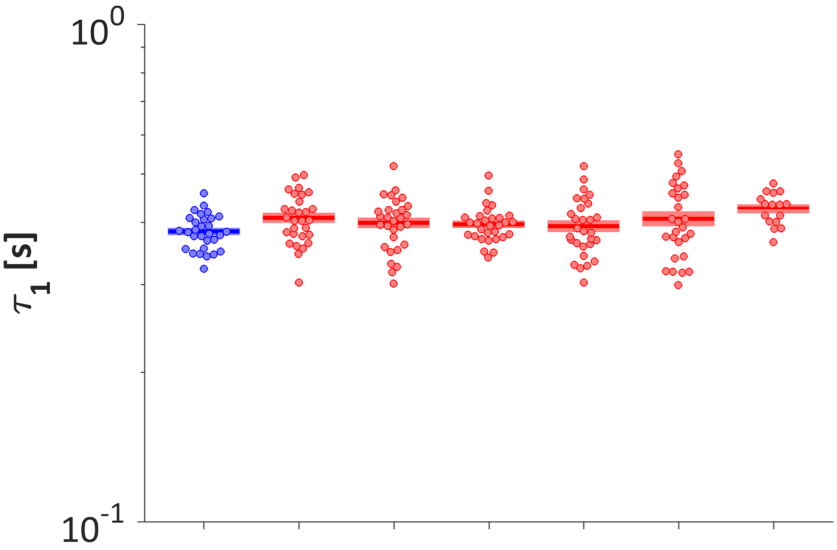

Sample	G	H	I	J	K	L	M
Day 0 Session	4	4	4	4	4	4	4
Day 0 Passage	28	28	28	28	28	28	28
Day of Diff.	0	1	2	3	4	5	6
Diff. Method	LIF-, FBS+	LIF-, FBS+	LIF-, FBS+	LIF-, FBS+	LIF-, FBS+	LIF-, FBS+	LIF-, FBS+

Figure 5.6: The Fast Viscoelastic Time Constant, τ_1, did not Depend on the Day of Differentiation. Sample letters are matched to the samples in Fig. 5.3. LIF, leukemia inhibitory factor; FBS, fetal bovine serum.

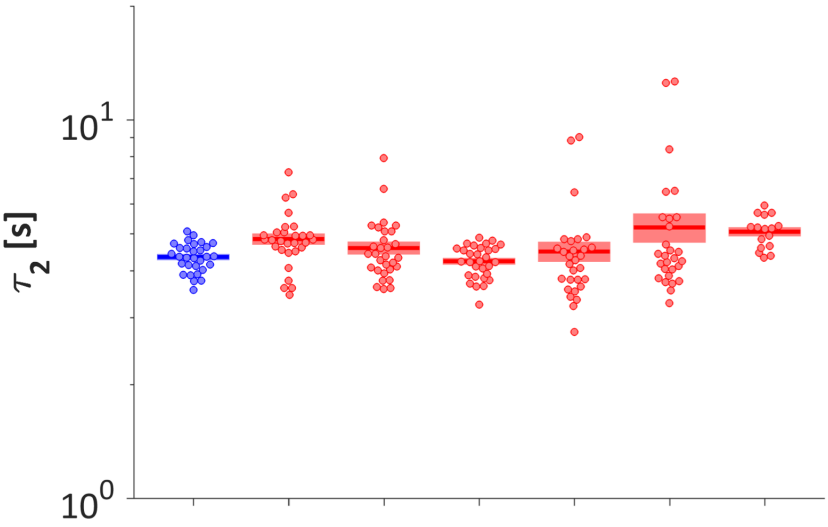

Sample	G	H	I	J	K	L	M
Day 0 Session	4	4	4	4	4	4	4
Day 0 Passage	28	28	28	28	28	28	28
Day of Diff.	0	1	2	3	4	5	6
Diff. Method	LIF-, FBS+	LIF-, FBS+	LIF-, FBS+	LIF-, FBS+	LIF-, FBS+	LIF-, FBS+	LIF-, FBS+

Figure 5.7: The Slow Viscoelastic Time Constant, τ_2, did not Depend on the Day of Differentiation. Sample letters are matched to the samples in Fig. 5.3. LIF, leukemia inhibitory factor; FBS, fetal bovine serum.

5.3.2 Sorting Pluripotent from Differentiating Embryonic Stem Cells

A 2-outlet device with a 15.6 μm gap was employed to sort pluripotent (day 0, LIF+) from differentiating cells (5 days LIF-). Cell cultures chosen for rounded pluripotent colonies or spread differentiating colonies (Fig. 5.8A) were stained with CellTracker™ Green and Red, respectively, to identify day of differentiation post-sort. The cell inlet flow rate was 8 μL/min, and the soft and stiff sheath inlet flow rates were 23 μL/min and 17 μL/min, respectively, resulting in a slight bias to the soft outlet.

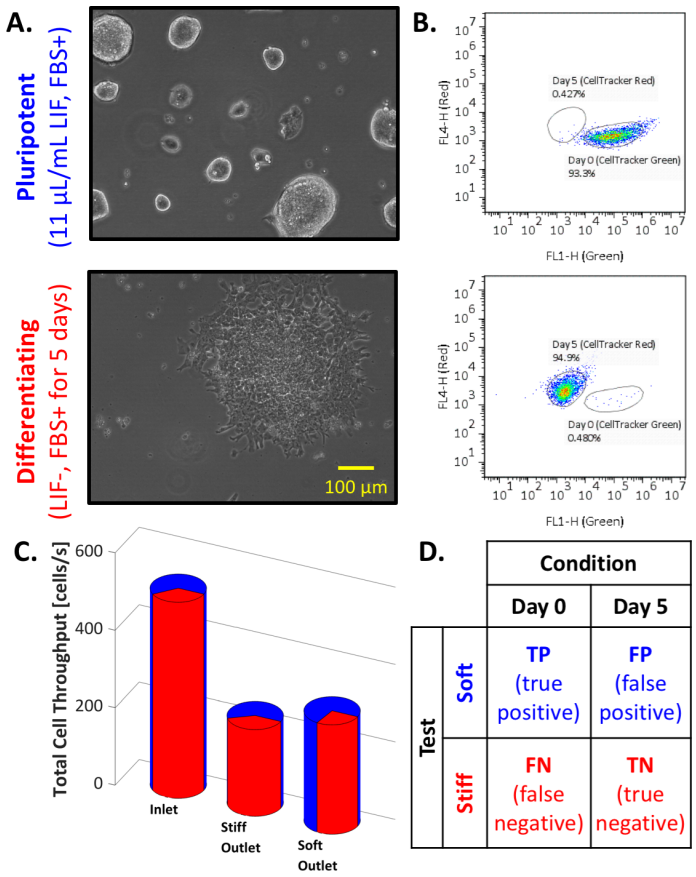

Figure 5.8: Biophysical Separation of Day 0 from Day 5 Embryonic Stem Cells. A. Before sorting, the LIF+ cell culture displayed pluripotent colonies with rounded morphology and the LIF- cell culture was characterized by differentiated, fibroblastic morphology. **B.** The pluripotent cells, stained green, and the differentiating cells, stained red, displayed distinct fluorescent signatures. **C.** Starting with a mixture of approximately 65% day 0 cells (blue) and 35% day 5 cells (red), 40% of cells sorted to the stiff outlet were day 5 and 75% of cells sorted to the soft outlet were day 0, indicating enrichment in both outlets. Blue, pluripotent cells; red, differentiating cells. **D.** To define the sorting efficiency, the contingency table was employed to divide cells by condition (condition positive, day 0; condition negative, day 5) and test (test positive, soft outlet; test negative; stiff outlet). The overall efficiency, defined as the diagnostic odds ratio, was 1.9.

The contingency table, which was used to assess sorting efficiency, separates sorted cells into true positives (TPs), false positives (FPs), false negatives (FNs), and true negatives (TNs) (Fig. 5.8D; for further information, see [18]). Biophysical sorting was used to select for pluripotent ESCs (condition positive) and against differentiated ESCs (condition negative). Cells sorted to the soft outlet were considered as test

positive, and cells sorted to the stiff outlet were considered as test negative.

The efficiency of sorting the day 0 cells, $e_{\text{day 0}}$, was described by the positive likelihood ratio, $LR+$, such that

$$e_{\text{day 0}} = LR+ = \frac{\text{true positive rate}}{\text{false positive rate}} = \frac{\frac{TP}{TP+FN}}{\frac{FP}{FP+TN}} = \frac{\frac{TP}{FP}}{\frac{TP+FN}{FP+TN}} = \frac{\left(\frac{\%\text{ day 0}}{\%\text{ day 5}}\right)_{\text{soft outlet}}}{\left(\frac{\%\text{ day 0}}{\%\text{ day 5}}\right)_{\text{inlet}}}.$$

Similarly, the efficiency of sorting the day 5 cells, $e_{\text{day 5}}$, was described by the multiplicative inverse of the negative likelihood ratio, $LR-$, such that

$$e_{\text{day 5}} = \frac{1}{LR-} = \frac{\text{true negative rate}}{\text{false negative rate}} = \frac{\frac{TN}{FP+TN}}{\frac{FN}{TP+FN}} = \frac{\frac{TN}{FN}}{\frac{FP+TN}{TP+FN}} = \frac{\left(\frac{\%\text{ day 5}}{\%\text{ day 0}}\right)_{\text{stiff outlet}}}{\left(\frac{\%\text{ day 5}}{\%\text{ day 0}}\right)_{\text{inlet}}}.$$

Thus, the efficiencies of sorting day 0 and 5 cells were 1.6 and 1.2, respectively. The overall sorting efficiency, e_{total}, was described by the diagnostic odds ratio, DOR, such that

$$e_{\text{total}} = DOR = \frac{LR+}{LR-} = \frac{\frac{TP}{FP}}{\frac{FN}{TN}} = e_{\text{day 0}} \cdot e_{\text{day 5}}.$$

The overall sorting efficiency was 1.9, which is analogous to enriching a mixture from 50% to 62% day 0 cells during a single pass through the device.

5.3.3 Biophysical Subsets

Before characterizing the biological properties of partially differentiated ESCs, the microfluidic device parameters were first optimized. A 3-outlet device containing an additional middle outlet was employed to increase the sorting resolution relative to the 2-outlet device used to sort day 0 from day 5 cells.

The gap height, which affects the strain to which each cell is exposed, was optimized to tune the differential trajectories of pluripotent and differentiated cells. The suspended cell size was similar for pluripotent and differentiating cells (Fig. 5.9A). The 15.6 μm employed for sorting day 0 from day 5 cells resulted in minimal cell

strain, but the 9.3 μm gap caused device clogging; therefore, the 11.5 μm gap was considered to be optimal (Figs. 5.9B–5.9D).

Although the changes to viscoelasticity during differentiation were minimal, the device parameters were also tuned to optimize viscoelastic-dependent cell separation. As the time a cell takes to pass from one ridge to the next depends on both the inter-ridge distance and the overall flow rate, the inter-ridge distance was fixed, and the overall flow rate, which is easier to adjust, was optimized. The lowest flow rates investigated (2.5 μL/min) maximized the percentage of pluripotent cells reaching the soft outlet and the percentage of differentiating cells reaching the middle outlet (Figs. 5.9E, 5.9F). Lower flow rates increase the dominance of elastic- over viscous-driven cell separation; thus, the low flow rates maximized the separation of the relatively soft pluripotent cells from the relatively stiff differentiating cells, and reduced separation based on the viscoelastic time constants, which were similar for pluripotent and differentiating cells. To increase the throughout achieved with a 2.5 μL/min flow rate, a total flow rate of 5 μL/min was chosen. Cell sorting was not biased, so both sheath inlet flow rates were set to 2 μL/min and the cell inlet flow rate was set to 1 μL/min.

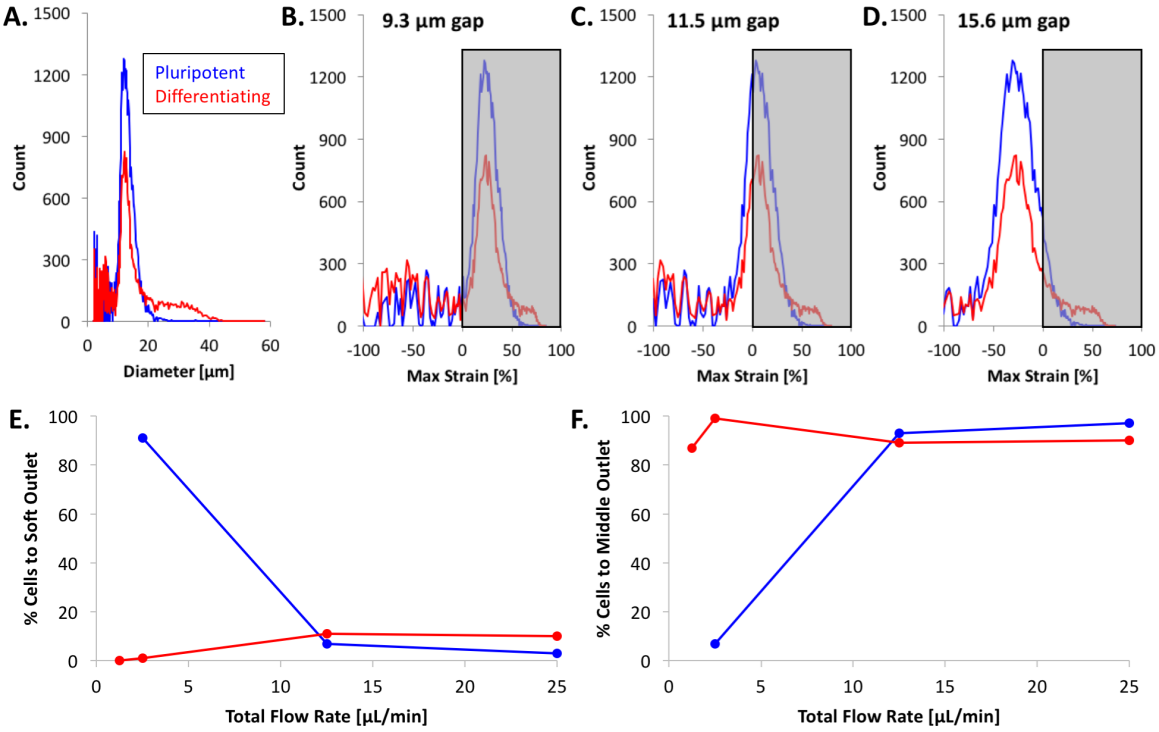

Figure 5.9: Microfluidic Design Optimization. A. The size distribution was similar for pluripotent (blue) and differentiating (red) cells, with modal cell sizes near 12 μm. **B–D.** The design of the microfluidic device requires cells to experience strain for sorting to occur. As the gap size was increased from 9.3 to 15.6 μm, the fraction of cells experiencing strain (gray shading) decreased. However, as the 9.3 μm gap caused device clogging, the 11.5 μm gap was optimal. **E–F.** Optimization studies indicated that a low total flow rate would increase both the fractions of pluripotent cells reaching the soft outlet and the fraction of differentiated cells reaching the middle outlet. The fraction of cells reaching the stiff outlet was negligible.

Biophysical subsets were generated from a cell culture that lacked LIF for 5 days, but contained both pluripotent and differentiating colonies (Fig. 5.10A). Characterization revealed that cells in the soft subset had significantly lower Feret's diameters (Fig. 5.10B) and higher circularities than cells sorted to the middle and stiff outlets (Fig. 5.10C), supporting the conclusion that the soft outlet was enriched for pluripotent cells, which displayed similar morphological signatures. Furthermore, cells sorted to the soft outlet were indeed softer than cells sorted to the stiff outlet (Fig. 5.10D). The fast viscoelastic time constant was not different between the biophysical subsets

(Fig. 5.10E), as observed during ESC differentiation. Differences in the slow viscoelastic time constant did not indicate increased pluripotency in the soft biophysical subset (Fig. 5.10F); however, the increased slow time constant in the soft biophysical subset may reflect the mechanism of cell sorting, which causes both soft and more viscous cells to be sorted to the soft outlet.

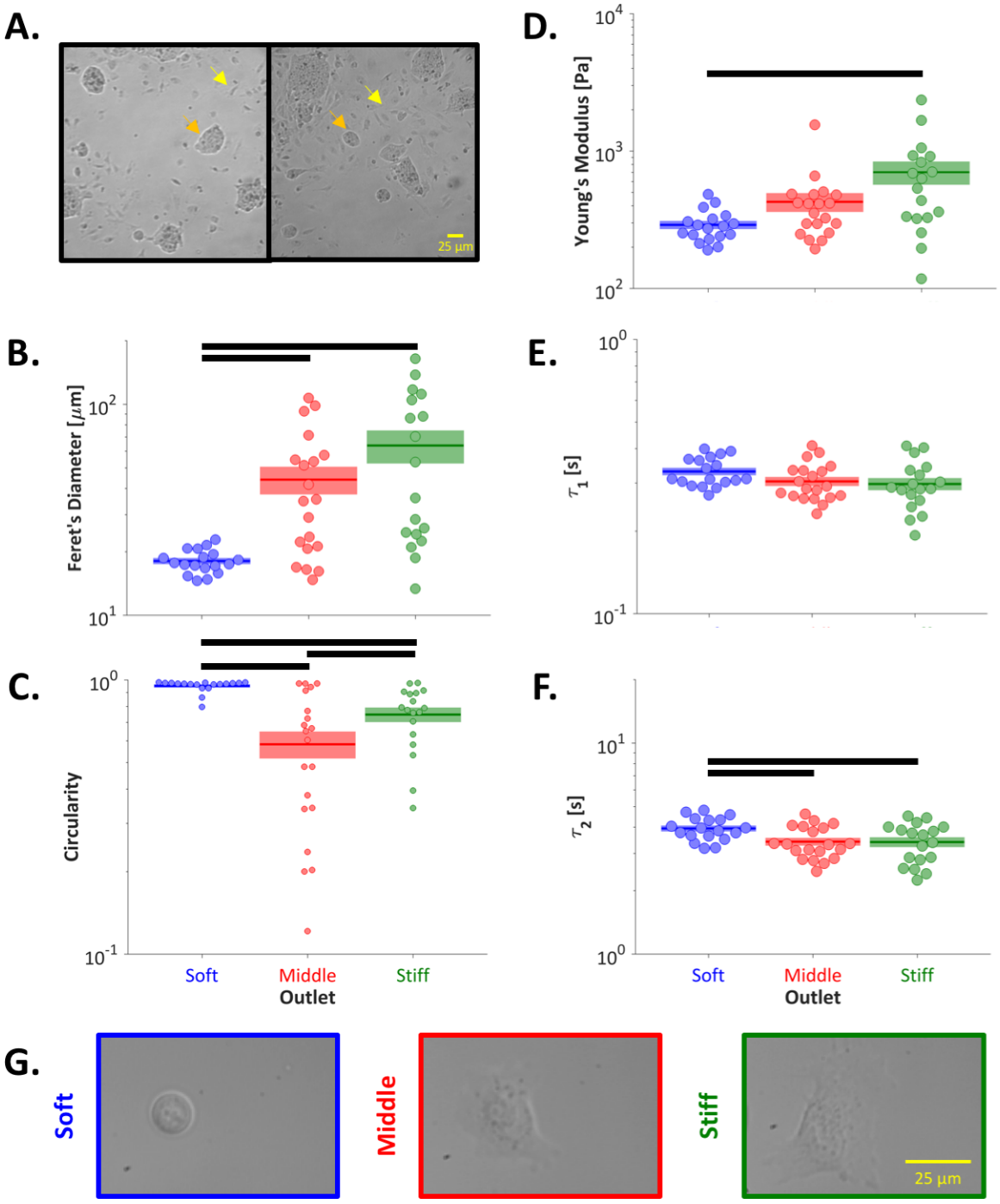

Figure 5.10: Biophysical Characterization After Microfluidic Stiffness-Based Sorting. A. Before sorting, the cell cultures were characterized by a mixture of rounded, pluripotent colonies (e.g. orange arrows) and mesenchymal morphology, differentiated cells (e.g. yellow arrows). **B.** Cells sorted to the soft outlet had a significantly smaller Feret's diameter than cells sorted to the middle ($p_{\text{adjusted}} = 0.012$) or stiff outlets ($p_{\text{adjusted}} = 0.012$). **C.** Cells sorted to the soft outlet were significantly more circular than cells sorted to the middle ($p_{\text{adjusted}} < 10^{-6}$) or stiff outlets ($p_{\text{adjusted}} = 0.003$). Cells sorted to the stiff outlet were significantly more circular than cells sorted to the middle outlet ($p_{\text{adjusted}} = 0.042$). **D.** Cells sorted to the stiff outlet were significantly stiffer than cells sorted to the soft outlet ($p_{\text{adjusted}} = 0.010$). **E.** The sorted cells did not have a significantly different fast viscoelastic time constant ($p_{\text{ANOVA}} = 0.127$). **F.** Cells sorted to the soft outlet had a significantly higher slow viscoelastic time constant than cells sorted to the middle ($p_{\text{adjusted}} = 0.019$) or stiff outlets ($p_{\text{adjusted}} = 0.030$). Populations connected by black bars are significantly different (α=0.1). **G.** Representative images of individual cells taken during atomic force microscopy corroborate the quantified Feret's diameters and circularities.

5.3.4 Gene Expression of Embryonic Stem Cells by Day of Differentiation and Biophysical Subset

ESCs were differentiated for 3 days before being sorted into biophysical subsets for assessment of gene expression. The expression of housekeeping genes (mGAPDH, mS18), pluripotency genes (mNANOG, mPOU5F1, mSOX2), differentiation genes (mISL1, mMAP2), and structural genes (mACTN1, mLMNA, mMAP2) was investigated both over the course of differentiation and for the soft, middle, and stiff biophysical subsets. mNANOG, mPOU5F1 (Oct-4), and mSOX2 are common markers of ESC pluripotency, and mISL1 (Islet-1) expression indicates endoderm differentiation. mMAP2 (microtubule-associated protein 2) expression is associated with both ectoderm differentiation and microtubule assembly [168]. mACTN1 (α-actinin-1) crosslinks F-actin filaments and increase the stiffness of the actin filament network [19]. Expression of mLMNA (Lamin A/C) is associated with stiff nuclei [85].

During differentiation, significant changes to the expression of any gene measured were not observed (Fig. 5.11A), as quantified by Spearman's correlations (Table 5.2).

However, all three pluripotency genes generally decreased during differentiation, concomitantly with a general increase in the endoderm differentiation gene mISL1 and the ectoderm differentiation gene mMAP2, as expected.

The soft biophysical subset was characterized by decreased expression of the endoderm differentiation marker mISL1, although the pluripotency genes mPOU5F1 and mSOX2 did not change substantially and mNANOG was actually decreased (Fig. 5.11B). Furthermore, the increased expression, on average, of mACTN1, mLMNA, and mMAP2 in the stiff outlet suggests that the cells may be stiffer due to increased presence of actin filaments, nuclear structure proteins, and microtubules. However, differential gene expression among the 3 biophysical subsets was not observed for any gene measured, as quantified by Spearman's correlations (Table 5.2).

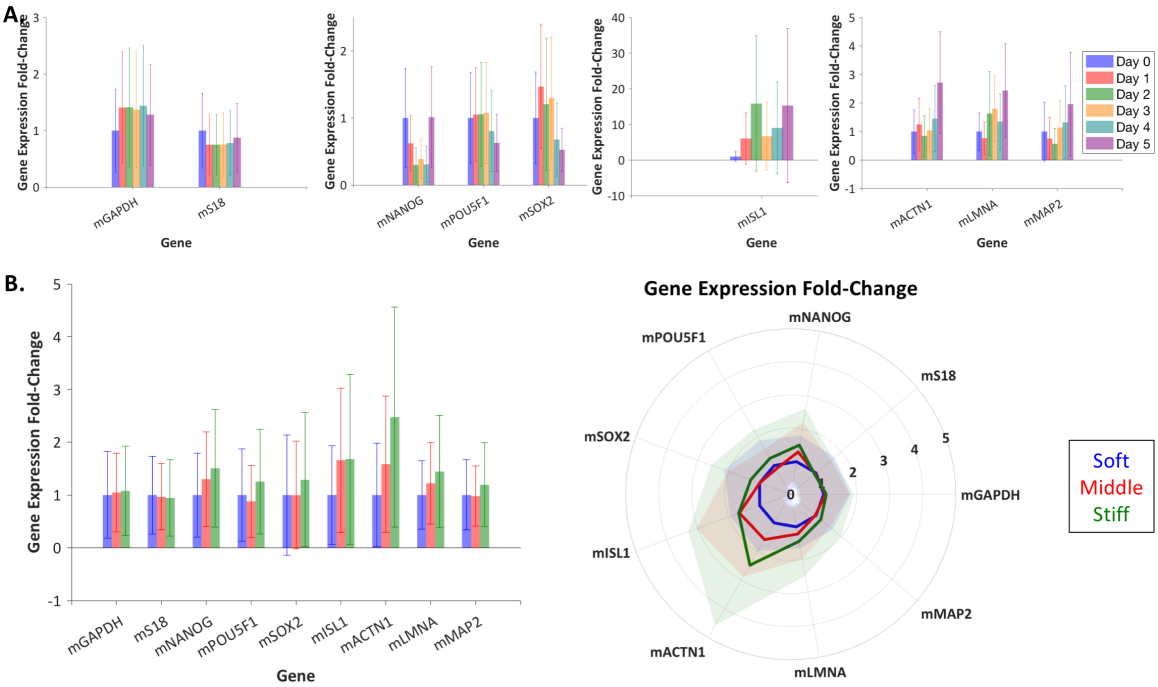

Figure 5.11: Gene Expression by Day of Differentiation and Outlet. A. The housekeeping genes mGAPDH and mS18 were consistent during differentiation. The pluripotency genes mNANOG, mPOU5F1, and mSOX2 generally decreased during differentiation and the differentiation gene mISL1 generally increased during differentiation, as expected, but the trends were not significant. Clear trends in the structural genes mACTN1, mLMNA, and mMAP2 were not observed. Blue, day 0; red, day 1; green, day 2; orange, day 3; teal, day 4; violet, day 5; $\Delta\Delta C_t$ values, control group = day 0. **B.** The pluripotency genes mPOU5F1 and mSOX2 were increased in the soft outlet, although mNANOG showed the opposite trend. The differentiation gene mISL1 and the structural genes mACTN1, mLMNA, and mMAP2 were all generally increased in the middle and stiff outlets. Blue, soft outlet; red, middle outlet; green, stiff outlet; error bars (bar plots) or shaded regions (radar plot), mean ± standard error; $\Delta\Delta C_t$ values, control group = soft outlet. Gene expression fold-change values of mMAP2 increased significantly with differentiation, but did not change significantly by day of differentiation or outlet for any gene measured, as assessed by Spearman's correlations (Table 5.2).

Table 5.2: Gene Expression did not Change By Outlet or Day of Differentiation, as Assessed by Spearman's Rank Correlation Coefficients. A significant increase in mMAP2 was observed over the course of differentiation. For the other 8 genes measured, the Spearman's coefficients' p values exceeded $\alpha = 0.05$.

Gene	Spearman's ρ, by outlet	p, by outlet	Spearman's ρ, by day	p, by day
mGAPDH	-0.091634	0.726508	0.179382	0.506211
mS18	0.091634	0.726508	-0.179382	0.506211
mNANOG	0.297478	0.246213	-0.325877	0.218045
mPOU5F1	-0.407704	0.104278	-0.376702	0.150377
mSOX2	-0.172643	0.507580	-0.254125	0.342234
mISL1	0.106242	0.684865	-0.130052	0.631187
mACTN1	0.347942	0.171140	-0.040361	0.882021
mLMNA	0.318726	0.212442	0.438242	0.117023
mMAP2	0.069057	0.792276	0.556084	0.025298

5.4 Discussion

To further assess the relationship between differentiation and biophysical subset, Spearman's correlation coefficients were calculated for each pair of parameters, taking into account either cells with a known day of differentiation ("unsorted mESCs," Fig. 5.11C) or cells sorted into biophysical subsets ("sorted mESCs," Fig. 5.11D). The correlation coefficients indicated that both pluripotent cells and cells sorted to the soft outlet were small, soft, and round (see also Fig. 5.13), supporting the conclusion that the microfluidic device successfully enriched for pluripotent cells in the soft outlet.

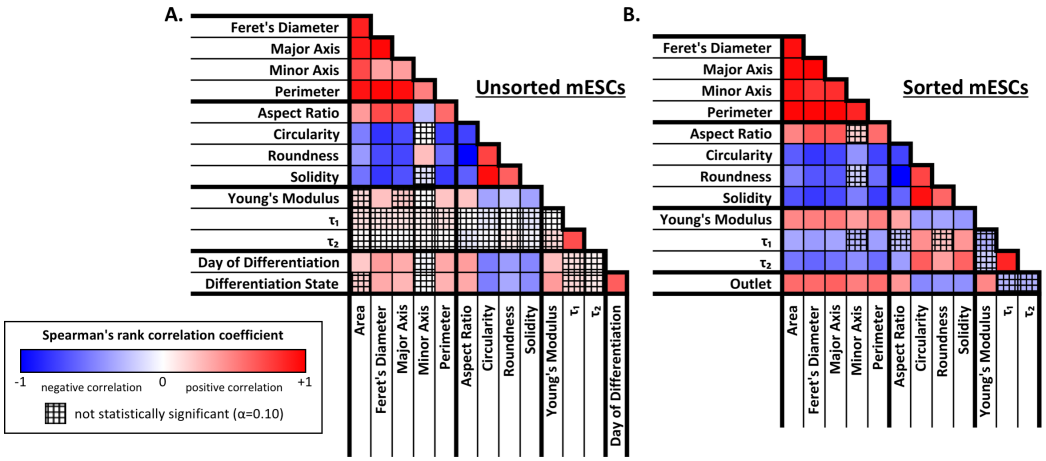

Figure 5.12: Biophysical Correlation Color Maps for Unsorted and Sorted mESCs. A. Spearman's correlations, which indicate monotonic trends, of pairs of biophysical parameters were compared for unsorted mESCs with known day of differentiation and differentiation state (0, pluripotent; 1, differentiating). Differentiation was positively correlated with cell size (high area, Feret's diameter, major axis, minor axis, perimeter) and stiffness (high Young's modulus), but negatively correlated with roundness (low aspect ratio; high circularity, roundness, solidity). **B.** Spearman's correlations were also calculated following microfluidic sorting, i.e. based on outlet (-1, soft outlet; 0, middle outlet; 1, stiff outlet). The stiff outlet tended to have cells that were larger (high area, Feret's diameter, major axis, minor axis, perimeter), more elongated (high aspect ratio; log circularity, roundness, solidity), and stiffer (high Young's modulus). Overall, the correlations between pairs of biophysical parameters were similar for unsorted mESCs relative to the day of differentiation or differentiation state (A) and for sorted mESCs relative to the microfluidic outlet (B). Blue, negative Spearman's correlation coefficient (indirect relationship); red, positive Spearman's correlation coefficient (direct relationship); white, zero Spearman's correlation coefficient (no correlation); cross-hatch, non-significant p-value.

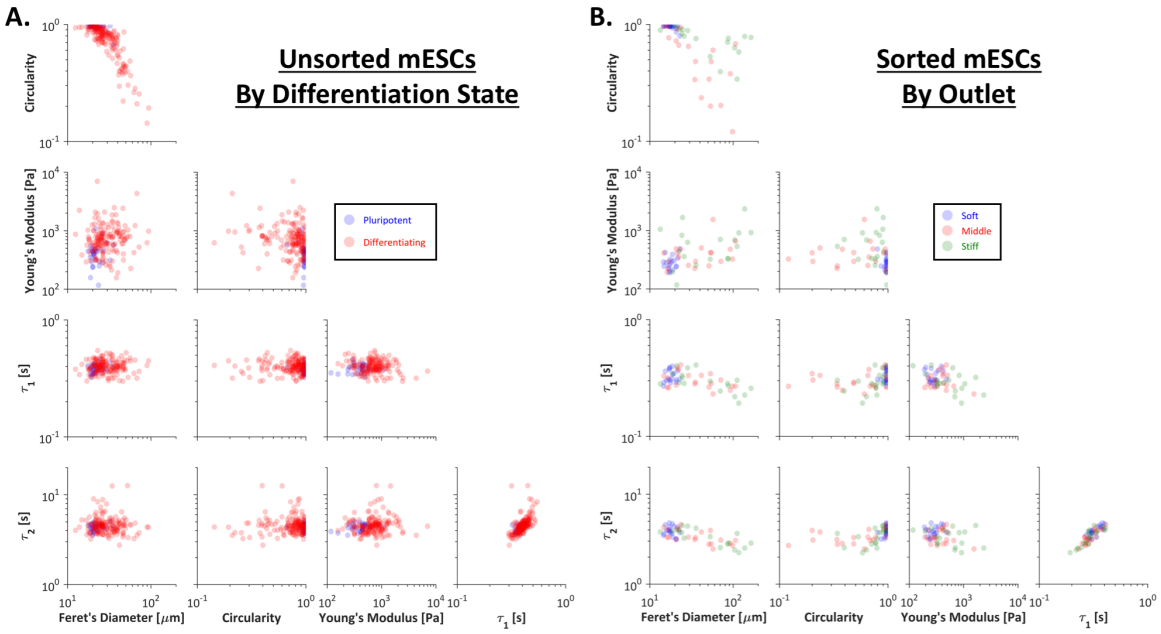

Figure 5.13: Similarities between Pairwise Biophysical Signatures of Pluripotent Cells and Cells Sorted to the Soft Outlet. A. Compared to the differentiating cells (red), the pluripotent cells (blue) were small, circular, and soft. **B.** The biophysical characteristics were similar for cells sorted to the soft outlet (blue) and pluripotent cells, whereas cells sorted to the middle (red) and stiff outlets (green) resembled differentiating cells.

Importantly, the trends observed for the unsorted mESCs held regardless of data set expansion to include cells lacking viscoelastic relaxation data (Fig. 5.14), indicating that the trends observed were not artifacts of the particular data subset chosen for analysis.

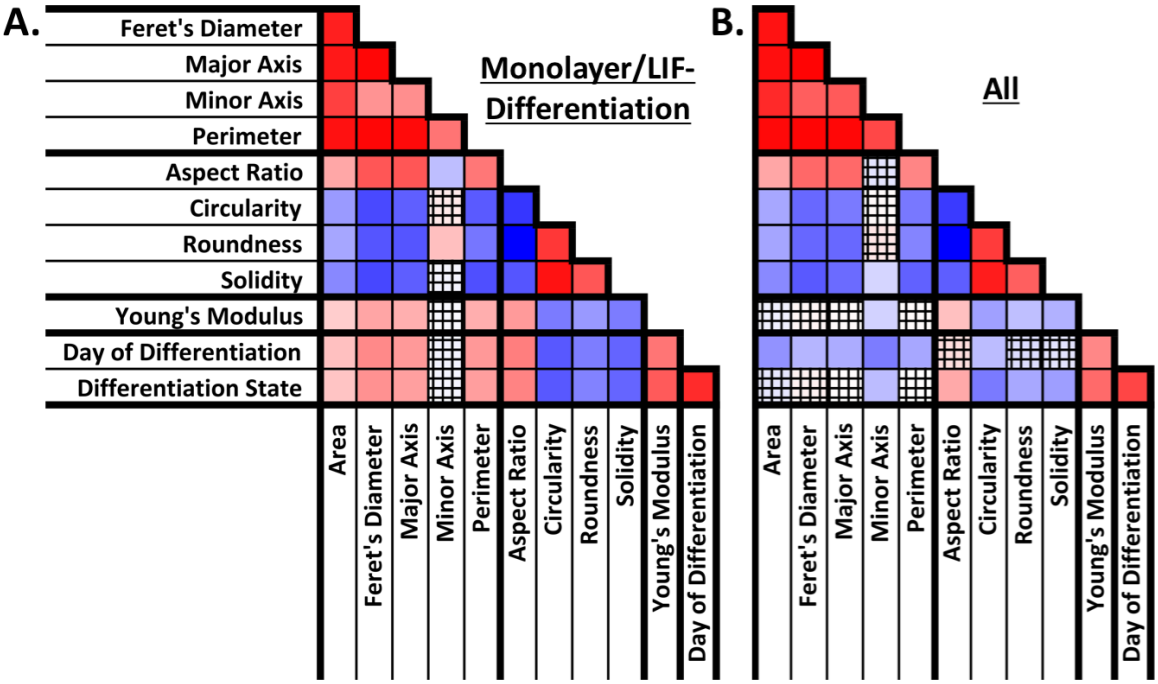

Figure 5.14: Trends Between Pairs of Biophysical Parameters did not Change Substantially for Expanded Data Sets. A–B. Compared to Fig. 5.11C, similar relationships among size, shape, mechanics, and differentiation were observed when the data set was expanded to include cells for which viscoelastic data were not available. The first data expansion included only cells differentiated in monolayer by LIF removal (A, N=242), and the second data expansion considered all cells, including cells differentiated in embryoid body format (B, N=359). As viscoelastic relaxation profiles were not recorded for large portions (21% and 47%, respectively) of cells in the expanded data sets, relationships with the viscoelastic relaxation time constants were not considered.

Strikingly, Young's modulus was the only parameter that correlated more strongly with differentiation state (i.e. pluripotent vs. differentiating) than the day of differentiation for both stiffness and stiffness-viscoelastic data, indicating that Young's modulus may serve as a better binary potency classifier than the other parameters measured. Interestingly, the observed change in stiffness may have structural underpinnings related to the cytoskeleton and nucleus. Pluripotent stem cells are known to have a less developed cytoskeleton than more differentiated cells [20]. Furthermore, pluripotent ESCs have reduced levels of lamin A/C, resulting in an open chromatin state and irregular nuclear shape [43]. Reduced levels of lamin A/C have also been

linked to decreased cell stiffness [85]. Previous reports have also suggested a role of chromatin condensation in ESC stiffening during differentiation [106, 112].

A previous study also sorted embryonic stem cells based on biophysical properties [158]. Tangential flow filtration was employed to separate embryonic stem cells from ESC-derived osteoblasts or fibroblasts based on Young's modulus. Interestingly, the Young's modulus increased, decreased, then increased again during osteoblast differentiation. Despite the lack of a monotonic trend, stiffness separation between ESCs and osteoblasts was achieved for all days of differentiation considered. The study highlights an establishment of stiffness-based sorting of embryonic stem cells and serves to highlight the ability to enrich for specific differentiated cell types using stiffness-based sorting, in addition to the ability to enrich for stem cells, as shown in the present study.

The microfluidic device presented herein, which can sort cells based on potency, has potential applications to rescuing an over-confluent ESC culture or removing the feeder layer from an ESC culture. To this end, mouse embryonic fibroblasts (MEFs) and pluripotent mESCs were sorted using a microfluidic device with a 15.6 μm gap, resulting in a 3.4-fold mESC enrichment and 3.3-fold MEF enrichment (Fig. 5.15). Thus, the overall sorting efficiency, e_{total}, was 11.2.

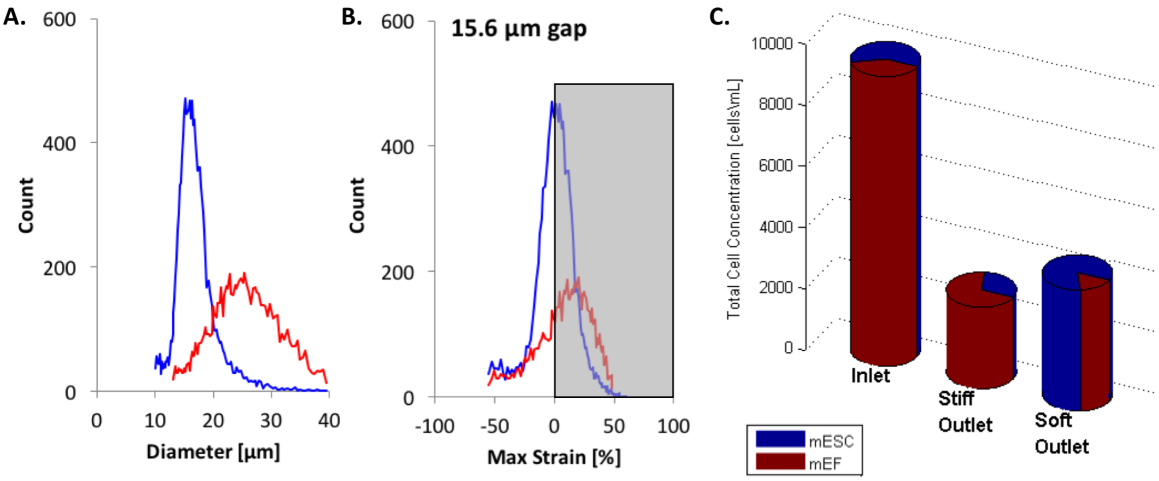

Figure 5.15: Biophysical Separation of Mouse Embryonic Stem Cells from Mouse Embryonic Fibroblasts. A. The modal diameter of mouse embryonic stem cells (mESCs, blue) was smaller than the modal diameter of the mouse embryonic fibroblasts (MEFs, red). **B.** A 15.6 μm device gap was chosen to expose the majority of mESCs and MEFs to strain (gray shading), maximizing the differential sorting trajectory between cell types. **C.** The sorting efficiencies of mESCs in the soft outlet and MEFs in the stiff outlet, defined similarly to $e_{\text{day }0}$ and $e_{\text{day }5}$, respectively, exceeded 3.

In the present study, pluripotent ESCs were enriched via mechanically-driven cell sorting, which highlights cell mechanics as a basis for efficient, high-throughput isolation of pluripotent ESCs. Further optimization of cell sorting parameters, such as flow rate, cell concentration, and device geometry, in addition to employing multiple sorts in series, will enable stiffness-based, microfluidic sorting to be used as a novel, label-free, and highly efficient method for the purification of pluripotent ESCs. The ability to generate pure populations of pluripotent ESCs will facilitate the understanding of pluripotency and serve as a step toward realizing the potential of ESCs as cell sources for various applications. Technologies that can select for or against pluripotent cells, such as stiffness-based microfluidic sorting, hold great potential to be adapted for the enrichment of specific differentiated lineages, with applications to improving directed differentiation for regenerative medicine and tissue engineering.

CHAPTER VI

SINGLE-CELL GENOMECHANICS ENABLES COMPARISONS OF THE MECHANICAL PROPERTIES AND GENE EXPRESSION OF INDIVIDUAL EMBRYONIC STEM CELLS

6.1 Introduction

Studies of the relationships between biomolecular and mechanical properties of cells have gained momentum in recent years, covering both in vitro cell systems and disease states, including stem cell differentiation [34,112,142], osteoarthritis [145], sickle cell disease [90], and cancer [32,162]. Cell mechanical parameters, such as stiffness and viscous relaxation, serve as individual indicators of the overall cell state; indeed, ties between biological state and cell structure, which can be measured via cell mechanics, have been identified in stem cell differentiation [19,80,142] and cancer metastasis [162]. Whereas mechanical parameters tend to be measured on the single-cell level, only a few studies have measured both biophysical and biomolecular properties at the subpopulation [87], clone [58], or individual cell level [19,95]. Subpopulation and clonal methods do not offer the same resolution as single-cell methods, and the existing single-cell methods rely on fluorescent techniques, where multiplexing is limited by spectral overlap. Other techniques, such as molecular beacons, are only semi-quantitative [37], which reduces the reliability of the information gleaned.

To truly understand the relationship between biological inputs and mechanical outputs, new techniques that measure multiple parameters on the single-cell level are needed. Unlike population-based techniques, single-cell analysis holds the potential

to understand the complex heterogeneity of stem cell populations with regard to cell mechanics, molecular expression, and phenotype.

Although mechanics tend to summarize cell state in one or several parameters, biological information is often highly multiplexed, resulting in data sets that can range from the fluorescent intensity of 10 antibodies to the expression of many thousands of genes. Thus, previous mechanics methods that relied on antibodies to deliver biological information were limited by fluorescence spectra overlaps and detection limits; an alternative method that could generate highly multiplexed biological data paired to mechanical information would be extremely powerful in both furthering the understanding cell mechanics and facilitating the use of mechanical parameters as label-free indicators of cell state. Multiplexed methods in the context of gene expression would enable investigations of the relationships among entire gene networks, cell mechanics, and cell phenotype.

Therefore, we developed a method to examine single-cell genomechanics to produce single-cell data that is paired for atomic force microscopy (AFM) mechanics measurements and polymerase chain reaction (PCR) gene expression readouts. In the present study, the expression levels of 5 genes were analyzed per cell; however, multiplex PCR methods can easily generate readings for 96 or more genes per cell. The main challenge in pairing AFM and PCR data was a conflicting sample preparation requirement. AFM requires the cell to be measured on a relatively flat surface, enabling the cantilever and associated electronics to probe the cell and come into close contact with the substrate, typically a glass slide or relatively large Petri dish (e.g. 50 mm). On the other hand, the liquid control requirements of single-cell PCR force an environment in which cells are isolated in individual liquid droplets, typically achieved using a small well plate (e.g. 96-well plate, 6 mm diameter wells). The complication is not only in satisfying two seemingly distinct sample preparation requirements, but also in transitioning from the live-cell AFM setup to the cell-lysing

PCR setup without losing the sample.

To address the AFM-PCR compatibility issue, cell carriers called genomechanics rafts were created. The rafts feature a flat, hard surface that is ideal for AFM. A hydrophilic island was created on an otherwise hydrophobic surface to localize liquid droplets and aid both cell attachment and pre-PCR lysate collection. The raft design also permitted macro-level manipulation with tweezers or magnets, simplifying the transition between stages of the method. To simplify scale-up, the system was designed to be compatible with standard 96-well spacing (8 rows and 12 columns spaced at 9 mm), which facilitated instrument setup and liquid processing via multichannel pipettors.

An overview of the single-cell genomechanics method is presented in Fig. 6.1A. Briefly, rafts were manufactured from stainless steel washers and polydimethylsiloxane (PDMS), a pourable polymer that hardens when cured. Oxygen plasma was used to make the PDMS hydrophilic, but the edge of each raft was protected by a silicone tape mask, and therefore retained the native hydrophobic nature of PDMS. One red-fluorescent cell was added to each raft using a cell sorter and immobilized on the surface. By focusing on green-fluorescent beads embedded in the rafts, an imaging plate reader was able to search each raft and identify successfully immobilized cells. Rafts were submerged in liquid for cell mechanics measurements via AFM and then immediately dried. Finally, each cell was lysed for gene expression measurements via PCR.

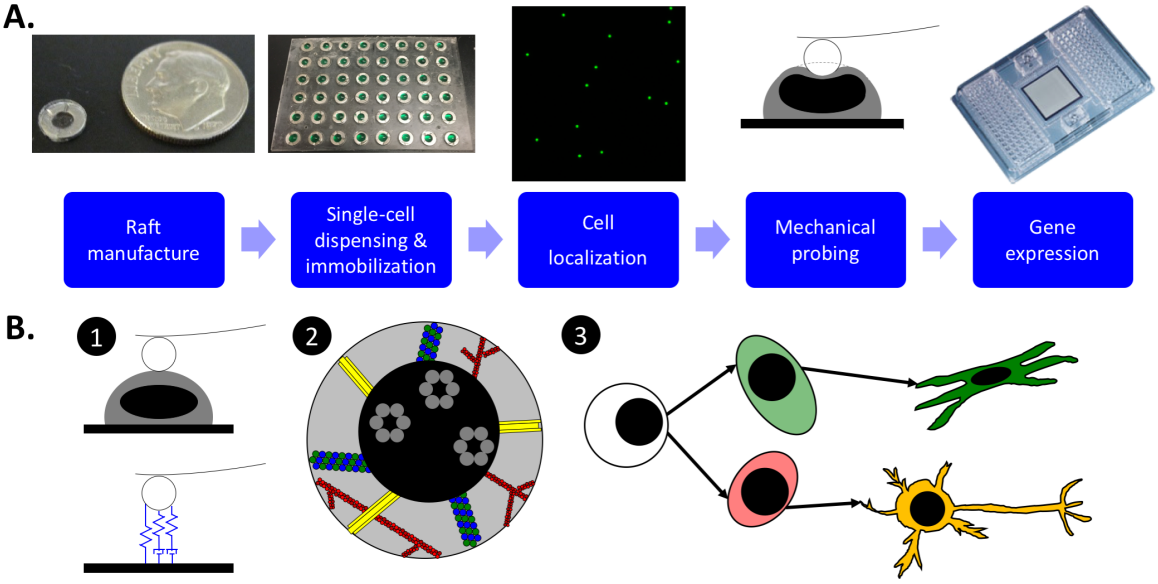

Figure 6.1: Single-cell Genomechanics Overview. A. To enable paired, single-cell measurements of mechanics and gene expression, rafts composed of PDMS and steel washers were constructed. One cell was dispensed onto each raft using fluorescence-activated cell sorting and immobilized. Cell locations were identified relative to fluorescent beads embedded in each raft. Each cell was probed mechanically by atomic force microscopy and lysed for gene expression analysis. **B.** The single-cell genomechanics method enables investigation of the interplay between 1) cell mechanical parameters, 2) molecular structural components, and 3) phenotypic differentiation.

The first single-cell genomechanics study was performed on embryonic stem cells (ESCs), which we and others have shown to stiffen during differentiation (Chapter 5, [106, 112]). For the first time, the tendency for stem cell stiffness to change during differentiation has been observed using not the day of differentiation, but rather gene expression, as the gold standard for differentiation state. Importantly within the context of stem cell biology, the single-cell technique is capable of detecting trends independently of asynchronous differentiation, which confounds studies that investigate populations of cells pooled by the day of differentiation. While neither day of differentiation nor gene expression is a perfect indicator of differentiation state, the new capacity to define differentiation based on dozens of gene expression measurements promises to enable improved definition of the differentiation state, and

thereby unambiguously clarify the relationship between cell mechanics and differentiation. Overall, the new method enables a direct understanding of the interplay between cell mechanics, cell structure, and phenotypic differentiation at the level of the individual cell (Fig. 6.1B). The single-cell genomechanics method can be applied to new biomedical systems by simply changing the cell type or target genes to understand the role of cell mechanics changes within various physiological and disease state models.

6.2 Methods

6.2.1 Raft Manufacture

The genomechanics rafts served as carriers to enable macro-scale manipulation of single cells. The rafts were composed of flat washers, PDMS, and fluorescent beads.

Washers were employed to prevent the liquid-submerged rafts from floating during atomic force microscopy. The washers were sufficiently rigid for manipulation using tweezers and sufficiently magnetic for manipulation using a neodymium magnetic wand. 18-8 stainless steel washers were chosen due to reduced cytotoxicity compared to standard zinc-coated washers [96]. M2.5 washers (inner diameter = 2.7 mm; outer diameter = 6.0 mm) were chosen to maximize the inner diameter (i.e. the target size for cell dispensing), while matching the outer diameter to the well diameter of a 96-well plate, enabling the use of standard mutichannel pipettors. Washers were stamped with Xs to identify orientation (Fig. 6.2A).

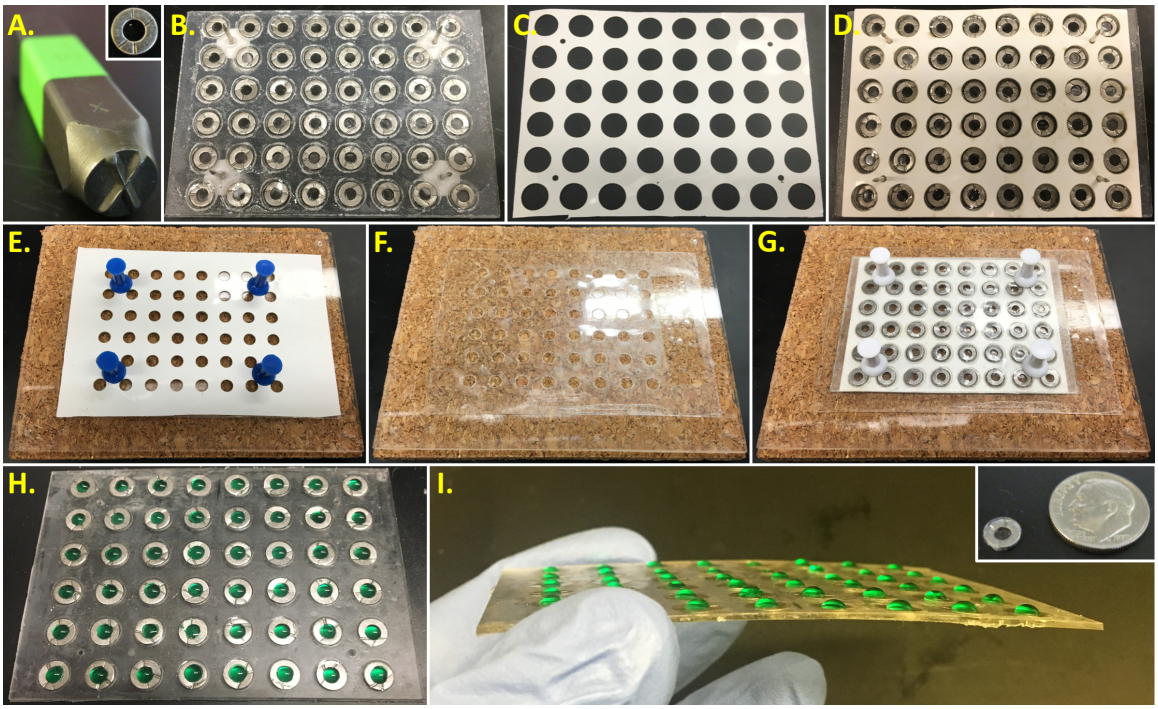

Figure 6.2: Manufacture of Genomechanics Rafts with Hydrophilic Islands. A. Stainless steel washers were stamped with Xs to identify the side to which cells would be attached. **B.** The stamped washers were added to a mold with 6 mm holes, which were filled with PDMS and cured. Another thin layer of PDMS containing fluorescent beads was added, enabling identification of the cell focal plane and facilitating cell localization during atomic force microscopy. **C.** A release liner was created to prevent adhesion to the area surrounding the rafts. **D.** Push pins were first used to align the raft mold to the release liner. **E.** A mask with an array of 3.6 mm holes, composed of polypropylene, silicone adhesive, and release liner layers, was pinned to a corkboard alignment tool. **F.** The release liner was removed from the mask, exposing the silicone adhesive. **G.** Using the alignment holes on the corkboard, the centers of the rafts and the mask holes were aligned. **H–I.** Hydrophilic islands were created by treating the rafts with oxygen plasma and removing the mask. Dyed water was employed to illustrate the hydrophobic barrier created by the mask; prior to dispensing cells onto the rafts, adhesive ligands were adsorbed to the hydrophilic islands and rafts were removed from the mold.

The washer filler material was chosen to be PDMS as an optically transparent material with sufficient stiffness to serve as the substrate for cell mechanics measurements [155]. As a pourable polymer, PDMS also enabled a scalable method of raft completion that did not require the use of potentially cytotoxic glues. PDMS

exhibits low levels of autofluorescence at lower wavelengths and is generally less autofluorescent than acrylic or polycarbonate [113]. Finally, PDMS is also known to be compatible with nucleic acids, as the Fluidigm microfluidic chips employed for PCR are composed of PDMS and PDMS adsorbs low levels of PCR sample compared to alternative materials [167].

Molds for curing the PDMS onto the stamped washers were created by first cutting an array of holes matching the washer outer diameter into a three-layer sheet of 1/32 in. acrylic, silicone tape (3M), and a release liner (3M) using a VLS3.50 laser cutter (Universal Laser Systems, Scottsdale, AZ). The cut sheet was cleaned, the release liner was removed, and the silicone tape was adhered to a clean polypropylene film, completing the mold.

After treating the mold with release agent (1 μL/mL Tween-20 in PBS) for 15 min, the washers were loaded into each well with Xs facing up. A mixture of PDMS pre-polymer and curing agent (5:1 v:v; Sylgard 184, Dow Corning) was poured into each well and degassed. The excess mixture was scraped off to ensure consistent 1/32 in. thickness of each raft, and the PDMS was partially cured at 100°C for 30 min.

To facilitate identification of the cell focal plane and enable cell localization within a small field of view, fluorescent beads were added to the top of the rafts. Thus, another layer of PDMS pre-polymer and curing agent containing fluorescent beads was spread thinly on top of the raft surface using a paint roller. The rafts were then cured completely at 100°C for 1 h (Fig. 6.2B).

As PDMS is naturally hydrophobic, a hydrophilic island was created at the center of the raft to enable coating with cell-adhesive ligands, whereas the still-hydrophobic edges facilitated lysate collection by manual pipetting of lysis buffer. The hydrophilic island also served to simplify the cell's environment by preventing contact with the washer for all stages of processing except AFM, which required full submersion of each raft. Oxygen plasma was used to create hydrophilic islands, but required a

mask to prevent plasma treatment, and thereby retain hydrophobicity, of the raft edges. Silicone tape was thus chosen to seal the edges of each raft.

The previously removed release liner (Fig. 6.2C) was aligned with the cured rafts using push pins (Fig. 6.2D), preventing the silicone tape from adhering too strongly to the acrylic mold and prematurely ripping the rafts out of the mold. A three-layer mask composed of polypropylene film, silicone tape, and release liner was laser cut with a hole array of 3.6 mm diameter, which was chosen to match the diameter of a 384-well plate, as the minimum resolution for cell dispensing given by the manufacturer of the cell sorter. The polypropylene layer of the mask was taped onto a corkboard alignment tool, using push pins to align the mask with the existing alignment holes (Fig. 6.2E). The push pins were then removed, and the release liner was removed, exposing the silicone tape (Fig. 6.2F). The raft mold, along with the first release liner and the push pins, were flipped and aligned to the mask (Fig. 6.2G). Finally, the mask was trimmed, and the silicone tape was press-sealed to the PDMS at the site of each raft, enabling maximum definition of the barrier between the hydrophilic plasma-treated islands and the hydrophobic untreated PDMS edges.

Although sterilization by autoclave diminished bead fluorescence, rafts were treated with 70% ethanol, exposed to ultraviolet light, and rinsed with sterile water to minimize cytotoxicity. Rafts were treated with air plasma for 6 min using a plasma cleaner (Harrick), creating the desired hydrophilic islands (Figs. 6.2H, 6.2I). The mask was immediately removed under a sterile biocabinet, and the cell-adhesive ligand Cell-Tak™ (Corning) was adsorbed onto the surface for 30 min according to the manufacturer's instructions. Following a wash with sterile water, rafts were removed from the molds and stored at 4°C for less than 1 week before use. In preliminary testing, of rafts visually identified to contain a single cell, Cell-Tak™ caused immobilization of 36% of cells following a wash step, whereas similar non-specific binding ligands, such as gelatin and poly-L-lysine, resulted in reduced cell retention (<5%).

Immediately prior to cell preparation, each raft was transferred to a custom 96-well pate and loaded with a 5 μL DMEM droplet, which supported cell viability without blocking the Cell-Tak™ adhesion sites. To prevent dehydration, a humectant composed of a sponge saturated with sterile water and acrylic layers to prevent disruption of the DMEM droplets was added to the well plate and sealed with pressure-sensitive optical adhesive film (ThermoFisher). The plate was stored on ice to reduce evaporation.

6.2.2 Cell Culture

Murine ESCs (D3 cell line, ATCC, Manassas, VA) were cultured in growth media (15% fetal bovine serum [Atlanta Biologicals, Atlanta, GA], 2 mM L-glutamine [ThermoFisher, Waltham, MA], 1x MEM non-essential amino acid solution [Mediatech, Herndon, VA], 0.1 mM 2-mercaptoethanol [ThermoFisher], and 100 U/mL penicillin, 100 μg/mL streptomycin, and 0.25 μg/mL amphotericin [PSA; Mediatech] in Dulbecco's modified Eagle's medium [DMEM; Sigma-Aldrich, St. Louis, MO]) on polystyrene Petri dishes treated with 0.1% gelatin (Millipore, Billerica, MA). Media was changed every other day, and cells were passaged at approximately 70% confluence. To encourage pluripotency, growth media was supplemented with 1.1 x 10^3 U/mL leukemia inhibitory factor (LIF; Millipore). Upon achieving pluripotent colonies, as identified by rounded morphology, differentiation was induced by culturing the mESCs in LIF- growth media.

6.2.3 Cell Staining

Although concerns have been raised that cell dyes can affect cell stiffness [89], the dyes were vital to cell localization in the present study, as it is challenging to find a single cell in a large area under brightfield illumination. Furthermore, no significant difference in stiffness was observed when day 0 mESCs were stained with 25 μM CellTracker™ Green CMFDA (ThermoFisher), the highest concentration recommended by

the manufacturer, and measured by atomic force microscopy on gelatin-coated glass (Fig. 6.3). Although the average stiffnesses differ between the unstained and stained cells, the ranges of the observed stiffnesses were well-aligned for both populations, with the exception of the stiffest stained cell.

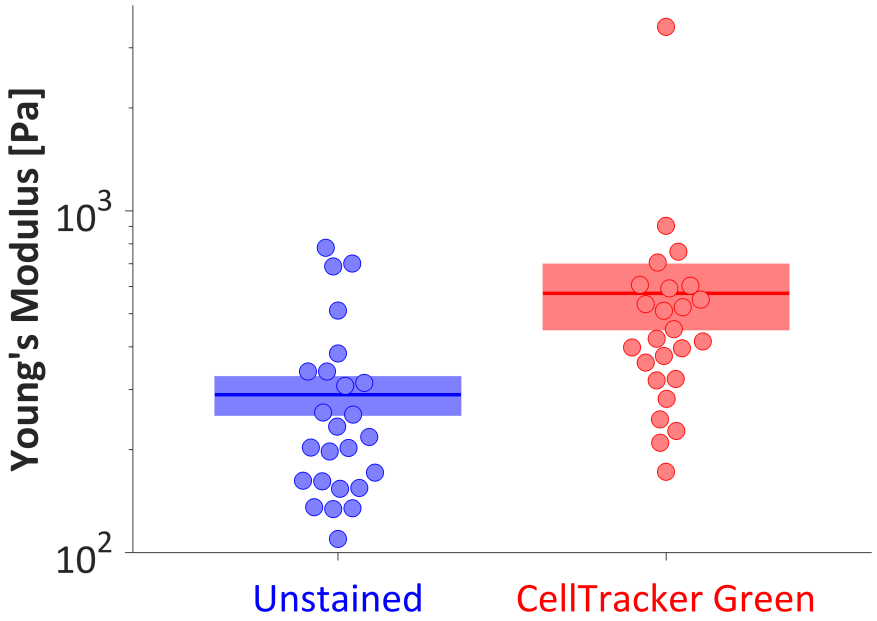

Figure 6.3: CellTracker™ does not Significantly Impact Cell Mechanics. There was no significant difference between untreated mESCs and mESCs treated with 25 μM CellTracker™ Green (p=0.208).

Whereas the fluorescent beads were easily distinguishable relative to background, the stained cells were less easily identified (see Fig. 6.5). The combination of green beads and red cells proved superior to the combination of red beads and green cells, which may have suffered from PDMS autofluorescence or bleedtrough from the red to the green channel. Therefore, mESCs were stained with 25 μM CellTracker™ Red CMTPX dye (ThermoFisher), using the manufacturer's protocol with the highest recommended dye concentration for maximal visibility. Prior to cell dispensing, cells were detached from the gelatin-coated dishes using a solution of 0.05% trypsin and 0.53 mM ethylenediaminetetraacetic acid (EDTA; Sigma-Aldrich), pelleted by centrifugation, dissociated by trituration, and stored on ice.

6.2.4 Single-cell Dispensing and Immobilization

A FACSAria Fusion™ cell sorter (BD Biosciences, San Jose, CA) was employed to identify single stained cells and to dispense 1 cell onto each raft (Fig. 6.4). Index sorting was employed such that the FACS parameters recorded by the instrument could be tracked to each individual raft. The humectant was immediately returned and the well plate was re-sealed. Cells were immobilized on Cell-Tak™ during 1-2 h incubation at 37°C.

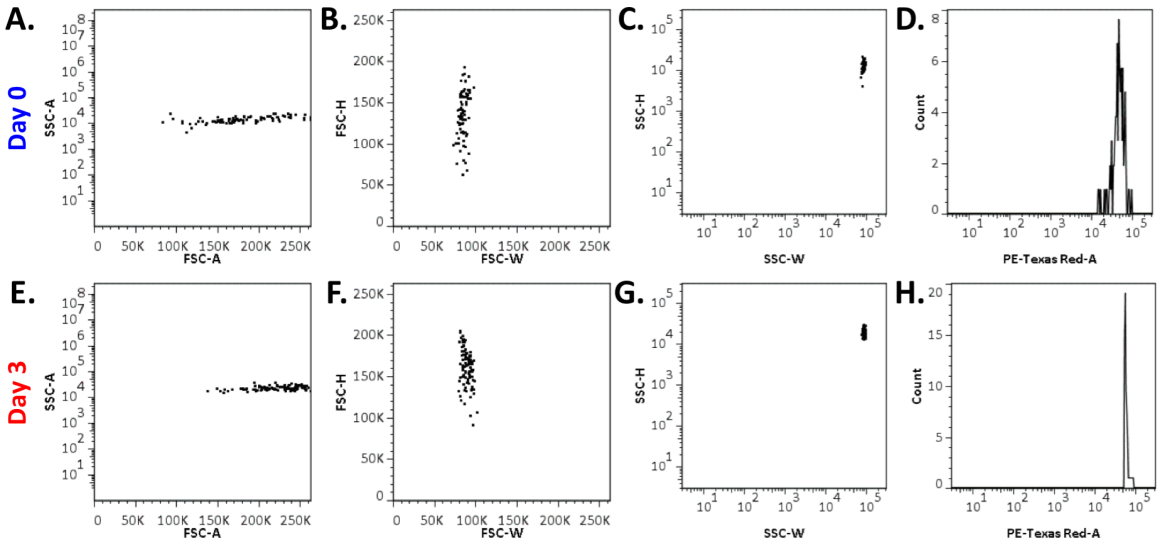

Figure 6.4: Single-cell Dispensing. **A.** Day 0 ESCs were first identified using a side scatter vs. forward scatter gate. **B.** A forward scatter-height vs. forward scatter-width gate was used to eliminate multi-cell clusters. **C.** A side scatter-height vs. side scatter-width gate further ensured the removal of clusters. **D.** Single cells with the brightest CellTracker™ Red signal (PE-Texas Red channel) were chosen for dispensing onto the rafts. **E–H.** Identical gates were applied for day 3 ESCs. On average, the day 3 cells were observed to be larger (i.e. higher forward scatter) than the day 0 cells.

6.2.5 Cell Localization

Following cell immobilization, rafts were washed twice with media, which has been empirically determined to remove cells that were not sufficiently adhered for AFM probing. As the acrylic-containing humectant was observed to be autofluorescent, a custom silicone lid was used during imaging. A Cytation™ 3 imaging plate reader

(BioTek) was employed to identify cell location, while maintaining the well plate at 37°C and 5% CO_2. Using a 4x objective, a 2x2 montage of each raft was sufficient to image the inner diameter of each washer. The GFP channel enabled automatic focusing on the bead focal plane, which corresponded with the cell focal plane. The Cy5 channel was then used to determine the absence or presence of a cell on each raft (Fig. 6.5).

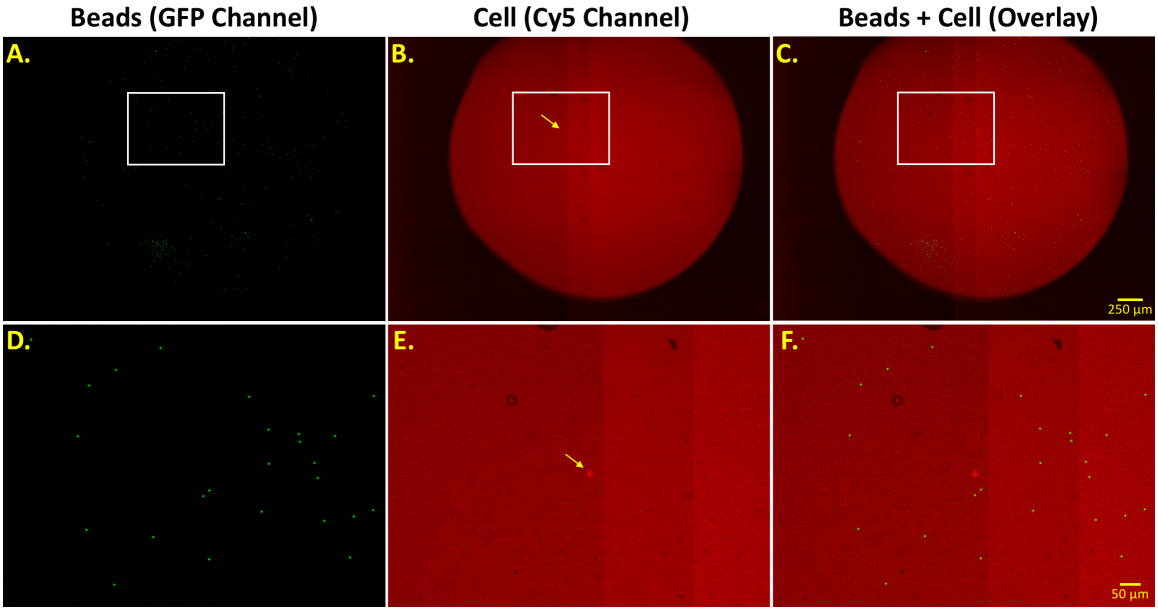

Figure 6.5: Cell Localization. A. The imaging plate reader first focused on the beads (GFP channel) in the center of each well to identify the top surface of each raft. A 2x2 montage was then constructed, generating an image of the entire inner diameter of the washer. **B.** A montage of the cell (Cy5) channel was then constructed to identify cell location (yellow arrow), using the bead channel for stitching. The cell montage was used to detect the presence or absence of a cell on each raft. **C.** An overlay of the bead and cell channels was used to locate the cell during atomic force microscopy. Scale bar, 250 μm. **D–F.** Magnified images (Panels A-C, white boxes) aided identification of the cell location (yellow arrow). Scale bar, 50 μm.

6.2.6 Atomic Force Microscopy

To simplify the tip-cell contact geometry, 5.5 μm polystyrene beads were attached to tipless silica nitride cantilevers (Bruker Probes, Camarillo, CA) using two-part epoxy, and dried overnight. Mechanical properties of individual cells were obtained from

force-indentation curves recorded with an atomic force microscope (Asylum Research, Santa Barbara, CA) with an integrated optical microscope (Nikon, Melville, NY) on a vibration isolation table. Photodetector calibration was performed on a PDMS raft lacking adhesive ligands and cells, which was sufficiently stiff to obtain a calibration curve similar to curves obtained on glass substrates (Fig. 6.6). The Sader calibration method [123] was used to obtain cantilever spring constants (k=10-13 pN/nm) based on the thermal vibration of the cantilever.

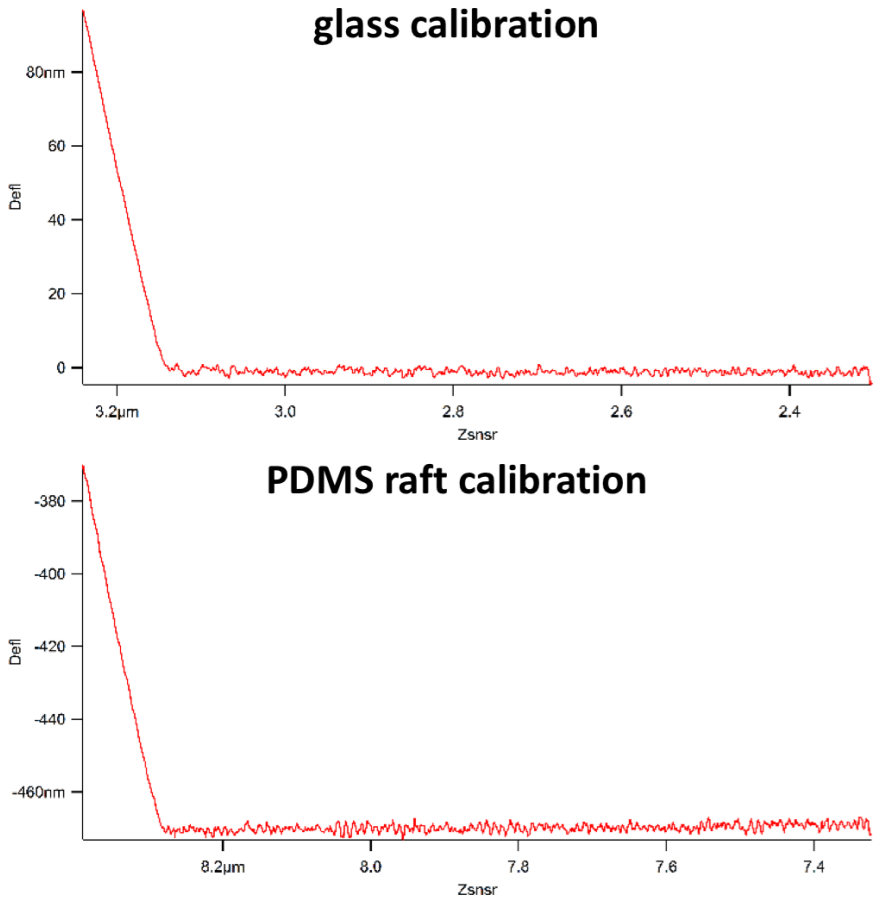

Figure 6.6: Atomic Force Microscopy Calibration Curves. PDMS is softer than glass or polystyrene, which are typically employed for AFM cell mechanics measurements. However, given the relatively low spring constant of the cantilever (10-13 pN/nm), the calibration curves obtained on glass (top) and PDMS (bottom) were similar. The similar slopes of the deflection vs. Z-sensor curves, which are proportional to force vs. indention curves, indicate that the difference in Young's modulus between glass and PDMS had a negligible effect on the cellular Young's modulus calculations.

Rafts were transferred to a glass-bottom dish containing phosphate-buffered saline (PBS; with calcium and magnesium), and raft orientation was verified using the stamped Xs. As cell stiffness is sensitive to temperature [116], measurements were taken in room temperature PBS to reduce variability. The cell focal plane was identified using the fluorescent beads (FITC channel), which also enabled rotational orientation. The cell was then located relative to the beads using images taken with the plate reader. Brightfield illumination was used to visually align the cantilever probe with the cell center. The probe was translated to indent the cell with a velocity of 2 μm/s until a force trigger of 5 nN was reached.

To calculate the cellular Young's modulus, the Hertzian contact model was fit to the compression segment of the force-indentation curve over the applied force range of 2.5-4.75 nN, where the Young's modulus was largely independent of the indentation. The cells were taken to be incompressible (cellular Poisson's ratio = 0.5). The Young's modulus of each cell was calculated as the average of 3 independent measurements.

Immediately following each measurement, rafts were transferred to a magnetic surface to prevent movement. Residual liquid was removed by manual pipetting. 5 μL lysis buffer (CellsDirect™ 2x reaction mix [ThermoFisher] containing 1 U/μL SUPERase In™ RNase inhibitor [ThermoFisher] to prevent degradation) was pipetted onto the raft and then transferred to a PCR plate on ice. After all measurements were complete, the lysate samples were stored at -80°C.

6.2.7 Primer Validation

Primers were obtained from Invitrogen, as listed in Table 6.1, and resuspended in DNA suspension buffer (Teknova, Hollister, CA).

Table 6.1: Primer Sequences. Primers employed for pre-amplification and PCR.

Gene	Forward Sequence (5' to 3')	Reverse Sequence (5' to 3')
m18S	GTAACCCGTTGAACCCCATT	CCATCCAATCGGTAGTAGCG
mGAPDH	CATGGCCTTCCGTGTTCCTA	CCTGCTTCACCACCTTCTTGAT
mISL1	ATGATGGTGGTTTACAGGC	TCGATGCTACTTCACTGCC
mPOU5F1	CCGTGTGAGGTGGAGTCTGGAG	GCGATGTGAGTGATCTGCTGTAGG
mS18	CTCTAGTGATCCCTGAGAAGTTCC	ACTCGCTCCACCTCATCCTC

Primer pairs were designed using Primer3 and validated for RT-qPCR through amplification of cDNA prepared with the CellsDirect™ One-Step qRT-PCR kit (ThermoFisher) and run on a StepOne Plus with SYBR Green detection chemistry (ThermoFisher). Amplification traces were baseline corrected and amplification efficiencies were measured using LinRegPCR software [121, 122, 149]. Melt curves were used for preliminary screening of primer pairs for primer dimers and multi-product reactions, and all primer products were validated for length and specificity using gel electrophoresis on a 1% agarose gel run in 1.5x TAE buffer.

6.2.8 Gene Expression

Lysed cells were mixed with the pooled set of primers (normalized to 500 nM), SuperScript® III RT Platinum® Taq Mix, and nuclease-free water. A thermocycler was used to convert RNA to cDNA, with reverse transcription occurring at 50°C for 15 min, followed by reverse transcriptase inactivation and Taq activation at 95°C for 2 min. To amplify the cDNA using the pooled primers, the sample was exposed to 20 cycles of 15 s at 95°C and 4 min at 60°C. The cDNA samples were stored at 4°C.

cDNA samples were then processed with exonulcease I to remove any unincorporated primer and diluted 5-fold. 3 μL of each sample and primer mix was prepared for the Fluidigm FLEXsixIFC chip. Finally, a Fluidigm Biomark was used to thermal cycle the chip 30 times and read the amplification via EvaGreen® fluorescence.

C_t values and threshold fluorescence signals were obtained using the Fluidigm Real-Time PCR Analysis software package with automatic detector thresholds. Initial target DNA concentrations were calculated as previously described [78], using $N_0 = \frac{t}{\epsilon^{C_t}}$, where t is the threshold fluorescence signal for each target, C_t is the threshold cycle for each sample, and ϵ is the reaction efficiency, assessed as the mean efficiency calculated using LinRegPCR software. Gene expression fold-changes were calculated using the ΔC_t method, with the housekeeping gene as m18S. m18S ΔC_t values were not included in the correlation analysis, as the values are defined as 1.

Initially, the expression levels of mSOX2, mMYF5, mPAX6, mLMNA, mACTN1, and mMAP2 were also measured. However, the low abundance of the target genes precluded PCR amplification, and the genes were removed from the analysis. mNANOG only amplified in one sample, and was excluded from analysis as the sample size was not sufficient to calculate correlation coefficients.

6.2.9 Lysate Recovery Testing

To assess the manual pipetting method of cell lysis, lysate obtained from genomechanics rafts with positively identified cells were compared to samples in which cells were dispensed directly into lysis buffer using the cell sorter.

cDNA libraries from mESCs were prepared and pre-amplified using the CellsDirect™ One-Step qRT-PCR kit (ThermoFisher) with 20 cycles of pre-amplification according to manufacturer's instructions. Standard curve libraries were prepared from samples containing 8, 4, 2, 1 or 0.5 cells (0.5 cells = 1 cell diluted twice), as counted by the cell sorter. Comparison libraries were created for single cells lysed manually on

genomechanics rafts. 8-cell libraries that were pre-amplified without Taq polymerase ("Taq-"), as well as RT-qPCR reaction mixtures without template cDNA, served as negative controls. cDNA was run in a StepOne Plus with SYBR Green detection chemistry (ThermoFisher) with 500 nM mGAPDH primers (see Table 6.1).

Amplification curves resulting from both 1 and 3 μL lysate displayed consistent C_q values (Fig. 6.7A), suggesting a low signal-to-noise ratio. Thus, similarly to digital droplet PCR analysis, the percentage of samples reaching the threshold amplification was considered (Fig. 6.7B). Within the 1 cell/sample group, a higher percentage of samples amplified for manually pipetted lysis buffer than direct-to-buffer FACS dispensing, suggesting the validity of the manual pipetting method.

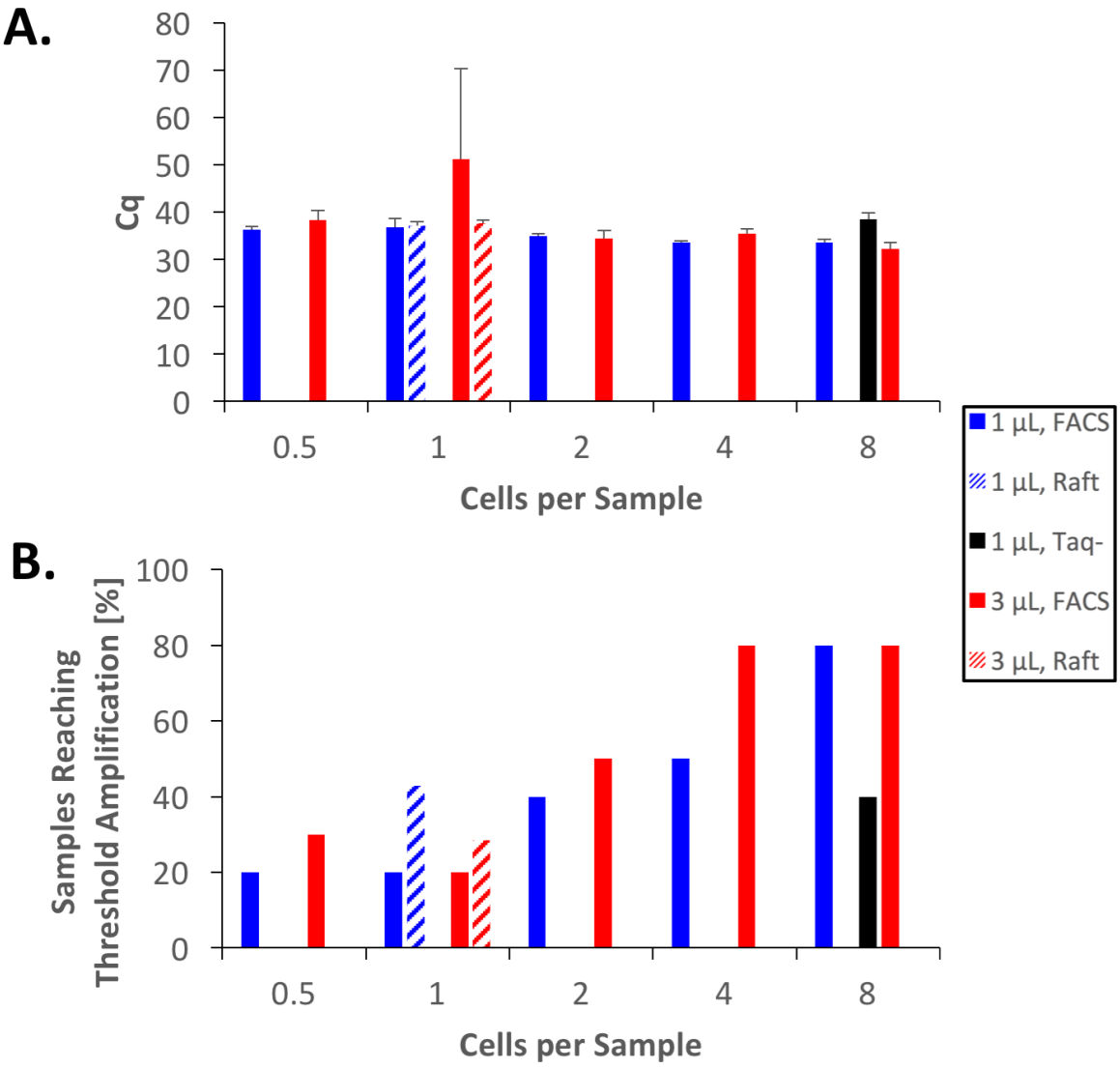

Figure 6.7: Cell Lysate Recovery. A. On the basis of C_q, differences among 1 μL samples (blue), 3 μL samples (red), and Taq- controls (black) were not discernible, indicating a low signal-to-noise ratio given the low number of cells per sample. Error bars indicate mean $\pm$ standard error. **B.** Therefore, samples were compared based on the percentage of samples that amplified (i.e. reached the threshold amplification). The percentage of samples that amplified generally increased with the number of cells per sample, as expected. Lysate samples obtained by pipetting following cell adhesion to the rafts (striped bars) were more likely to amplify than lysate samples obtained by directly dispensing cells into lysate buffer using fluorescence-activated cell sorting (FACS; solid bars), suggesting the validity of the manual pipetting lysis method.

6.2.10 Statistics and Figure Generation

Bootstrapping ANOVA was performed using a custom code in MATLAB (MathWorks, Natick, MA) to discern statistically significant differences and apply Holm's p-value adjustment (α=0.1), as previously reported [19]. Spearman's rank correlations were assessed by first using JMP statistical software (SAS Institute, Cary, NC) to obtain coefficients and raw p values and subsequently using a custom Microsoft Excel spreadsheet to apply Holm's p-value adjustment (α=0.1) and plot the resulting color matrices (Fig. 6.10). Beeswarm plots (Fig. 6.3) and semitransparent scatter plots (Fig. 6.9) were generated using a custom MATLAB code.

6.3 Results

Force-indentation curves of day 0 (LIF+) and day 3 cells (LIF- for 3 days) indicated that the pluripotent day 0 cells were softer than the differentiating day 3 cells (Fig. 6.8), in agreement with previous findings (Chapter 5, [81, 106, 112, 139]).

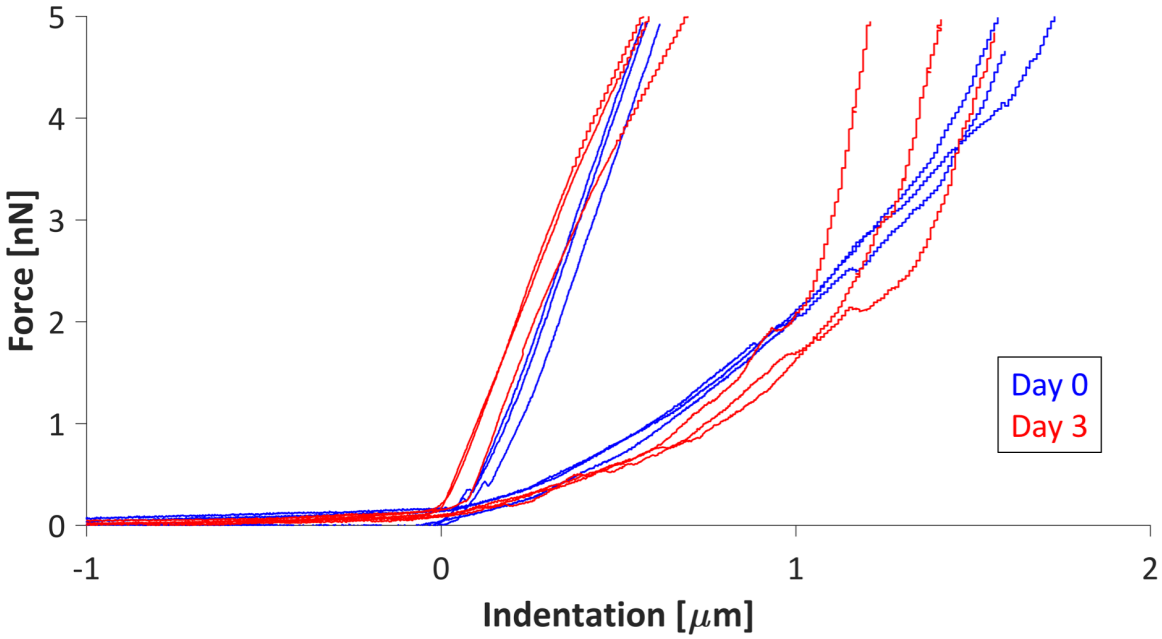

Figure 6.8: Cell Stiffness Probed by Atomic Force Microscopy. Cell stiffness, which is related to the slope of the force-indentation curve, was lower for day 0 cells (blue, mean=2.3 kPa, n=12 cells) than day 3 cells (red, mean=4.0 kPa, n=8 cells). The curves depict 3 independent measurements of 2 representative cells selected from each population.

Correlations among pairs of FACS, mechanics, and gene expression parameters were considered, with gene expression data based on either raw N_0 values or ΔC_t values normalized by the housekeeping gene m18S (Figs. 6.9, 6.10). Interestingly, one day 3 cell had a similar expression of the pluripotency gene mPOU5F1 compared to the day 0 cells (see Fig. 6.9, Young's modulus vs. mPOU5F1, top-left). The differentiation state of the individual day 3 cell was more characteristic of the day 0 population than the day 3 population, indicating potential asynchronous differentiation. Importantly, such a result would be very difficult to obtain using traditional population-based comparisons of pluripotent and differentiated cells; the single-cell genomechanics method was necessary to parse out asynchronous differentiation effects.

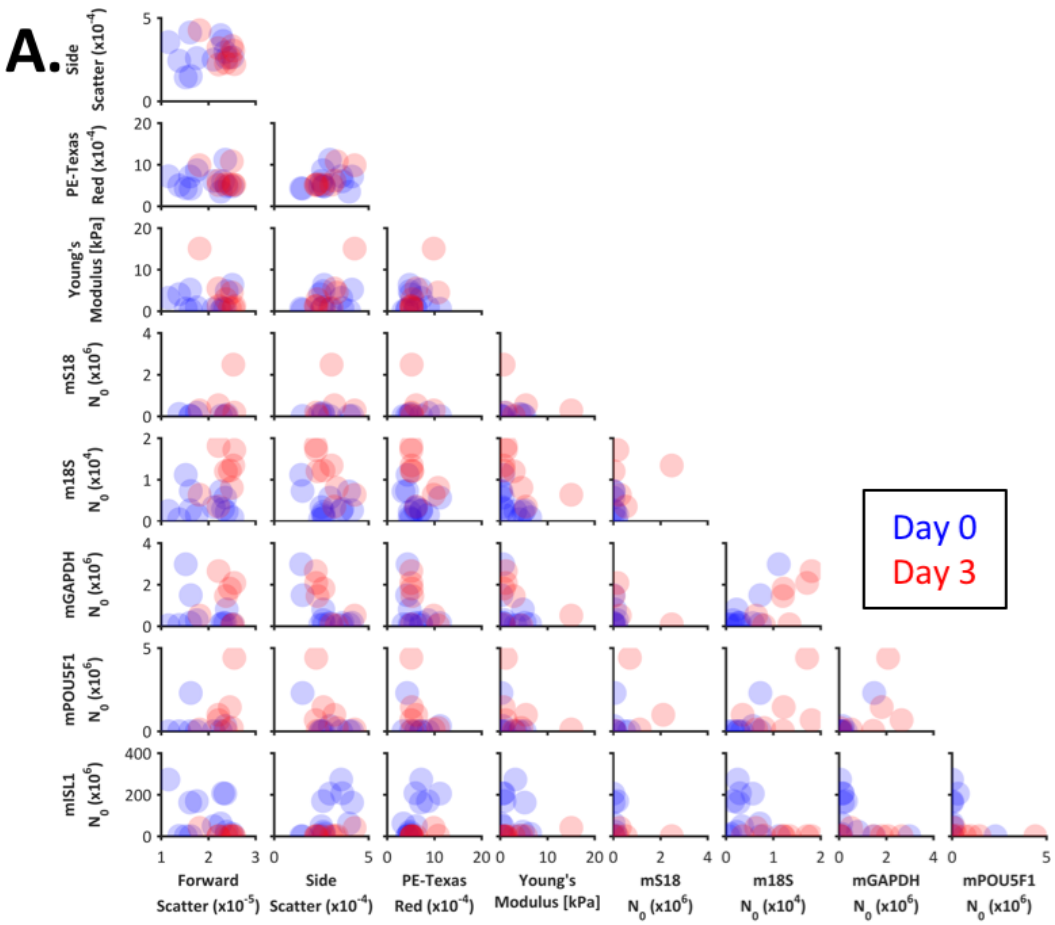
A.
Day 0
Day 3
Forward Scatter (x10^-5)
Side Scatter (x10^-4)
PE-Texas Red (x10^-4)
Young's Modulus [kPa]
mS18 N0 (x10^6)
m18S N0 (x10^4)
mGAPDH N0 (x10^6)
mPOU5F1 N0 (x10^6)
mISL1 N0 (x10^6)

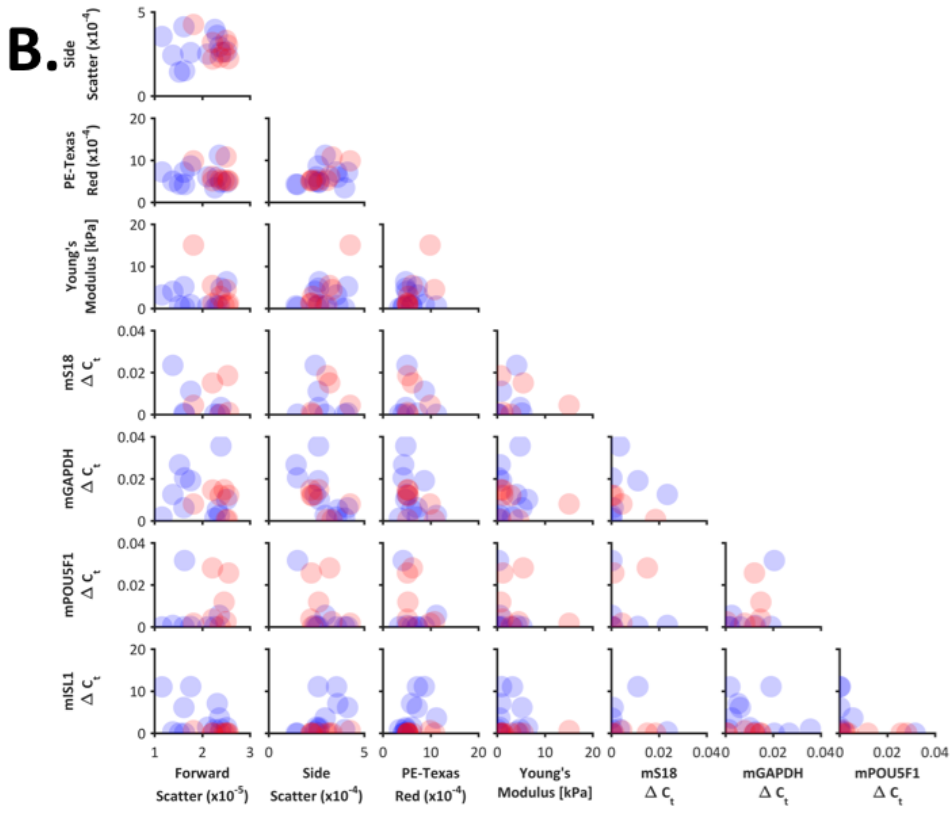
B.
Forward Scatter (x10^-5)
Side Scatter (x10^-4)
PE-Texas Red (x10^-4)
Young's Modulus [kPa]
mS18 ΔCt
mGAPDH ΔCt
mPOU5F1 ΔCt
mISL1 ΔCt

Figure 6.9: Pairwise Comparisons between FACS, Mechanics, and Gene Expression Data, based on Initial Number of Molecules. A. Based on the initial number of molecules calculation (N_0), the cellular Young's modulus appeared to decrease with the pluripotency gene mPOU5F1 and increase with the differentiation gene mISL1, suggesting that single-cell stiffness is inversely related to differentiation. Interestingly, a day 3 cell (red) with low Young's modulus displayed mPOU5F1 expression similar to the day 0 cells (blue; see top-left of Young's modulus vs. mPOU5F1 plots). Such an observation, which may be explained by asynchronous differentiation, would be difficult to detect with population methods, which typically average cells based on the day of differentiation. **B.** Similar observations were made for the ΔC_t values calculated by normalizing gene expression data to the housekeeping gene m18S.

Spearman's correlations were calculated to detect monotonic trends among the FACS, mechanics, and gene expression parameters. Significant positive trends between N_0 and ΔC_t values for each gene indicated that the analysis was not strongly affected by normalization (Fig. 6.10). Although not statistically significant, the negative correlation between Young's modulus and pluripotency (mPOU5F1), coupled with the positive correlation between Young's modulus and differentiation (mISL1), suggests that the genomechanics method is capable of detecting an inverse single-cell relationship between stiffness and potency, which has been observed previously in cell population studies (Chapter 5, [106, 112]). Importantly, the stiffness-potency relationship was observable without taking the known day of differentiation into account, emphasizing the ability of the single-cell genomechanics method to operate independently of the typical day of differentiation gold standard, which is hampered by the faulty assumption that differentiation is synchronous.

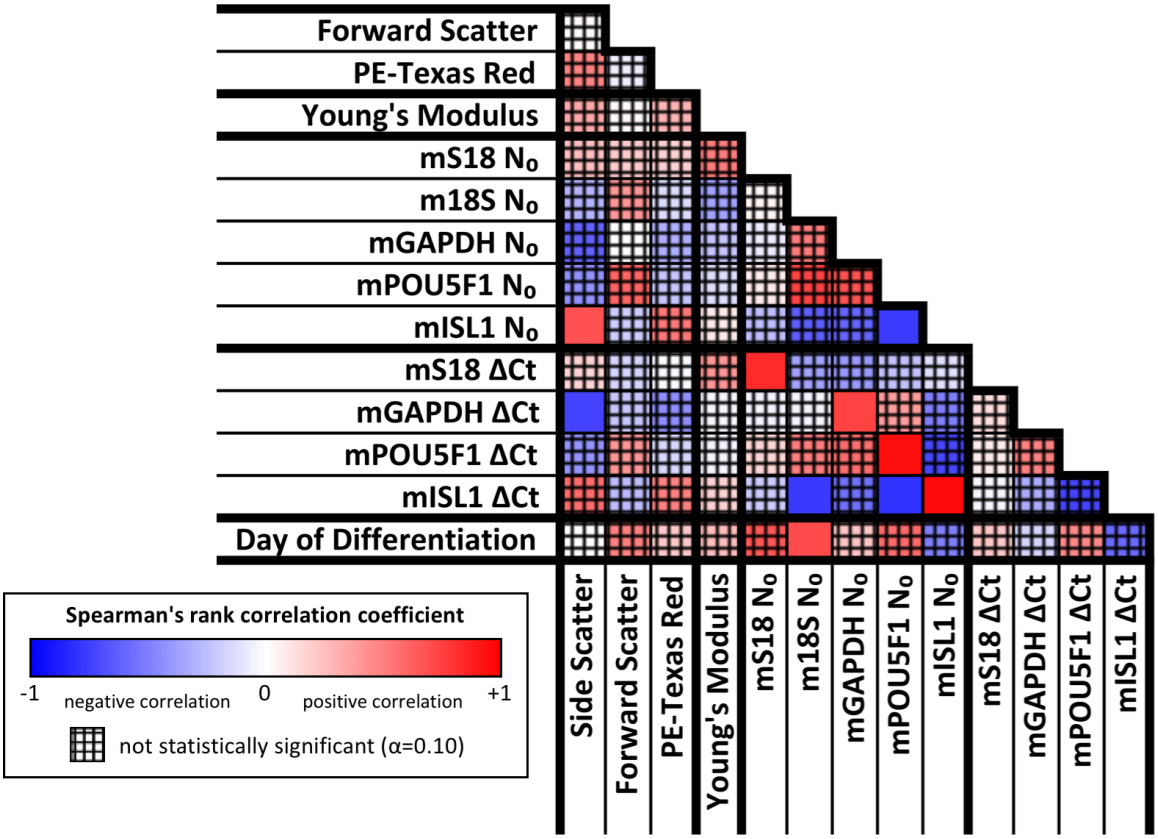

Figure 6.10: Single-Cell Genomechanics Correlation Color Map. Spearman's correlations were calculated to detect monotonic trends among the FACS, mechanics, and gene expression parameters. Although not statistically significant, the negative relationship between Young's modulus and mPOU5F1 and the positive relationship between Young's modulus and mISL1 support the conclusion that the genomechanics method is capable of detecting a single-cell relationship between cell stiffness and potency. Strong, positive relationships between N_0 and ΔC_t values for each gene indicate that results generally hold regardless of the whether normalization is applied. Blue, negative Spearman's correlation coefficient (indirect relationship); red, positive Spearman's correlation coefficient (direct relationship); white, zero Spearman's correlation coefficient (no correlation); cross-hatch, non-significant p-value.

6.4 Discussion

Considered as populations, the pluripotent day 0 cells were, on average, softer than the differentiating day 3 cells, in agreement with previous studies (Chapter 5, [81, 106,112,139]). However, the single-cell genomechanics method enabled more detailed analysis of biomechanical and biomolecular heterogeneity, revealing a soft cell in the

day 3 population that expressed the pluripotency marker mPOU5F1. Thus, the method enables the relationship between cell mechanics and biology to be examined with more resolution than previous techniques.

Within the context of stem cell differentiation, the ability of the genomechanics method to change the differentiation-defining gold standard would be particularly profound. Recent computational techniques hold the capacity to develop time-independent differentiation progress metrics from RNA sequencing data [143]. Redefining differentiation state independently of the day of differentiation, in combination with the genomechanics method, would enable a clearer understanding of the mechanical changes stem cells undergo during differentiation; importantly, such understanding would be unfettered by asynchronous differentiation, which confounds current techniques.

Broadening the scope of this study beyond stem cells would enable the genetic underpinning of cell mechanical heterogeneity to be more easily understood. The coefficient of variation of cellular Young's modulus typically exceeds 50%, even for clonal cell populations, but the single-cell genomechanics method can be employed to shed light on the biological sources of biomechanical heterogeneity, such as cell cycle, cell structure, and physiological state. Furthermore, single-cell genomechanics can be used to clarify the relative contribution of the cell structure components (e.g. nucleus, actin, intermediate filaments, microtubules) to overall cell stiffness, which is often debated.

The genomechanics technique is easily expandable to other genes by simply changing the primers used during PCR. Further such experiments of ESCs will seek to fortify understanding of the interplay between cell mechanics, cell structure, and differentiation by investigating genes related to pluripotency, lineage specification, nuclear structure, cytoskeletal structure, and cell cycle.

The majority of cell types is also compatible with the method presented herein.

As cells are immobilized to the rafts using a non-specific protein surface, even non-adherent cell types can be adapted to the technique; indeed, even pluripotent ESCs do not adhere to standard tissue-culture polystyrene, and gelatin or other substances must be employed for cells to adhere during routine cell culture. Even if a given cell type did not adhere to the rafts as currently designed, the adhesive surface can easily be changed to virtually any charged adhesive ligand and adsorbed following oxygen plasma treatment. The ability to study other cell types enables the investigation of questions beyond the realm of stem cell biology. Cell stiffness is well known to inversely correlate with metastasis [32, 162], but single-cell analysis would enable further study of the role of cell cycle on stiffness. Furthermore, cell systems containing subsets with well-defined biomolecular signatures but low prevalence, such as cancer and immunology, could be studied at the single-cell level to elucidate the potential of cell stiffness as a phenotype-specific biomarker.

Interestingly, future single-cell genomechanics studies may elucidate the temporal responses of genes, proteins, and mechanics to differentiation; indeed, previous studies suggest that, in response to differentiation, cell stiffness may change before morphology (Chapter 5) and morphology may change before pluripotency marker expression [98]. Thus, asynchronous differentiation may affect, to varying degrees, the extent of heterogeneity with regard to gene expression, protein expression, cell morphology, and cell mechanics.

The present study employed a novel technique to measure stem cell mechanics and gene expression at the single-cell level, permitting the observation that ESC stiffness increases during differentiation, regardless of the effects of asynchronous differentiation. The method is broadly applicable to answering various questions relating the biological and mechanical states of cells.

CHAPTER VII

CONCLUSION

7.1 Summary

Overall, cell stiffness has been shown as a stemness indicator in mesenchymal stem cells, limbal stem cells, and mesenchymal stem cells. Importantly, cell stiffness is a label-free, sorting-compatible marker, as evidenced by the ability to enrich for pluripotent embryonic stem cells using microfluidic stiffness-based sorting technology. By simplifying the complicated cell structure to a simple spring via the Young's modulus, pluripotent or differentiated cells can be identified from a heterogeneous population, as summarized in Fig. 7.1.

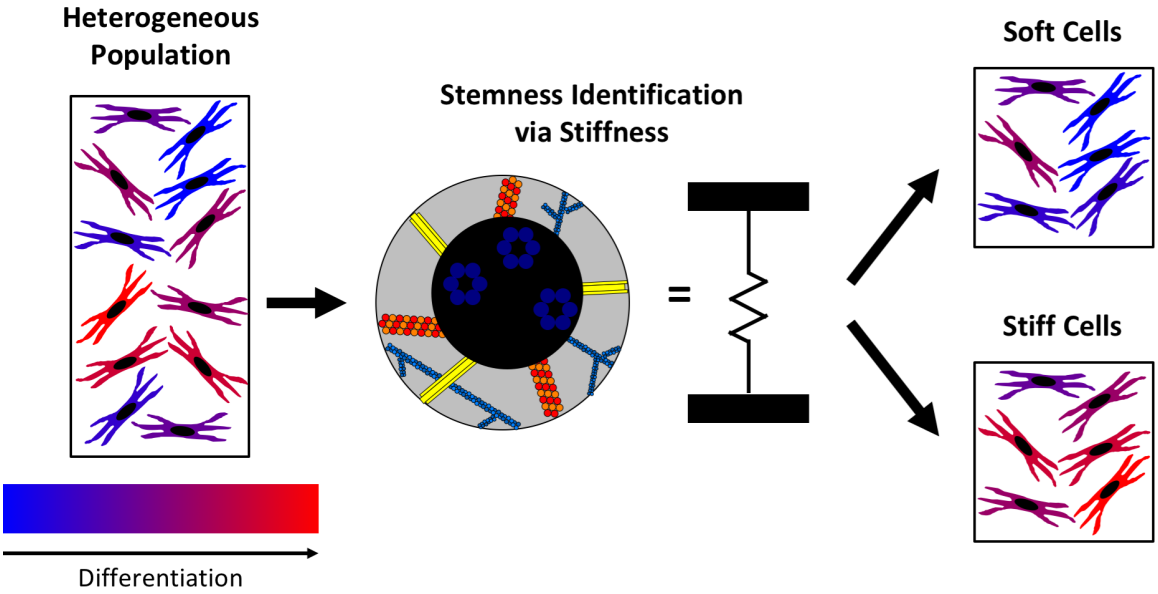

Figure 7.1: Summary. Starting with a heterogeneous population of cells, including cells with high potency (blue) and low potency (red), stemness can be identified via cell stiffness. The cellular Young's modulus represents a simple metric that integrates the complicated cell structure, including the nucleus (black), actin (blue-green), intermediate filaments (yellow), and microtubules (red-orange). Single-cell stemness can be identified using atomic force microscopy, or microfluidic sorting can be employed to separate a cell population into stiffness subsets, resulting in enriched populations of undifferentiated (blue) and differentiated cells (red).

7.2 Mechanical Stiffness as an Improved Single-cell Indicator of Osteoblastic Human Mesenchymal Stem Cell Differentiation

The stiffness of hMSCs was determined to decrease during osteoblast differentiation, which agreed with some studies, but contradicted others. In contrast to other studies, a novel method of location registration was employed, enabling first-ever single-cell correlations between cell mechanics and protein expression, as assessed by fluorescently tagged antibodies. Thus, using the day of differentiation as the gold standard of differentiation state, cell stiffness was determined to be more predictive of differentiation than the traditional biomolecular markers, osteocalcin and bone sialoprotein.

The follow-up work to this study sought to replace the protein markers by highly multiplexed genetic markers. However, the gridded Petri dish registration technique

still holds great promise for simplified correlation studies at the single-cell level. The hMSC study was complicated by the relatively slow and low-level secretion kinetics of osteoblasts; however, the technique may be employed with other cell types that have faster secretion times or better studied surface protein expression. Furthermore, secretion inhibition compounds may be used to maximize the signal in cells with slow or low-level protein production, enabling more detailed comparisons between the kinetics of protein secretion and mechanics changes.

Although the slow growth rate of hMSCs hampered their use in subsequent cell sorting experiments, which require high cell numbers, interesting questions remain regarding the relationship between mechanics and hMSC differentiation. It would be interesting to study mechanics within the context of the Dominici criteria [41] and investigate the relationship between levels of hMSC markers (e.g. CD73, CD105, CD166) and cell stiffness.

7.3 Cellular Stiffness as a Novel Stemness Marker in the Corneal Limbus

The first characterization of limbal stem cell mechanics was performed, yielding the conclusion that LSCs are softer than both in vivo- and in vitro-differentiated cells. Mechanics have been characterized in various cell systems, but this work was connected to the broader context of cell sorting using sensitivity analysis. The diagnostics odds ratio (DOR) was calculated as an overall metric of a parameter's utility to classify samples into groups (in this case, to classify cells by potency). The resulting receiver operating curves provide a useful framework, both specifically within the context of LSCs for the improvement of corneal therapies and generally within the broader context of bioprocessing, with applications to improve the design of cell sorting devices.

High-throughput, microfluidic separation technologies require cells to be in suspension. Thus, to move from investigation of stiffness as a stem cell biomarker to

phenotypic stiffness-activated cell sorting, further understanding of cells in the suspended state is required, as differences in mechanical properties between adhered and suspension cells may exist [34]. Adherent cells typically express integrins, which are intimately involved in mechanosensing and mechanotransduction through control of cytoskeletal structure [33]. Mechanical forces induce the assembly of focal adhesions, triggering integrin-dependent signaling [33]. Integrins are also connected to the nucleus through cytoskeletal filaments, which may result in mechanical niche-induced nuclear changes [33]. Additionally, naive hMSCs have been shown to stiffen in tens of minutes after suspension [92]. In spite of these facts, the DOR based on adherent-cell stiffness was shown to be correlated with the stiffness-based sorting DOR, which operates on suspended cells, for various cell types. Furthermore, although the absolute cell stiffness is known to change based on attachment state, the relative cell stiffness values between cell types are robust to attachment state (Fig. 7.2). Further study to fortify this understanding, perhaps employing optical tweezers, which can operate on suspended cells, will be necessary to pin down the relationship between cell mechanics and cell attachment.

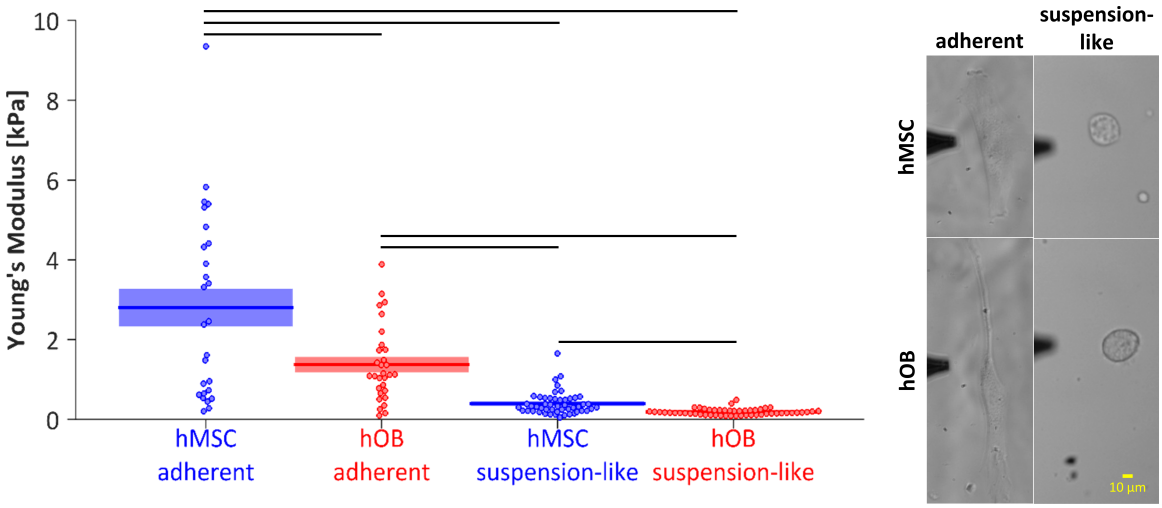

Figure 7.2: Relative Differences in Young's Modulus between Cell Types does not Depend on Attachment Time. The Young's moduli of adherent (20-32 h adhesion time) and suspension-like (15 min adhesion time) human mesenchymal stem cells (hMSCs) and human osteoblasts (hOBs) were statistically distinct, indicating that relative stiffness differences between cell types are detectable for populations with similar attachment times. Populations connected by black bars are significantly different (Holm's adjusted p-values, α=0.10). Young's moduli of adherent hMSCs and hOBs replotted from [19].

7.4 Biophysical Subsets of Embryonic Stem Cells Display Distinct Phenotypic and Morphological Signatures

Although mESCs were already known to stiffen during differentiation, the phenomenon was validated and refined by considering multiple days of differentiation. The mESC stiffening effect was observed to take place in only 1 day for cells differentiated by LIF removal and measured on a poly-L-lysine substrate. Additionally, the soft biophysical subset of partially differentiated cells, which were produced using a microfluidic sorting device, were shown to be morphologically, mechanically, and genetically similar to pluripotent (LIF+) mESCs.

As a follow-up study of mESC biophysical subsets, it would be interesting to assess the clonogenicity of each biophysical subset by plating cells onto gelatin-coated 96-well plates at a low, clonal density and culturing the cells until colonies formed. Cell morphology and alkaline phosphatase staining could be used to functionally

assess pluripotency [99, 100, 148] in a high-throughput, automated manner. A live-cell alkaline phosphatase stain, available from ThermoFisher (#A14353), could be employed for fast readouts of potency. Similar studies could also be conducted to assess differences in differentiation potential among biophysical ESC subsets.

Since cell nuclei are generally observed to be stiffer than the cytoskeleton [119] and ESC nuclei occupy a large volume of the cell [112], the ESC stiffness would be expected to change along with nuclear stiffness. Further exploration of this relationship could be completed by isolating cell nuclei and comparing overall cell stiffness to nuclear stiffness. Additionally, location registration techniques, such as the gridded Petri dish, could be used to assess the relationship between mechanics and imaging parameters derived from a fluorescent nuclear dye, such as DAPI or Hoechst.

Additional biophysical subset studies can be performed to identify whether stiffness is heritable. After obtaining biophysical subsets and verifying distinct mechanical parameters, the magnitude of changes to the parameters during extended cell culture would reveal the kinetics and robustness of initially mechanically distinct subsets. Mechanical heritability has previously been assessed in the context of mechanotransduction [163], but changes to the endogenous cell mechanics have not been addressed.

Whereas the relationship between cell mechanics and cytoskeletal structure is well understood in spread cells, such as hMSCs, the relationship is less understood in epithelial-like cells, such as mESCs. Investigation of cell structure, either based on the day of differentiation or on biophysical subsets, could be achieved by staining cells for nuclear material, F-actin, microtubules, and intermediate filaments (e.g. cytokeratins, vinculin).

To further understand the relationship between nuclear structure and mechanics, the epigenetics and chromatin structure of cells could be assessed post-sort. As stem cell populations may be derived from a single clone, variable gene expression and epigenetics may be observed within a population although the gene sequence

is identical. One particular target for epigenetic investigation is Lamin A (LMNA), which is known to modulate nuclear stiffness [85]. Interestingly, CpG island promoter hypermethylation is known to inactivate LMNA in 50% of leukemia and lymphoma cell lines [1]. Furthermore, long-lived cytoskeletal structures may act as epigenetic determinants of cell shape, function, and fate [51]. Recent methods for single-cell epigenetics [16] may also enable more detailed study of the relationships between epigenetic states and mechanical properties.

High LMNA expression is known to correlate with stiff nuclei [85], and LMNA is known to increase with hESC differentiation (before Oct-3/4 decreases, but after Tra-1-60 decreases) [28]. If similar trends hold in mESCs, chromatin compaction via LMNA hypermethylation may be implicated in ESC stiffening during differentiation.

The sorting trajectories of single-population pluripotent or differentiating ESCs suggested that low flow rates would produce a high enrichment factor for pluripotent cells, with approximately 90% of the pluripotent cells reaching the soft outlet (Figs. 5.9E, 5.9F). However, upon sorting a mixed population of pluripotent and differentiating cells, the diagnostic odds ratio was only 1.9 (Fig. 5.8). Diminished sorting efficiency may have been caused by 1) difficulty in distinguishing pluripotent from differentiating cells after sorting or 2) interaction effects between the cell types.

CellTracker™ dyes were employed to distinguish pluripotent from differentiating cells, and performed well for unmixed, singly-stained cell populations, even following an incubation step that simulated the ambient temperature and mixing conditions experienced during sorting. However, upon mixing cell populations stained with each CellTracker™ dye, the fluorescence spectra shifted together and became more difficult to distinguish. As the percentage of cells that could not be definitively classified as pluripotent or differentiating increased, so the sorting efficiency of the device was dampened. Due to the combined effects of potential "cross-talk" between dyes and the implicit, but potentially inaccurate, assumption of synchronous differentiation in

differentially staining entire cell populations, gene expression targets were ultimately chosen as additional indicators of differentiation and sorting efficiency.

Interaction effects between the pluripotent and differentiating cells may have also reduced the sorting efficiency. Notably, the differentiating cells were observed to be more adhesive than the pluripotent cells. Thus, clusters containing both pluripotent and differentiating cells may have formed, unpredictably dispersed while traversing the microfluidic device, and sorted unpredictably, thereby reducing the efficiency of stiffness-based sorting. While the exact prevalence of the clustering effect in the ESC cell system is unknown, retaining a single-cell suspension throughout the sorting process will be paramount to maximizing future cell enrichment efficiencies.

7.5 Single-cell Genomechanics Enables Comparisons of the Mechanical Properties and Gene Expression of Individual Embryonic Stem Cells

A novel method enabling the measurement of single-cell mechanics and gene expression was developed. Importantly, the technique can be easily multiplexed, enabling dozens of genes to be measured for an individual cell and correlated with the cell mechanical properties. The technique successfully identified the expected trend between ESC stiffness and potency, independently of the day of differentiation.

The technique is currently hampered by the difficulty in obtaining large sample numbers. In an average 96-well plate containing 1 cell per raft, AFM and PCR measurements were successfully obtained for only about 2 cells. The primary rate-limiting step is cell immobilization, which is potentially caused by 1) insufficient dispensing resolution of the cell sorter in the row-column plane of the plate, 2) slow or insufficient immobilization of the cell on the Cell-Tak surface, 3) cell dislodgement during washing, or 4) insufficient brightness to recognize cell localization. As the first three causes have either been addressed or are difficult to control, the identification of cells during AFM should be prioritized. Ideally, an automated system would be

developed to help the researcher find the cell based on plate reader images; typically, this step is rate-limiting. Localization via a template matching algorithm has been attempted, but the algorithm is not sufficiently robust to localize the cell using a live image. Specifically, minor changes in focal plane and bright areas, which appear to arise from debris in the fluorescent bead solution, limit the ability to correctly identify the location of the current field of view within the full-well images taken using the imaging plate reader.

The gene expression information obtained for each cell can easily be scaled to 96 genes per cell using Fluidigm technology. Additional information can also be gleaned from cell mechanics by performing force map measurements, rather than individual measurements, on each cell. Using the full z-range of the AFM, force maps over the full height range of ESCs can be recorded. Furthermore, after identifying the contact point using a recently developed algorithm [13], the Young's modulus can be determined as a function of strain [29] and used to generate a force map video in which strain increases over time and color changes indicate localized, strain-dependent Young's moduli.

Additional gene targets for single-cell genomechanics, including genes related to cell cycle, structure, differentiation, and mechanotransduction, are listed in Table 7.1. Further genes of interest related to mechanotransduction are also available in [48]. To complement the PCR-based genomechanics technique, post-AFM biological readouts could be adapted to recent advances in single-cell Western blotting [71] or epigenetics [16]. Western blotting could be targeted at the protein transcripts of the genes listed in Table 7.1, whereas epigenetics studies may be most interesting in the context of LMNA, as discussed in Section 7.4.

Table 7.1: Additional Targets for Single-Cell Genomechanics.

Symbol	Gene	Group	Subgroup
ANAPC2	anaphase promoting complex subunit 2	cell cycle	G2
BCCIP	BRCA2 and CDKN1A interacting protein	cell cycle	G2
CCNB1	cyclin B1	cell cycle	G2
CCNB2	cyclin B2	cell cycle	M
CCNF	cyclin F	cell cycle	M
CDK1	cyclin-dependent kinase 1	cell cycle	M
ABL1	c-abl oncogene 1, non-receptor tyrosine kinase	cell cycle	S
MCM2	minichromosome maintenance deficient 2 mitotin	cell cycle	S
ACTG2	actin, gamma 2	cytoskeleton	actin binding & regulation of actin cytoskeleton
ACTR2	actin related protein 2	cytoskeleton	actin binding & regulation of actin cytoskeleton

Table 7.1 Continued.

Symbol	Gene	Group	Subgroup
ANLN	anillin actin binding protein	cytoskeleton	actin binding & regulation of actin cytoskeleton
FBLIM1	filamin binding LIM protein 1	cytoskeleton	actin binding & regulation of actin cytoskeleton
TWF1	twinfilin	cytoskeleton	actin binding & regulation of actin cytoskeleton
ADD3	adducin 3	cytoskeleton	actin binding & regulation of actin cytoskeleton
GSN	gelsolin	cytoskeleton	actin binding & regulation of actin cytoskeleton
ARPC3	actin related protein 2/3 complex, subunit 3	cytoskeleton	actin binding & regulation of actin cytoskeleton
VIM	vimentin	cytoskeleton	intermediate filaments
MAP1B	microtubule-associated protein 1B	cytoskeleton	microtubules
TUBB3	tubulin beta-3 chain	cytoskeleton	microtubules

Table 7.1 Continued.

Symbol	Gene	Group	Subgroup
CFL2	cofilin-2	cytoskeleton	actin
PFN1	profilin	cytoskeleton	actin
MLYK	myosin light chain kinase	cytoskeleton	myosin
CAV2	caveolin 2	cytoskeleton	actin
RAC1	RAS-related C3 botulinum substrate 1	cytoskeleton	actin
NES	nestin	lineage specification	endoderm/ectoderm
AFP	α-fetaprotein	lineage specification	endoderm/ectoderm
KDR	Flk-1	lineage specification	mesoderm
T	Brachyury T	lineage specification	mesoderm
MAPK1	mitogen-activated protein kinase 1	lineage specification	general
AKT1	thymoma viral proto-oncogene 1	growth	proliferation
BMP1	bone morphogenetic protein 1	growth	proliferation
BMP2	bone morphogenetic protein 2	growth	proliferation
BMP7	bone morphogenetic protein 7	growth	proliferation
TGFB1	transforming growth factor, beta 1	growth	proliferation

Table 7.1 Continued.

Symbol	Gene	Group	Subgroup
YAP1	yes-associated protein 1	mechanotransduction	
TAZ	tafazzin	mechanotransduction	
LMNB1	lamin B1	nucleus	
LMNB2	lamin B2	nucleus	

APPENDIX A

MECHANICAL STIFFNESS AS AN IMPROVED SINGLE-CELL INDICATOR OF OSTEOBLASTIC HUMAN MESENCHYMAL STEM CELL DIFFERENTIATION – SUPPLEMENTAL MATERIAL[1]

A.1 Methods

A.1.1 Antibodies

The primary and secondary antibodies used in flow cytometry immunophenotyping are summarized in Tables A.1, A.2.

Table A.1: Primary Antibodies.

Name	Target	Host Species	Fluorophore	Dilution	Product Number
anti-CD34	Human CD34	Mouse	None (2°Ab)	1:100	Cell Signaling 3569S
anti-CD45	Human CD45	Mouse	None (2°Ab)	1:100	Biolegend 304001
anti-CD73	Human CD73	Mouse	PE	1:100	BD Pharmingen 550257
anti-CD105	Human CD105	Mouse	FITC	1:100	Fitzgerald 61R-CD105dHUFT
anti-CD133	Human CD133	Mouse	PE	1:11	Miltenyi Biotec 130-080-801
anti-CD166	Human CD166	Mouse	PE	1:100	Biolegend 343903
CD166 Isotype	—	Mouse	PE	1:100	Biolegend 400111

[1]Portions of this chapter were reproduced from [19].

Table A.2: Secondary Antibody.

Target	Host Species	Fluorophore	Dilution	Product Number
Mouse IgM/IgG/IgA	Goat	FITC	1:100	Southern Biotech 1010-02

Table A.3: GEO datasets used in the expression analysis. SuperSeries GSE12267, `http://www.ncbi.nlm.nih.gov/geo/`.

Patient #	hMSC	hMSC-OB Day:			hOB
		1	7	10-14	
3002	GSM308067	GSM308068	GSM308069	GSM308070	GSM308030
3080	GSM308071	GSM308072	GSM308073	GSM308074	GSM308034
3205	GSM308075	GSM308076	GSM308077	GSM308078	GSM308037
3206	GSM308079	GSM308080	GSM308081	GSM308082	GSM308041

Table A.4: Original p-Values for Mechanics Data.

		hMSC-OB Day:							hOB
		0	3	6	10	13	17	20	
hMSC-OB Day:	0	—	0.4129	0.0227	0.9954	0.5546	0.0309	0.0033	0.0081
	3		—	0.0648	0.3721	0.7075	0.0820	0.0044	0.0166
	6			—	0.0132	0.0192	0.6311	0.4020	0.7718
	10				—	0.5093	0.0185	0.0013	0.0041
	13					—	0.0124	0.0000	0.0004
	17						—	0.0680	0.2775
	20							—	0.4160
hOB									—

Table A.5: Adjusted p-Values for Mechanics Data.

		hMSC-OB Day:							hOB
		0	3	6	10	13	17	20	
hMSC-OB Day:	0	—	1.0000	0.3632	1.0000	1.0000	0.4635	0.0825	0.1782
	3		—	0.9072	1.0000	1.0000	0.9840	0.1012	0.3154
	6			—	0.2640	0.3330	1.0000	1.0000	1.0000
	10				—	1.0000	0.3330	0.0338	0.0984
	13					—	0.2604	0.0000	0.0108
	17						—	0.9072	1.0000
	20							—	1.0000
hOB									—

Table A.6: Single-Cell Correlation Data.

Variable 1	Variable 2	Spearman's ρ	p original	p adjusted
Area	Day of Differentiation	-0.3323	<0.0001	<0.0091
Area	Young's Modulus	0.3678	<0.0001	<0.0091
Aspect Ratio	Area	-0.1035	0.1217	1
Aspect Ratio	Circularity	-0.5724	<0.0001	<0.0091
Aspect Ratio	Day of Differentiation	0.0844	0.2072	1
Aspect Ratio	Perimeter	0.3236	<0.0001	<0.0091
Aspect Ratio	Young's Modulus	0.1231	0.0652	1
BSP	Area	-0.1601	0.0162	0.5022
BSP	Aspect Ratio	-0.1446	0.0302	0.8456
BSP	Circularity	0.2826	<0.0001	<0.0091
BSP	Day of Differentiation	0.1979	0.0029	0.1073
BSP	Perimeter	-0.2443	0.0002	0.0092
BSP	Roundness	0.1712	0.0101	0.3434
BSP	Young's Modulus	-0.1075	0.1077	1
Circularity	Area	-0.3564	<0.0001	<0.0091
Circularity	Day of Differentiation	0.0988	0.1396	1

Table A.6 Continued.

Variable 1	Variable 2	Spearman's ρ	p original	p adjusted
Circularity	Perimeter	-0.8259	<0.0001	<0.0091
Circularity	Young's Modulus	-0.2765	<0.0001	<0.0091
Eccentricity	Area	0.13	0.0514	1
Eccentricity	Aspect Ratio	-0.9735	<0.0001	<0.0091
Eccentricity	BSP	0.1711	0.0101	0.3434
Eccentricity	Circularity	0.5989	<0.0001	<0.0091
Eccentricity	Day of Differentiation	-0.0735	0.2721	1
Eccentricity	Feret's Diameter	-0.5513	<0.0001	<0.0091
Eccentricity	Major Axis	-0.6614	<0.0001	<0.0091
Eccentricity	Minor Axis	0.7596	<0.0001	<0.0091
Eccentricity	OCN	0.0919	0.1693	1
Eccentricity	Perimeter	-0.297	<0.0001	<0.0091
Eccentricity	Roundness	1	<0.0001	<0.0091
Eccentricity	Young's Modulus	-0.1165	0.0812	1
Feret's Diameter	Area	0.6591	<0.0001	<0.0091
Feret's Diameter	Aspect Ratio	0.5779	<0.0001	<0.0091
Feret's Diameter	BSP	-0.2461	0.0002	0.0092
Feret's Diameter	Circularity	-0.7723	<0.0001	<0.0091
Feret's Diameter	Day of Differentiation	-0.1656	0.0129	0.4128
Feret's Diameter	Major Axis	0.9436	<0.0001	<0.0091
Feret's Diameter	Minor Axis	0.0393	0.5577	1
Feret's Diameter	OCN	-0.1006	0.1323	1
Feret's Diameter	Perimeter	0.8818	<0.0001	<0.0091
Feret's Diameter	Roundness	-0.5513	<0.0001	<0.0091

Table A.6 Continued.

Variable 1	Variable 2	Spearman's ρ	p original	p adjusted
Feret's Diameter	Young's Modulus	0.3911	<0.0001	<0.0091
Major Axis	Area	0.6142	<0.0001	<0.0091
Major Axis	Aspect Ratio	0.6879	<0.0001	<0.0091
Major Axis	BSP	-0.2272	0.0006	0.0258
Major Axis	Circularity	-0.7261	<0.0001	<0.0091
Major Axis	Day of Differentiation	-0.1443	0.0305	0.8456
Major Axis	OCN	-0.1154	0.0841	1
Major Axis	Perimeter	0.8277	<0.0001	<0.0091
Major Axis	Roundness	-0.6614	<0.0001	<0.0091
Major Axis	Young's Modulus	0.3853	<0.0001	<0.0091
Minor Axis	Area	0.7253	<0.0001	<0.0091
Minor Axis	Aspect Ratio	-0.7331	<0.0001	<0.0091
Minor Axis	BSP	0.0259	0.699	1
Minor Axis	Circularity	0.1721	0.0097	0.3395
Minor Axis	Day of Differentiation	-0.2716	<0.0001	<0.0091
Minor Axis	Major Axis	-0.0629	0.3474	1
Minor Axis	OCN	-0.0134	0.8421	1
Minor Axis	Perimeter	0.3006	<0.0001	<0.0091
Minor Axis	Roundness	0.7596	<0.0001	<0.0091
Minor Axis	Young's Modulus	0.1462	0.0284	0.8236
OCN	Area	-0.1104	0.0987	1
OCN	Aspect Ratio	-0.0654	0.3288	1
OCN	BSP	0.6596	<0.0001	<0.0091
OCN	Circularity	0.1986	0.0028	0.1064

Table A.6 Continued.

Variable 1	Variable 2	Spearman's ρ	p original	p adjusted
OCN	Day of Differentiation	0.1812	0.0064	0.2304
OCN	Perimeter	-0.1541	0.0208	0.624
OCN	Roundness	0.0919	0.1694	1
OCN	Young's Modulus	-0.1382	0.0384	0.96
Perimeter	Area	0.7951	<0.0001	<0.0091
Perimeter	Day of Differentiation	-0.2377	0.0003	0.0132
Perimeter	Young's Modulus	0.3869	<0.0001	<0.0091
Perimeter:Area	Area	-0.4397	<0.0001	<0.0091
Perimeter:Area	Aspect Ratio	0.6646	<0.0001	<0.0091
Perimeter:Area	BSP	-0.1075	0.1077	1
Perimeter:Area	Circularity	-0.5901	<0.0001	<0.0091
Perimeter:Area	Day of Differentiation	0.2097	0.0016	0.064
Perimeter:Area	Eccentricity	-0.638	<0.0001	<0.0091
Perimeter:Area	Feret's Diameter	0.2126	0.0013	0.0546
Perimeter:Area	Major Axis	0.2061	0.0019	0.0741
Perimeter:Area	Minor Axis	-0.7316	<0.0001	<0.0091
Perimeter:Area	OCN	-0.0705	0.2922	1
Perimeter:Area	Perimeter	0.1433	0.0316	0.8456
Perimeter:Area	Roundness	-0.638	<0.0001	<0.0091
Perimeter:Area	Young's Modulus	-0.0218	0.745	1
Roundness	Area	0.13	0.0515	1
Roundness	Aspect Ratio	-0.9735	<0.0001	<0.0091
Roundness	Circularity	0.5989	<0.0001	<0.0091
Roundness	Day of Differentiation	-0.0735	0.2723	1

Table A.6 Continued.

Variable 1	Variable 2	Spearman's ρ	p original	p adjusted
Roundness	Perimeter	-0.297	<0.0001	<0.0091
Roundness	Young's Modulus	-0.1165	0.0813	1
Young's Modulus	Day of Differentiation	-0.2136	0.0013	0.0546

Table A.7: Cell Population Correlation Data.

Variable 1	Variable 2	Spearman's ρ	p original	p adjusted
BSP	Day of Differentiation	0.5139	<0.0001	<0.0003
OCN	Day of Differentiation	0.5195	<0.0001	<0.0003
OCN	BSP	0.8921	<0.0001	<0.0003

Table A.8: Single-Cell Correlation Data (Readjusted).

Variable 1	Variable 2	Spearman's ρ	p original	p adjusted
OCN	BSP	0.6596	<0.0001	<0.0003
BSP	Day of Differentiation	0.1979	0.0029	0.0058
OCN	Day of Differentiation	0.1812	0.0064	0.0064

Table A.9: GO cellular component gene sets enriched in hMSC phenotype based on Gene Set Enrichment Analysis (GSEA). Size, number of genes in each gene set that appeared in the dataset; ES, enrichment score; NES, normalized enrichment score; p, nominal p-value for the statistical significance of the enrichment score; FDR q, FDR-adjusted p-value.

Name	Size	ES	NES	p	FDR q
CHROMOSOME	114	-0.64684	-2.39457	0	0
CHROMOSOME PERICEN-TRIC REGION	27	-0.8331	-2.38101	0	0
CHROMOSOMAL PART	88	-0.67821	-2.37618	0	0
SPINDLE	37	-0.77124	-2.33851	0	0

Table A.9 Continued.

Name	Size	ES	NES	p	FDR q
KINETOCHORE	22	-0.80783	-2.19197	0	0
SPINDLE MICROTUBULE	15	-0.8572	-2.15332	0	0
MICROTUBULE CYTOSKELETON	136	-0.53713	-2.01797	0	0.000349
CONDENSED CHROMOSOME	29	-0.68079	-2.01764	0	0.000306
MICROTUBULE ORGANIZING CENTER	57	-0.6142	-2.01263	0	0.000393
CENTROSOME	49	-0.61732	-1.95472	0	0.001652
REPLICATION FORK	17	-0.77228	-1.94433	0	0.001608
MICROTUBULE	31	-0.66056	-1.9215	0	0.002273
SPINDLE POLE	17	-0.75592	-1.89858	0.001901	0.002803
CONDENSED NUCLEAR CHROMOSOME	16	-0.74319	-1.88456	0	0.002767
NUCLEAR CHROMOSOME	50	-0.58816	-1.86942	0	0.00328
CHROMATIN	34	-0.62182	-1.84537	0	0.004664
CYTOSKELETAL PART	215	-0.45521	-1.80533	0	0.008715
CYTOSKELETON	336	-0.41317	-1.73251	0	0.02014
LEADING EDGE	41	-0.56125	-1.7241	0.005102	0.021379
NUCLEAR CHROMOSOME PART	31	-0.58063	-1.693	0.010084	0.027808

Table A.10: GeneGO Maps significantly associated with 4,396 features differentially expressed between hMSCs and hOBs at FDR<0.01.. p, hypergeometric p-value (probability that the enrichment of the differentially expressed genes was obtained purely by chance); FDR q, FDR-adjusted p-value; N1, number of identifiers among differentially expressed features; N2, total number of identifiers.

Rank	Maps	p	FDR q	N1	N2
1	Cell cycle_The metaphase checkpoint	1.34E-13	9.40E-11	22	36
2	Cell cycle_Start of DNA replication in early S phase	9.68E-13	3.39E-10	20	32
3	DNA damage_ATM / ATR regulation of G2 / M checkpoint	1.77E-11	4.13E-09	17	26
4	Cell cycle_Chromosome condensation in prometaphase	7.81E-10	1.37E-07	14	21
5	Cell cycle_Role of APC in cell cycle regulation	1.76E-09	2.46E-07	17	32
6	Cell cycle_Spindle assembly and chromosome separation	3.28E-09	3.83E-07	17	33
7	Reproduction_Progesterone-mediated oocyte maturation	1.76E-08	1.76E-06	18	40
8	Transcription_Role of Akt in hypoxia induced HIF1 activation	7.44E-08	6.51E-06	14	27
9	Cell cycle_Regulation of G1/S transition (part 1)	3.42E-07	2.66E-05	16	38
10	G-protein signaling_RhoA regulation pathway	3.83E-07	2.68E-05	15	34
11	Cytoskeleton remodeling_TGF, WNT and cytoskeletal remodeling	4.60E-07	2.93E-05	30	111

Table A.10 Continued.

Rank	Maps	p	FDR q	N1	N2
12	Cell adhesion_Chemokines and adhesion	5.04E-07	2.94E-05	28	100
13	Cytoskeleton remodeling_Cytoskeleton remodeling	7.85E-07	4.23E-05	28	102
14	Development_TGF-beta receptor signaling	1.03E-06	4.98E-05	18	50
15	DNA damage_ATM/ATR regulation of G1/S checkpoint	1.07E-06	4.98E-05	14	32
16	Immune response_Oncostatin M signaling via MAPK in human cells	1.44E-06	6.28E-05	15	37
17	Cell cycle_Initiation of mitosis	1.90E-06	7.81E-05	12	25
18	Translation_Regulation of EIF4F activity	2.74E-06	1.07E-04	18	53
19	Signal transduction_PKA signaling	6.92E-06	2.55E-04	17	51
20	Apoptosis and survival_BAD phosphorylation	9.23E-06	3.08E-04	15	42
21	Immune response_PIP3 signaling in B lymphocytes	9.23E-06	3.08E-04	15	42
22	Development_BMP signaling	1.06E-05	3.37E-04	13	33
23	Immune response_HMGB1/RAGE signaling pathway	1.24E-05	3.78E-04	17	53
24	Cell cycle_Cell cycle (generic schema)	1.54E-05	4.48E-04	10	21
25	Development_Thromboxane A2 pathway signaling	1.73E-05	4.85E-04	16	49

Table A.10 Continued.

Rank	Maps	p	FDR q	N1	N2
26	Cell cycle_Nucleocytoplasmic transport of CDK/Cyclins	2.07E-05	5.56E-04	8	14
27	Immune response_Oncostatin M signaling via MAPK in mouse cells	2.25E-05	5.82E-04	13	35
28	Cell cycle_Role of 14-3-3 proteins in cell cycle regulation	2.56E-05	6.40E-04	10	22
29	Immune response_MIF-induced cell adhesion, migration and angiogenesis	3.23E-05	7.79E-04	15	46
30	Development_IGF-1 receptor signaling	3.99E-05	9.30E-04	16	52
31	Development_WNT signaling pathway. Part 1. Degradation of beta-catenin in the absence WNT signaling	4.39E-05	9.92E-04	9	19
32	Development_WNT signaling pathway. Part 2	5.17E-05	1.12E-03	16	53
33	Cell cycle_Transition and termination of DNA replication	5.28E-05	1.12E-03	11	28
34	Immune response_Antigen presentation by MHC class II	5.91E-05	1.20E-03	7	12
35	Signal transduction_AKT signaling	6.01E-05	1.20E-03	14	43
36	Immune response_Role of integrins in NK cells cytotoxicity	6.14E-05	1.20E-03	13	38
37	Development_Glucocorticoid receptor signaling	6.41E-05	1.21E-03	10	24
38	Immune response_BCR pathway	6.66E-05	1.22E-03	16	54

Table A.10 Continued.

Rank	Maps	p	FDR q	N1	N2
39	Immune response_Oncostatin M signaling via JAK-Stat in human cells	7.26E-05	1.30E-03	9	20
40	Development_VEGF signaling via VEGFR2 - generic cascades	8.44E-05	1.45E-03	21	84
41	Immune response_Fc epsilon RI pathway	8.51E-05	1.45E-03	16	55
42	Development_c-Kit ligand signaling pathway during hemopoiesis	9.34E-05	1.56E-03	17	61
43	Transcription_Transcription regulation of aminoacid metabolism	9.70E-05	1.58E-03	10	25
44	Development_Thrombopoietin-regulated cell processes	1.05E-04	1.67E-03	14	45
45	DNA damage_Role of Brca1 and Brca2 in DNA repair	1.11E-04	1.72E-03	11	30
46	Cell adhesion_Plasmin signaling	1.15E-04	1.75E-03	12	35
47	Cell adhesion_ECM remodeling	1.57E-04	2.33E-03	15	52
48	Regulation of CFTR activity (norm and CF)	1.70E-04	2.48E-03	16	58
49	Development_Growth hormone signaling via PI3K/AKT and MAPK cascades	1.96E-04	2.8E-03	13	42
50	Possible pathway of TGF-beta 1-dependent inhibition of CFTR expression	2.07E-04	2.85E-03	10	27

Table A.10 Continued.

Rank	Maps	p	FDR q	N1	N2
51	Immune response_TREM1 signaling pathway	2.12E-04	2.85E-03	16	59
52	Immune response_Immunological synapse formation	2.12E-04	2.85E-03	16	59
53	Cell cycle_Role of Nek in cell cycle regulation	2.16E-04	2.85E-03	11	32
54	Immune response_HTR2A-induced activation of cPLA2	2.55E-04	3.30E-03	13	43
55	Immune response_IL-4 signaling pathway	3.28E-04	4.18E-03	13	44
56	Immune response_Histamine signaling in dendritic cells	3.63E-04	4.34E-03	14	50
57	Immune response_C5a signaling	3.63E-04	4.34E-03	14	50
58	HIV-1 signaling via CCR5 in macrophages and T lymphocytes	3.66E-04	4.34E-03	12	39
59	Transcription_P53 signaling pathway	3.66E-04	4.34E-03	12	39
60	Development_Keratinocyte differentiation	3.84E-04	4.47E-03	15	56
61	Proteolysis_Putative SUMO-1 pathway	4.05E-04	4.58E-03	10	29
62	Transcription_Androgen Receptor nuclear signaling	4.19E-04	4.58E-03	13	45
63	Development_Ligand-independent activation of ESR1 and ESR2	4.19E-04	4.58E-03	13	45

Table A.10 Continued.

Rank	Maps	p	FDR q	N1	N2
64	Cell adhesion_Ephrin signaling	4.19E-04	4.58E-03	13	45
65	Immune response_NFAT in immune response	4.535E-04	4.88E-03	14	51
66	Immune response_Fc gamma R-mediated phagocytosis in macrophages	5.30E-04	5.45E-03	13	46
67	Development_Hedgehog signaling	5.30E-04	5.45E-03	13	46
68	Signal transduction_PTEN pathway	5.30E-04	5.45E-03	13	46
69	Immune response _Sialic-acid receptors (Siglecs) signaling	6.22E-04	6.31E-03	6	12
70	Development_PIP3 signaling in cardiac myocytes	6.65E-04	6.34E-03	13	47
71	Transport_Clathrin-coated vesicle cycle	6.72E-04	6.39E-03	17	71
72	Immune response_Regulation of T cell function by CTLA-4	6.83E-04	6.39E-03	11	36
73	G-protein signaling_Regulation of RAC1 activity	6.83E-04	6.39E-03	11	36
74	Immune response_CD40 signaling	6.93E-04	6.39E-03	16	65
75	Apoptosis and survival_Endoplasmic reticulum stress response pathway	6.94E-04	6.39E-03	14	53
76	Development_Endothelin-1/EDNRA signaling	6.94E-04	6.39E-03	14	53
77	Immune response_IL-18 signaling	8.49E-04	7.63E-03	15	60

Table A.10 Continued.

Rank	Maps	p	FDR q	N1	N2
78	Immune response_HSP60 and HSP70/ TLR signaling pathway	8.50E-04	7.63E-03	14	54
79	DNA damage_DNA-damage-induced responses	1.01E-03	8.81E-03	5	9
80	Development_Melanocyte development and pigmentation	1.02E-03	8.81E-03	13	49
81	Development_A3 receptor signaling	1.02E-03	8.81E-03	13	49
82	Immune response_MIF-mediated glucocorticoid regulation	1.04E-03	8.81E-03	8	22
83	Translation_Regulation of translation initiation	1.04E-03	8.81E-03	9	27

Table A.11: GeneGO Process Networks. GeneGO Process Networks significantly associated with 4,396 features differentially expressed between hMSCs and hOBs at FDR<0.04. p, hypergeometric p-value (probability that the enrichment of the differentially expressed genes was obtained purely by chance); FDR q, FDR-adjusted p-value; N1, number of identifiers among differentially expressed features; N2, total number of identifiers.

Rank	Process Networks	p	FDR q	N1	N2
1	Cell cycle_Core	5.45E-15	8.66E-13	58	114
2	Cell cycle_S phase	7.58E-12	6.03E-10	63	147
3	Cell cycle_G2-M	1.86E-09	9.86E-08	74	205
4	Cell cycle_Mitosis	3.15E-09	1.25E-07	66	177
5	Cytoskeleton_Spindle microtubules	2.21E-07	7.02E-06	43	108
6	Immune response_BCR pathway	1.97E-05	5.22E-04	43	125
7	Signal transduction_WNT signaling	2.50E-05	5.67E-04	54	170

Table A.11 Continued.

Rank	Process Networks	p	FDR q	N1	N2
8	Reproduction_Progesterone signaling	6.45E-05	1.28E-03	58	192
9	Translation_Regulation of initiation	3.40E-04	6.01E-03	39	123
10	DNA damage_Checkpoint	8.45E-04	1.34E-02	38	124
11	Signal Transduction_Cholecystokinin signaling	1.17E-03	1.69E-02	30	93
12	Reproduction_FSH-beta signaling pathway	1.29E-03	1.70E-02	44	152
13	Development_Ossification and bone remodeling	1.49E-03	1.82E-02	44	153
14	Cell cycle_G1-S	1.79E-03	1.98E-02	46	163
15	DNA damage_DBS repair	1.91E-03	1.98E-02	33	108
16	Immune response_Phagocytosis	2.10E-03	1.98E-02	53	195
17	Inflammation_Histamine signaling	2.12E-03	1.98E-02	48	173
18	Development_Blood vessel morphogenesis	3.18E-03	2.81E-02	56	212
19	Inflammation_TREM1 signaling	3.75E-03	3.01E-02	36	125
20	Inflammation_IL-4 signaling	3.79E-03	3.01E-02	32	108
21	Cell adhesion_Platelet aggregation	4.98E-03	3.77E-02	36	127

A.1.2 Flow cytometry immunophenotyping

Cells were fixed with 4% (w:v) paraformaldehyde for 15 min, washed with PBS, and stored in PBS at 4°C. Cells were permeabilized by incubation with 0.5% Triton X-100 in sterile H_2O for 30 min at 4°C, with resupension by vortexing every 15 min. Cells were then washed in working buffer solution (WBS, 3 mg/mL bovine serum albumin and 1% Tween-20 in sterile PBS, sterile filtered) and incubated with WBS containing

10% normal goat serum for 1 h at 4°C, with resupension by vortexing every 15 min. Cells were washed with WBS and incubated in primary antibody solution for 30 min at 4°C. Cells were washed with WBS and incubated in WBS or secondary antibody solution (where applicable) for 30 min at 4°C. Cells were washed twice in WBS before data were taken on an Accuri C6 flow cytometer (Becton Dickinson, Franklin Lakes, NJ). Samples were run in triplicate, with at least 10,000 FSC/SSC-gated events per sample. Data were analyzed using FlowJo software (TreeStar, Ashland, OR).

A.1.3 Donor test

Additional hMSCs at passage 1 were obtained from the Tulane University Center for Gene Therapy (Donor 7071L) and grown similarly to the hMSCs from Texas A&M. The stiffnesses of hMSCs from each donor were compared at passage 4 using Student's independent t-test (α=0.05).

A.1.4 Single-cell immunofluorescence

Cells were washed twice with PBS and fixed with 4% (w:v) paraformaldehyde for 30 min at room temperature. Cells were then washed twice with PBS and once with wash buffer (1 mg/mL bovine serum albumin in PBS). Cells were permeabilized by incubation with 0.5% Triton X-100 in sterile H_2O for 30 min and blocked by incubation with 10% normal goat serum and 0.3% Triton X-100 in PBS for 45 min. Cells were incubated with 1:500 rabbit anti-human BSP (ab52128, Abcam, Cambridge, MA) and 1:15 phycoerythrin (PE)-conjugated mouse anti-human OCN (IC1419P, R&D Systems, Minneapolis, MN) in dilution buffer (10 mg/mL bovine serum albumin, 1% normal goat serum, 0.3% Triton X, 0.1 mg/mL sodium azide in PBS) for 12 h at 4°C, washed twice with wash buffer, incubated in 1:100 fluorescein isothiocyanate (FITC)-conjugated goat anti-rabbit IgG (Abcam ab97068) in dilution buffer for 1 h, and washed twice with wash buffer. Cell membranes were then stained with HCS CellMask Blue (H32720, Invitrogen, Carlsbad, CA, 1:10,000 in PBS) for 30

min. Following two washes in PBS, cells were mounted in anti-fade reagent (100 mM N-propyl gallate in 1:1 [v:v] PBS:glycerol) and sealed under a 22 mm glass coverslip with clear nail polish. Gridded Petri dishes were inverted prior to imaging on an inverted microscope in order to image the cells through a single glass coverslip.

A.1.5 Gene expression analysis

Raw gene expression data for naive hMSCs, Day 1, 7, or 10-14 hMSC-OBs, and hOBs [62] were downloaded as Affymetrix (Santa Clara, CA) Human Genome U133 Plus 2.0 .CEL files from the gene expression omnibus (GEO) dataset GSE 12267 (`http://www.ncbi.nlm.nih.gov/geo/`). Data for 4 patients (3002, 3080, 3205, 3206) were analyzed as biological replicates (Table A.3). Quality of raw data was evaluated and the data were GCRMA-normalized using the Arrayanalysis.org tool [45]. Normalized expression data were analyzed by differential expression analysis (DEA) and gene set enrichment analysis (GSEA). DEA was performed using the significance analysis of microarrays (SAM) method [150] as (1) paired analysis to identify genes with significant differences in gene expression between hMSCs and hOBs and (2) one class time course analysis to identify genes with consistent increase or decrease in expression during hMSCs osteoblastic differentiation. In DEA, probe sets with absent calls (detected by MAS5 algorithm) across all specimens were removed and GCRMA-normalized signals for remaining probe sets were analyzed by SAM as paired data (hMSCs vs. hOBs) or as time series data using slope summarization. Features identified as differentially expressed were biologically interpreted via their functional enrichment in GeneGO Maps and GeneGO Process Networks using MetaCore version 6.15 build 62452 integrated software suite (GeneGO, Thomson Reuters, Philadelphia, PA) [15]. GSEA analysis [135] was performed on GCRMA-normalized data without any pre-filtering of probe sets for hMSCs vs. hOBs using categorical phenotype labels and signal-to-noise metrics to identify gene sets significantly enriched in specific

phenotypes. Gene set permutation type and C5 GO gene sets (Molecular Signatures Database v4.0; 1454 gene sets) were the parameters were used in this GSEA. Gene sets with q<0.05 were considered to be significantly enriched in a given phenotype.

A.1.6 Statistics

Original p-values and Holm's adjusted p-values determined from the bootstrapping post-hoc analysis of AFM data are listed in Tables A.4, A.5, respectively. Spearman's rank correlation coefficients, original p-values, and Holm's adjusted p-values for single-cells and cell populations are listed in Tables A.6, A.7, respectively. To facilitate comparison to the cell population data, Holm's adjustment was recalculated for the single-cell data using N=3 (Fig. 5C); the recalculated Holm's adjusted p-values are listed in Table A.8.

A.2 Results

A.2.1 Flow cytometry immunophenotyping

Fluorescence intensity histograms were gated to indicate the percentage of putative hMSCs positive for the indicated antibody compared to each negative control. Relative to secondary antibody only control, hMSCs were negative for CD34 and CD45 (Fig. S1A-B). Relative to unlabeled cells, hMSCs were negative for CD133 and positive for CD73 and CD105 (Fig. S1C-E). Relative to isotype control, hMSCs were positive for CD166 (Fig. S1F). Putative hMSCs were therefore CD34-, CD45-, CD133-, CD73+, CD105+, and CD166+, indicating MSC phenotype.

A.2.2 Image processing validation

The aspect ratio can be written as the inverse of roundness or, assuming a perfect ellipse, $\frac{1}{\sqrt{e^2-1}}$, where e is the eccentricity. For a perfect eclipse, e is related to the roundness, r, by $e = \sqrt{1+r^2}$. Therefore, the aspect ratio was perfectly inversely related (Spearman's ρ=-1) to both roundness and eccentricity, and e was perfectly

directly related to r (Spearman's ρ=+1).

The major axis is the primary axis of the best fitting ellipse, and Feret's diameter is the largest distance between any two points on the cell boundary. Therefore, generally elliptical morphologies are likely to have a Feret's diameter similar to the major axis, and a strong positive relationship was observed (Table A.6). The perimeter:area ratio is equivalent to $\frac{4\pi}{c \cdot p}$, where c is circularity and p is perimeter. The perimeter:area ratio was therefore strongly inversely related to circularity. Circularity, which can be written as $\frac{4\pi \cdot A}{p^2}$, is more strongly dependent on perimeter, p, than area, A; therefore, a strong inverse relationship between circularity and perimeter was observed.

A.2.3 Gene expression

GSEA revealed that relative to hOBs, hMSCs were enriched for 20 GO cellular component gene sets, including Chromosome, Chromatin, Cytoskeletal Part, and Cytoskeleton (Table A.9). Within the Cytoskeleton set, 70 genes comprised a leading-edge subset that contributed most to the Cytoskeleton gene set enrichment (Supplementary Excel Sheet 4). 12 of the leading-edge subset genes mapped to the Actin Cytoskeleton Organization GO term, 6 to Regulation of Actin Filament Polymerization or Depolymerization, and 5 to Actin Filament Capping.

DEA identified 4,396 differentially expressed Affymetrix features between hMSCs and hOBs ($|FC| \geq 1.5$; FDR=4.77%), of which 2,367 probe sets showed increased expression and 2,029 showed decreased expression in hOBs relative to hMSCs (Supplementary Excel Sheet 2). The differentially expressed features were enriched in 83 GeneGO Maps at FDR=1% (Table A.10) and 21 GeneGO Process Networks at FDR=3.77% (Table A.11), which are related to the cell cycle, DNA replication, and DNA repair.

REFERENCES

[1] Agrelo, R., Setien, F., Espada, J., Artiga, M. J., Rodriguez, M., Pérez-Rosado, A., Sanchez-Aguilera, A., Fraga, M. F., Piris, M. A., and Esteller, M., "Inactivation of the lamin A/C gene by CpG island promoter hypermethylation in hematologic malignancies, and its association with poor survival in nodal diffuse large B-cell lymphoma.," *Journal of clinical oncology : official journal of the American Society of Clinical Oncology*, vol. 23, pp. 3940–3947, June 2005.

[2] Ahmad, S., "Concise review: limbal stem cell deficiency, dysfunction, and distress.," *Stem cells translational medicine*, vol. 1, pp. 110–115, Feb. 2012.

[3] Ahmad, S., Kolli, S., Li, D.-Q., de Paiva, C. S., Pryzborski, S., Dimmick, I., Armstrong, L., Figueiredo, F. C., and Lako, M., "A putative role for RHAMM/HMMR as a negative marker of stem cell-containing population of human limbal epithelial cells.," *Stem Cells*, vol. 26, pp. 1609–1619, June 2008.

[4] Amini, A. R., Laurencin, C. T., and Nukavarapu, S. P., "Bone tissue engineering: recent advances and challenges.," *Critical reviews in biomedical engineering*, vol. 40, no. 5, pp. 363–408, 2012.

[5] Arpitha, P., Prajna, N. V., Srinivasan, M., and Muthukkaruppan, V., "High expression of p63 combined with a large N/C ratio defines a subset of human limbal epithelial cells: implications on epithelial stem cells.," *Investigative ophthalmology & visual science*, vol. 46, pp. 3631–3636, Oct. 2005.

[6] Aubin, J. E. and Triffitt, J., "Mesenchymal stem cells and osteoblast differentiation," in *Principles of Bone Biology*, pp. 59–81, San Diego: Academic Press, 2002.

[7] Baksh, D., Song, L., and Tuan, R. S., "Adult mesenchymal stem cells: characterization, differentiation, and application in cell and gene therapy.," *Journal of Cellular and Molecular Medicine*, vol. 8, pp. 301–316, June 2004.

[8] Baraniak, P. R., Cooke, M. T., Saeed, R., Kinney, M. A., Fridley, K. M., and McDevitt, T. C., "Stiffening of human mesenchymal stem cell spheroid microenvironments induced by incorporation of gelatin microparticles.," *Journal of the mechanical behavior of biomedical materials*, vol. 11, pp. 63–71, July 2012.

[9] Baraniak, P. R. and McDevitt, T. C., "Stem cell paracrine actions and tissue regeneration.," *Regenerative medicine*, vol. 5, pp. 121–143, Jan. 2010.

[10] Barrandon, Y. and Green, H., "Three clonal types of keratinocyte with different capacities for multiplication.," *Proceedings of the National Academy of Sciences*, vol. 84, pp. 2302–2306, Apr. 1987.

[11] Battula, V. L., Treml, S., Bareiss, P. M., Gieseke, F., Roelofs, H., de Zwart, P., Müller, I., Schewe, B., Skutella, T., Fibbe, W. E., Kanz, L., and Bühring, H.-J. J., "Isolation of functionally distinct mesenchymal stem cell subsets using antibodies against CD56, CD271, and mesenchymal stem cell antigen-1.," *Haematologica*, vol. 94, pp. 173–184, Feb. 2009.

[12] Ben-David, U., Kopper, O., and Benvenisty, N., "Expanding the boundaries of embryonic stem cells.," *Cell stem cell*, vol. 10, pp. 666–677, June 2012.

[13] BenÍtez, R., Moreno-flores, S., BolÓs, V. J., and Toca-Herrera, J. L., "A new automatic contact point detection algorithm for AFM force curves.," *Microscopy research and technique*, vol. 76, pp. 870–876, Aug. 2013.

[14] Bernstein, H. S. and Hyun, W. C., "Strategies for enrichment and selection of stem cell-derived tissue precursors.," *Stem cell research & therapy*, vol. 3, no. 3, p. 17, 2012.

[15] Bessarabova, M., Ishkin, A., JeBailey, L., Nikolskaya, T., and Nikolsky, Y., "Knowledge-based analysis of proteomics data.," *BMC bioinformatics*, vol. 13 Suppl 16, p. S13, 2012.

[16] Bheda, P., Bheda, P., Schneider, R., and Schneider, R., "Epigenetics reloaded: the single-cell revolution.," *Trends in cell biology*, vol. 24, pp. 712–723, Nov. 2014.

[17] Binnig, G., Quate, C., and Gerber, C., "Atomic force microscope.," *Physical Review Letters*, vol. 56, pp. 930–933, Mar. 1986.

[18] Bongiorno, T., Chojnowski, J. L., Lauderdale, J. D., and Sulchek, T., "Cellular Stiffness as a Novel Stemness Marker in the Corneal Limbus.," *Biophysical Journal*, vol. 111, pp. 1761–1772, Oct. 2016.

[19] Bongiorno, T., Kazlow, J., Mezencev, R., Griffiths, S., Olivares-Navarrete, R., McDonald, J. F., Schwartz, Z., Boyan, B. D., McDevitt, T. C., and Sulchek, T., "Mechanical stiffness as an improved single-cell indicator of osteoblastic human mesenchymal stem cell differentiation.," *Journal of Biomechanics*, vol. 47, pp. 2197–2204, June 2014.

[20] Boraas, L. C., Guidry, J. B., Pineda, E. T., and Ahsan, T., "Cytoskeletal Expression and Remodeling in Pluripotent Stem Cells.," *PLoS ONE*, vol. 11, no. 1, p. e0145084, 2016.

[21] Carpenter, A. E., Jones, T. R., Lamprecht, M. R., Clarke, C., Kang, I. H., Friman, O., Guertin, D. A., Chang, J. H., Lindquist,

R. A., Moffat, J., Golland, P., and Sabatini, D. M., "CellProfiler: image analysis software for identifying and quantifying cell phenotypes.," *Genome biology*, vol. 7, no. 10, p. R100, 2006.

[22] Chan, L. Y., Birch, W. R., Yim, E. K. F., and Choo, A. B. H., "Temporal application of topography to increase the rate of neural differentiation from human pluripotent stem cells.," *Biomaterials*, vol. 34, pp. 382–392, Jan. 2013.

[23] Chen, B., Jones, R. R., Mi, S., Foster, J., and Alcock, S. G., "The mechanical properties of amniotic membrane influence its effect as a biomaterial for ocular surface repair," *Soft Matter*, vol. 8, pp. 8379–8387, 2012.

[24] Chen, Q., Xiao, P., Chen, J.-N., Cai, J.-Y., Cai, X.-F., Ding, H., and Pan, Y.-L., "AFM studies of cellular mechanics during osteogenic differentiation of human amniotic fluid-derived stem cells.," *Analytical sciences*, vol. 26, no. 10, pp. 1033–1037, 2010.

[25] Chen, W., Zhou, H., Weir, M. D., Tang, M., Bao, C., and Xu, H. H. K., "Human embryonic stem cell-derived mesenchymal stem cell seeding on calcium phosphate cement-chitosan-RGD scaffold for bone repair.," *Tissue Engineering Part A*, vol. 19, pp. 915–927, Apr. 2013.

[26] Chen, Z., de Paiva, C. S., Luo, L., Kretzer, F. L., Pflugfelder, S. C., and Li, D.-Q., "Characterization of putative stem cell phenotype in human limbal epithelia.," *Stem Cells*, vol. 22, no. 3, pp. 355–366, 2004.

[27] Chistiakov, D. A. and Chistiakov, P. A., "Strategies to produce hepatocytes and hepatocyte-like cells from pluripotent stem cells.," *Hepatology research : the official journal of the Japan Society of Hepatology*, vol. 42, pp. 111–119, Feb. 2012.

[28] Constantinescu, D., Gray, H. L., Sammak, P. J., Schatten, G. P., and Csoka, A. B., "Lamin A/C expression is a marker of mouse and human embryonic stem cell differentiation.," *Stem Cells*, vol. 24, pp. 177–185, Jan. 2006.

[29] Costa, K. D., Sim, A. J., and Yin, F. C.-P., "Non-Hertzian approach to analyzing mechanical properties of endothelial cells probed by atomic force microscopy.," *Journal of biomechanical engineering*, vol. 128, pp. 176–184, Apr. 2006.

[30] Cregger, M., Berger, A. J., and Rimm, D. L., "Immunohistochemistry and quantitative analysis of protein expression.," *Archives of pathology & laboratory medicine*, vol. 130, pp. 1026–1030, July 2006.

[31] Cross, S. E., Jin, Y.-S., Rao, J., and Gimzewski, J. K., "Nanomechanical analysis of cells from cancer patients.," *Nature nanotechnology*, vol. 2, pp. 780–783, Dec. 2007.

[32] Cross, S. E., Jin, Y.-S., Tondre, J., Wong, R., Rao, J., and Gimzewski, J. K., "AFM-based analysis of human metastatic cancer cells.," *Nanotechnology*, vol. 19, p. 384003, Sept. 2008.

[33] D'Angelo, F., Tiribuzi, R., Armentano, I., Kenny, J. M., Martino, S., and Orlacchio, A., "Mechanotransduction: Tuning Stem Cells Fate," *Journal of Functional Biomaterials*, vol. 2, no. 2, pp. 67–87, 2011.

[34] Darling, E. M., Topel, M., Zauscher, S., Vail, T. P., and Guilak, F., "Viscoelastic properties of human mesenchymally-derived stem cells and primary osteoblasts, chondrocytes, and adipocytes.," *Journal of Biomechanics*, vol. 41, no. 2, pp. 454–464, 2008.

[35] Darling, E. M., Zauscher, S., Block, J. A., and Guilak, F., "A thin-layer model for viscoelastic, stress-relaxation testing of cells using atomic force microscopy: do cell properties reflect metastatic potential?," *Biophysical Journal*, vol. 92, pp. 1784–1791, Mar. 2007.

[36] Deonarain, M. P., Kousparou, C. A., and Epenetos, A. A., "Antibodies targeting cancer stem cells: a new paradigm in immunotherapy?," *MAbs*, vol. 1, no. 1, pp. 12–25, 2009.

[37] Desai, H. V., Voruganti, I. S., Jayasuriya, C., Chen, Q., and Darling, E. M., "Live-cell, temporal gene expression analysis of osteogenic differentiation in adipose-derived stem cells.," *Tissue Engineering Part A*, vol. 19, pp. 40–48, Jan. 2013.

[38] Di Carlo, D., Tse, H. T. K., and Gossett, D. R., "Introduction: why analyze single cells?," *Methods in molecular biology (Clifton, N.J.)*, vol. 853, pp. 1–10, 2012.

[39] Diogo, M. M., da Silva, C. L., and Cabral, J. M. S., "Separation technologies for stem cell bioprocessing.," *Biotechnology and bioengineering*, vol. 109, pp. 2699–2709, Nov. 2012.

[40] Docheva, D., Padula, D., Popov, C., Mutschler, W., Clausen-Schaumann, H., and Schieker, M., "Researching into the cellular shape, volume and elasticity of mesenchymal stem cells, osteoblasts and osteosarcoma cells by atomic force microscopy.," *Journal of Cellular and Molecular Medicine*, vol. 12, pp. 537–552, Apr. 2008.

[41] Dominici, M., Le Blanc, K., Mueller, I., Slaper-Cortenbach, I., Marini, F., Krause, D., Deans, R., Keating, A., Prockop, D., and Horwitz, E., "Minimal criteria for defining multipotent mesenchymal stromal cells. The International Society for Cellular Therapy position statement.," *Cytotherapy*, vol. 8, no. 4, pp. 315–317, 2006.

[42] Dua, H. S. and Azuara-Blanco, A., "Limbal stem cells of the corneal epithelium," *Survey of ophthalmology*, vol. 44, no. 5, pp. 415–425, 2000.

[43] Eckersley-Maslin, M. A., Bergmann, J. H., Lazar, Z., and Spector, D. L., "Lamin A/C is expressed in pluripotent mouse embryonic stem cells.," *Nucleus (Austin, Tex.)*, vol. 4, pp. 53–60, Jan. 2013.

[44] Efremov, Y. M., Dokrunova, A. A., Bagrov, D. V., Kudryashova, K. S., Sokolova, O. S., and Shaitan, K. V., "The effects of confluency on cell mechanical properties.," *Journal of Biomechanics*, vol. 46, pp. 1081–1087, Apr. 2013.

[45] Eijssen, L. M. T., Jaillard, M., Adriaens, M. E., Gaj, S., de Groot, P. J., Müller, M., and Evelo, C. T., "User-friendly solutions for microarray quality control and pre-processing on ArrayAnalysis.org.," *Nucleic Acids Research*, vol. 41, pp. W71–76, July 2013.

[46] Engler, A. J., Sen, S., Sweeney, H. L., and Discher, D. E., "Matrix elasticity directs stem cell lineage specification.," *Cell*, vol. 126, pp. 677–689, Aug. 2006.

[47] Enver, T., Pera, M., Peterson, C., and Andrews, P. W., "Stem cell states, fates, and the rules of attraction.," *Cell stem cell*, vol. 4, pp. 387–397, May 2009.

[48] Esnault, C., Stewart, A., Gualdrini, F., East, P., Horswell, S., Matthews, N., and Treisman, R., "Rho-actin signaling to the MRTF coactivators dominates the immediate transcriptional response to serum in fibroblasts.," *Genes & development*, vol. 28, pp. 943–958, May 2014.

[49] Esue, O., Tseng, Y., and Wirtz, D., "Alpha-actinin and filamin cooperatively enhance the stiffness of actin filament networks.," *PLoS ONE*, vol. 4, no. 2, p. e4411, 2009.

[50] Fallqvist, B., Fielden, M. L., Pettersson, T., Nordgren, N., Kroon, M., and Gad, A. K. B., "Experimental and computational assessment of F-actin influence in regulating cellular stiffness and relaxation behaviour of fibroblasts.," *Journal of the mechanical behavior of biomedical materials*, vol. 59, pp. 168–184, June 2016.

[51] Fletcher, D. A. and Mullins, R. D., "Cell mechanics and the cytoskeleton.," *Nature*, vol. 463, pp. 485–492, Jan. 2010.

[52] Fu, J., Wang, Y.-K., Yang, M. T., Desai, R. A., Yu, X., Liu, Z., and Chen, C. S., "Mechanical regulation of cell function with geometrically modulated elastomeric substrates.," *Nature methods*, vol. 7, pp. 733–736, Sept. 2010.

[53] Funderburgh, M. L., Funderburgh, M. L., Du, Y., Mann, M. M., SundarRaj, N., and Funderburgh, J. L., "PAX6 expression identifies progenitor cells for corneal keratocytes.," *FASEB journal : official publication of the Federation of American Societies for Experimental Biology*, vol. 19, pp. 1371–1373, Aug. 2005.

[54] Garca, A. J., Vega, M. D., and Boettiger, D., "Modulation of cell proliferation and differentiation through substrate-dependent changes in fibronectin conformation.," *Molecular biology of the cell*, vol. 10, pp. 785–798, Mar. 1999.

[55] Gerger, A., Bergthaler, P., and Smolle, J., "An automated method for the quantification and fractal analysis of immunostaining.," *Cellular oncology*, vol. 26, no. 3, pp. 125–134, 2004.

[56] Glas, A. S., Lijmer, J. G., Prins, M. H., Bonsel, G. J., and Bossuyt, P. M. M., "The diagnostic odds ratio: a single indicator of test performance.," *Journal of Clinical Epidemiology*, vol. 56, pp. 1129–1135, Nov. 2003.

[57] Golpanian, S., Schulman, I. H., Ebert, R. F., Heldman, A. W., DiFede, D. L., Yang, P. C., Wu, J. C., Bolli, R., Perin, E. C., Moyé, L., Simari, R. D., Wolf, A., and Hare, J. M., "Concise Review: Review and Perspective of Cell Dosage and Routes of Administration From Preclinical and Clinical Studies of Stem Cell Therapy for Heart Disease.," *Stem cells translational medicine*, vol. 5, pp. 186–191, Feb. 2016.

[58] González-Cruz, R. D. and Darling, E. M., "Adipose-derived stem cell fate is predicted by cellular mechanical properties," *Adipocyte*, vol. 2, no. 2, pp. 0–1, 2013.

[59] González-Cruz, R. D., Fonseca, V. C., and Darling, E. M., "Cellular mechanical properties reflect the differentiation potential of adipose-derived mesenchymal stem cells.," *Proceedings of the National Academy of Sciences of the United States of America*, vol. 109, pp. E1523–9, June 2012.

[60] Gossett, D. R., Henry, T. K., Lee, S. A., Ying, Y., Lindgren, A. G., Yang, O. O., Rao, J., Clark, A. T., and Di Carlo, D., "Hydrodynamic stretching of single cells for large population mechanical phenotyping," *Proceedings of the National Academy of Sciences of the United States of America*, vol. 109, no. 20, pp. 7630–7635, 2012.

[61] Graham, H. K., Hodson, N. W., Hoyland, J. A., Millward-Sadler, S. J., Garrod, D., Scothern, A., Griffiths, C. E. M., Watson, R. E. B., Cox, T. R., Erler, J. T., Trafford, A. W., and Sherratt, M. J., "Tissue section AFM: In situ ultrastructural imaging of native biomolecules.," *Matrix Biology*, vol. 29, pp. 254–260, May 2010.

[62] Granchi, D., Ochoa, G., Leonardi, E., Devescovi, V., Baglìo, S. R., Osaba, L., Baldini, N., and Ciapetti, G., "Gene expression patterns related to osteogenic differentiation of bone marrow-derived mesenchymal stem cells during ex vivo expansion.," *Tissue engineering. Part C, Methods*, vol. 16, pp. 511–524, June 2010.

[63] Guilak, F., Tedrow, J. R., and Burgkart, R., "Viscoelastic properties of the cell nucleus.," *Biochemical and Biophysical Research Communications*, vol. 269, pp. 781–786, Mar. 2000.

[64] Guvendiren, M. and Burdick, J. A., "Stiffening hydrogels to probe short- and long-term cellular responses to dynamic mechanics.," *Nature communications*, vol. 3, p. 792, 2012.

[65] Hammerick, K. E., Huang, Z., Sun, N., Lam, M. T., Prinz, F. B., Wu, J. C., Commons, G. W., and Longaker, M. T., "Elastic properties of induced pluripotent stem cells.," *Tissue Engineering Part A*, vol. 17, pp. 495–502, Feb. 2011.

[66] He, H. and Yiu, S. C., "Stem cell-based therapy for treating limbal stem cells deficiency: A review of different strategies.," *Saudi Journal of Ophthalmology*, vol. 28, pp. 188–194, July 2014.

[67] Heng, B. C., Cao, T., Haider, H. K., Wang, D. Z. M., Sim, E. K.-W., and Ng, S. C., "An overview and synopsis of techniques for directing stem cell differentiation in vitro.," *Cell and Tissue Research*, vol. 315, pp. 291–303, Mar. 2004.

[68] Hipfner, D. R., Mao, Q., Qiu, W., Leslie, E. M., Gao, M., Deeley, R. G., and Cole, S. P., "Monoclonal antibodies that inhibit the transport function of the 190-kDa multidrug resistance protein, MRP. Localization of their epitopes to the nucleotide-binding domains of the protein.," *The Journal of biological chemistry*, vol. 274, pp. 15420–15426, May 1999.

[69] Holland, E. J., Djalilian, A. R., and Schwartz, G. S., "Management of aniridic keratopathy with keratolimbal allograft: a limbal stem cell transplantation technique.," *Ophthalmology*, vol. 110, pp. 125–130, Jan. 2003.

[70] Hu, M., Wang, J., Zhao, H., Dong, S., and Cai, J., "Nanostructure and nanomechanics analysis of lymphocyte using AFM: from resting, activated to apoptosis.," *Journal of Biomechanics*, vol. 42, pp. 1513–1519, July 2009.

[71] Hughes, A. J. and Herr, A. E., "Microfluidic Western blotting," *Proceedings of the National Academy of Sciences of the United States of America*, vol. 109, no. 52, pp. 21450–21455, 2012.

[72] Hur, S. C., Brinckerhoff, T. Z., Walthers, C. M., Dunn, J. C. Y., and Di Carlo, D., "Label-free enrichment of adrenal cortical progenitor cells using inertial microfluidics.," *PLoS ONE*, vol. 7, no. 10, p. e46550, 2012.

[73] Hur, S. C., Henderson-MacLennan, N. K., McCabe, E. R. B., and Di Carlo, D., "Deformability-based cell classification and enrichment using inertial microfluidics.," *Lab on a Chip*, vol. 11, pp. 912–920, Mar. 2011.

[74] Hutter, J. L. and Bechhoefer, J., "Calibration of atomic-force microscope tips," *Review of Scientific Instruments*, vol. 64, p. 1868, 1993.

[75] Hwang, N. S., Zhang, C., Hwang, Y.-S., and Varghese, S., "Mesenchymal stem cell differentiation and roles in regenerative medicine.," *Wiley interdisciplinary reviews. Systems biology and medicine*, vol. 1, pp. 97–106, July 2009.

[76] Jones, T. R., Carpenter, A., and Golland, P., "Voronoi-Based Segmentation of Cells on Image Manifolds," in *Computer Vision for Biomedical Image Applications*, pp. 535–543, Berlin, Heidelberg: Springer Berlin Heidelberg, 2005.

[77] Joseph, A. and Powell-Richards, A., "Epithelial cell characteristics of cultured human limbal explants," *British journal of Ophthalmology*, vol. 88, pp. 393–398, 2004.

[78] Karlen, Y., McNair, A., Perseguers, S., Mazza, C., and Mermod, N., "Statistical significance of quantitative PCR.," *BMC bioinformatics*, vol. 8, no. 1, p. 131, 2007.

[79] Ketene, A. N., Roberts, P. C., Shea, A. A., Schmelz, E. M., and Agah, M., "Actin filaments play a primary role for structural integrity and viscoelastic response in cells.," *Integrative biology*, vol. 4, pp. 540–549, May 2012.

[80] Kinney, M. A., Saeed, R., and McDevitt, T. C., "Mesenchymal morphogenesis of embryonic stem cells dynamically modulates the biophysical microtissue niche.," *Scientific reports*, vol. 4, p. 4290, 2014.

[81] Kiss, R., Bock, H., Pells, S., Canetta, E., Adya, A. K., Moore, A. J., De Sousa, P., and Willoughby, N. A., "Elasticity of human embryonic stem cells as determined by atomic force microscopy.," *Journal of biomechanical engineering*, vol. 133, p. 101009, Oct. 2011.

[82] Kovac, B., Teo, J. L., Mäkelä, T. P., and Vallenius, T., "Assembly of non-contractile dorsal stress fibers requires alpha-actinin-1 and Rac1 in migrating and spreading cells.," *Journal of Cell Science*, vol. 126, pp. 263–273, Jan. 2013.

[83] Ksander, B. R., Kolovou, P. E., Wilson, B. J., Saab, K. R., Guo, Q., Ma, J., McGuire, S. P., Gregory, M. S., Vincent, W. J. B., Perez, V. L., Cruz-Guilloty, F., Kao, W. W. Y., Call, M. K., Tucker, B. A., Zhan, Q., Murphy, G. F., Lathrop, K. L., Alt, C., Mortensen, L. J., Lin, C. P., Zieske, J. D., Frank, M. H., and Frank, N. Y.,

"ABCB5 is a limbal stem cell gene required for corneal development and repair.," *Nature*, vol. 511, pp. 353–357, July 2014.

[84] Lam, W. A., Rosenbluth, M. J., and Fletcher, D. A., "Chemotherapy exposure increases leukemia cell stiffness.," *Blood*, vol. 109, pp. 3505–3508, Apr. 2007.

[85] Lammerding, J., Fong, L. G., Ji, J. Y., Reue, K., Stewart, C. L., Young, S. G., and Lee, R. T., "Lamins A and C but not lamin B1 regulate nuclear mechanics," *Journal of Biological Chemistry*, vol. 281, no. 35, pp. 25768–25780, 2006.

[86] Last, J. A., Thomasy, S. M., Croasdale, C. R., Russell, P., and Murphy, C. J., "Compliance profile of the human cornea as measured by atomic force microscopy.," *Micron (Oxford, England : 1993)*, vol. 43, pp. 1293–1298, Dec. 2012.

[87] Lee, W. C., Shi, H., Poon, Z., Nyan, L. M., Kaushik, T., Shivashankar, G. V., Chan, J. K. Y., Lim, C. T., Han, J., and Van Vliet, K. J., "Multivariate biophysical markers predictive of mesenchymal stromal cell multipotency.," *Proceedings of the National Academy of Sciences of the United States of America*, vol. 111, pp. E4409–18, Oct. 2014.

[88] Liberio, M. S., Sadowski, M. C., Soekmadji, C., Davis, R. A., and Nelson, C. C., "Differential effects of tissue culture coating substrates on prostate cancer cell adherence, morphology and behavior.," *PLoS ONE*, vol. 9, no. 11, p. e112122, 2014.

[89] Lulevich, V., Shih, Y.-P., Lo, S. H., and Liu, G.-Y., "Cell tracing dyes significantly change single cell mechanics.," *The Journal of Physical Chemistry B*, vol. 113, pp. 6511–6519, May 2009.

[90] Maciaszek, J. L. and Lykotrafitis, G., "Sickle cell trait human erythrocytes are significantly stiffer than normal," *Journal of Biomechanics*, vol. 44, pp. 657–661, Feb. 2011.

[91] Mader, E. K., Butler, G., Dowdy, S. C., Mariani, A., Knutson, K. L., Federspiel, M. J., Russell, S. J., Galanis, E., Dietz, A. B., and Peng, K.-W., "Optimizing patient derived mesenchymal stem cells as virus carriers for a phase I clinical trial in ovarian cancer.," *Journal of translational medicine*, vol. 11, p. 20, 2013.

[92] Maloney, J. M., Nikova, D., Lautenschläger, F., Clarke, E., Langer, R., Guck, J., and Van Vliet, K. J., "Mesenchymal stem cell mechanics from the attached to the suspended state.," *Biophysical Journal*, vol. 99, pp. 2479–2487, Oct. 2010.

[93] Matsuura, K., Masuda, S., Haraguchi, Y., Yasuda, N., Shimizu, T., Hagiwara, N., Zandstra, P. W., and Okano, T., "Creation of mouse embryonic stem cell-derived cardiac cell sheets.," *Biomaterials*, vol. 32, pp. 7355–7362, Oct. 2011.

[94] Meyer-Blazejewska, E. A., Kruse, F. E., Bitterer, K., Meyer, C., Hofmann-Rummelt, C., Wünsch, P. H., and Schlötzer-Schrehardt, U., "Preservation of the limbal stem cell phenotype by appropriate culture techniques.," *Investigative ophthalmology & visual science*, vol. 51, pp. 765–774, Feb. 2010.

[95] Milani, P., Mirabet, V., Cellier, C., Rozier, F., Hamant, O., Das, P., and Boudaoud, A., "Matching Patterns of Gene Expression to Mechanical Stiffness at Cell Resolution through Quantitative Tandem Epifluorescence and Nanoindentation.," *Plant physiology*, vol. 165, pp. 1399–1408, June 2014.

[96] Mockers, O., Deroze, D., and Camps, J., "Cytotoxicity of orthodontic bands, brackets and archwires in vitro.," *Dental materials : official publication of the Academy of Dental Materials*, vol. 18, pp. 311–317, June 2002.

[97] Moers, K., Steinberg, T., Schlunck, G., Reinhard, T., Tomakidi, P., and Eberwein, P., "Substrate elasticity as biomechanical modulator of tissue homeostatic parameters in corneal keratinocytes.," *Experimental Cell Research*, vol. 319, pp. 1889–1901, July 2013.

[98] Murray, P., Prewitz, M., Hopp, I., Wells, N., Zhang, H., Cooper, A., Parry, K. L., Short, R., Antoine, D. J., and Edgar, D., "The self-renewal of mouse embryonic stem cells is regulated by cell-substratum adhesion and cell spreading.," *The international journal of biochemistry & cell biology*, vol. 45, pp. 2698–2705, Nov. 2013.

[99] O'Connor, M. D., Kardel, M. D., and Eaves, C. J., "Functional assays for human embryonic stem cell pluripotency.," *Methods in molecular biology (Clifton, N.J.)*, vol. 690, pp. 67–80, 2011.

[100] O'Connor, M. D., Kardel, M. D., Iosfina, I., Youssef, D., Lu, M., Li, M. M., Vercauteren, S., Nagy, A., and Eaves, C. J., "Alkaline phosphatase-positive colony formation is a sensitive, specific, and quantitative indicator of undifferentiated human embryonic stem cells.," *Stem Cells*, vol. 26, pp. 1109–1116, May 2008.

[101] Ofek, G., Willard, V. P., Koay, E. J., Hu, J. C., Lin, P., and Athanasiou, K. A., "Mechanical characterization of differentiated human embryonic stem cells.," *Journal of biomechanical engineering*, vol. 131, p. 061011, June 2009.

[102] Ojala, P. J., Paavilainen, V. O., Vartiainen, M. K., Tuma, R., Weeds, A. G., and Lappalainen, P., "The two ADF-H domains of twinfilin

play functionally distinct roles in interactions with actin monomers.," *Molecular biology of the cell*, vol. 13, pp. 3811–3821, Nov. 2002.

[103] Oldershaw, R. A., "Cell sources for the regeneration of articular cartilage: the past, the horizon and the future.," *International journal of experimental pathology*, vol. 93, pp. 389–400, Dec. 2012.

[104] Otto, O., Rosendahl, P., Mietke, A., Golfier, S., Herold, C., Klaue, D., Girardo, S., Pagliara, S., Ekpenyong, A., Jacobi, A., Wobus, M., Töpfner, N., Keyser, U. F., Mansfeld, J., Fischer-Friedrich, E., and Guck, J., "Real-time deformability cytometry: on-the-fly cell mechanical phenotyping.," *Nature methods*, vol. 12, pp. 199–202, Mar. 2015.

[105] Özvegy-Laczka, C., Várady, G., Köblös, G., Ujhelly, O., Cervenak, J., Schuetz, J. D., Sorrentino, B. P., Koomen, G.-J., Váradi, A., Német, K., and Sarkadi, B., "Function-dependent conformational changes of the ABCG2 multidrug transporter modify its interaction with a monoclonal antibody on the cell surface.," *The Journal of biological chemistry*, vol. 280, pp. 4219–4227, Feb. 2005.

[106] Pajerowski, J. D., Dahl, K. N., Zhong, F. L., Sammak, P. J., and Discher, D. E., "Physical plasticity of the nucleus in stem cell differentiation.," *Proceedings of the National Academy of Sciences of the United States of America*, vol. 104, pp. 15619–15624, Oct. 2007.

[107] Parot, P., Dufrêne, Y. F., Hinterdorfer, P., Le Grimellec, C., Navajas, D., Pellequer, J.-L., and Scheuring, S., "Past, present and future of atomic force microscopy in life sciences and medicine.," *Journal of molecular recognition*, vol. 20, pp. 418–431, Nov. 2007.

[108] Pellegrini, G., Dellambra, E., Golisano, O., Martinelli, E., Fantozzi, I., Bondanza, S., Ponzin, D., McKeon, F., and De Luca, M., "p63 identifies keratinocyte stem cells.," *Proceedings of the National Academy of Sciences*, vol. 98, pp. 3156–3161, Mar. 2001.

[109] Pellegrini, G., Pellegrini, G., Traverso, C. E., Traverso, C. E., Franzi, A. T., Franzi, A. T., Zingirian, M., Zingirian, M., Cancedda, R., Cancedda, R., De Luca, M., and De Luca, M., "Long-term restoration of damaged corneal surfaces with autologous cultivated corneal epithelium.," *Lancet (London, England)*, vol. 349, pp. 990–993, Apr. 1997.

[110] Pellegrini, G., Rama, P., Matuska, S., Lambiase, A., Bonini, S., Pocobelli, A., Colabelli, R. G., Spadea, L., Fasciani, R., Balestrazzi, E., Vinciguerra, P., Rosetta, P., Tortori, A., Nardi, M., Gabbriellini, G., Traverso, C. E., Macaluso, C., Losi, L., Percesepe, A., Venturi, B., Corradini, F., Panaras, A., Di Rocco, A., Guatelli, P., and De Luca, M., "Biological parameters determining the

clinical outcome of autologous cultures of limbal stem cells.," *Regenerative medicine*, vol. 8, pp. 553–567, Sept. 2013.

[111] Philipp, E., Jiri, N., and Günther, S., "Nanoindentation derived Mechanical Properties of the Corneoscleral Rim of the Human Eye.," *Key Engineering Materials*, vol. 606, pp. 117–120, 2014.

[112] Pillarisetti, A., Desai, J. P., Ladjal, H., Schiffmacher, A., Ferreira, A., and Keefer, C. L., "Mechanical phenotyping of mouse embryonic stem cells: increase in stiffness with differentiation.," *Cellular reprogramming*, vol. 13, pp. 371–380, Aug. 2011.

[113] Piruska, A., Nikcevic, I., Lee, S. H., Ahn, C., Heineman, W. R., Limbach, P. A., and Seliskar, C. J., "The autofluorescence of plastic materials and chips measured under laser irradiation.," *Lab on a Chip*, vol. 5, pp. 1348–1354, Dec. 2005.

[114] Platt, M. O., Wilder, C. L., Wells, A., Griffith, L. G., and Lauffenburger, D. A., "Multipathway kinase signatures of multipotent stromal cells are predictive for osteogenic differentiation: tissue-specific stem cells.," *Stem Cells*, vol. 27, pp. 2804–2814, Nov. 2009.

[115] Rama, P., Matuska, S., Paganoni, G., Spinelli, A., De Luca, M., and Pellegrini, G., "Limbal stem-cell therapy and long-term corneal regeneration.," *The New England journal of medicine*, vol. 363, pp. 147–155, July 2010.

[116] Rico, F., Chu, C., Abdulreda, M. H., Qin, Y., and Moy, V. T., "Temperature modulation of integrin-mediated cell adhesion.," *Biophysical Journal*, vol. 99, pp. 1387–1396, Sept. 2010.

[117] Rodríguez, J. P., González, M., Rios, S., and Cambiazo, V., "Cytoskeletal organization of human mesenchymal stem cells (MSC) changes during their osteogenic differentiation.," *Journal of Cellular Biochemistry*, vol. 93, pp. 721–731, Nov. 2004.

[118] Romano, A. C., Espana, E. M., Yoo, S. H., Budak, M. T., Wolosin, J. M., and Tseng, S. C. G., "Different cell sizes in human limbal and central corneal basal epithelia measured by confocal microscopy and flow cytometry.," *Investigative ophthalmology & visual science*, vol. 44, pp. 5125–5129, Dec. 2003.

[119] Rowat, A. C., Lammerding, J., Herrmann, H., and Aebi, U., "Towards an integrated understanding of the structure and mechanics of the cell nucleus.," *BioEssays : news and reviews in molecular, cellular and developmental biology*, vol. 30, pp. 226–236, Mar. 2008.

[120] Rubin, H., "Cell aging in vivo and in vitro.," *Mechanisms of ageing and development*, vol. 98, pp. 1–35, Oct. 1997.

[121] Ruijter, J. M., Ramakers, C., Hoogaars, W. M. H., Karlen, Y., Bakker, O., van den Hoff, M. J. B., and Moorman, A. F. M., "Amplification efficiency: linking baseline and bias in the analysis of quantitative PCR data.," *Nucleic Acids Research*, vol. 37, p. e45, Apr. 2009.

[122] Ruijter, J. M., Lorenz, P., Tuomi, J. M., Hecker, M., and van den Hoff, M. J. B., "Fluorescent-increase kinetics of different fluorescent reporters used for qPCR depend on monitoring chemistry, targeted sequence, type of DNA input and PCR efficiency.," *Mikrochimica acta*, vol. 181, no. 13-14, pp. 1689–1696, 2014.

[123] Sader, J. E., Larson, I., and Mulvaney, P., "Method for the calibration of atomic force microscope cantilevers," *Review of Scientific Instruments*, vol. 66, no. 7, pp. 3789–3798, 1995.

[124] Schlötzer-Schrehardt, U. and Kruse, F. E., "Identification and characterization of limbal stem cells.," *Experimental eye research*, vol. 81, pp. 247–264, Sept. 2005.

[125] Schriebl, K., Lim, S., Choo, A., Tscheliessnig, A., and Jungbauer, A., "Stem cell separation: a bottleneck in stem cell therapy.," *Biotechnology journal*, vol. 5, pp. 50–61, Jan. 2010.

[126] Shaharuddin, B., Harvey, I., Ahmad, S., Ali, S., and Meeson, A., "Characterisation of human limbal side population cells isolated using an optimised protocol from an immortalised epithelial cell line and primary limbal cultures.," *Stem cell reviews*, vol. 10, pp. 240–250, Apr. 2014.

[127] Shen, Z. L., Kahn, H., Ballarini, R., and Eppell, S. J., "Viscoelastic properties of isolated collagen fibrils.," *Biophysical Journal*, vol. 100, pp. 3008–3015, June 2011.

[128] Singh, A., Suri, S., Lee, T., Chilton, J. M., Cooke, M. T., Chen, W., Fu, J., Stice, S. L., Lu, H., McDevitt, T. C., and Garca, A. J., "Adhesion strength-based, label-free isolation of human pluripotent stem cells.," *Nature methods*, vol. 10, pp. 438–444, May 2013.

[129] Soleimani, M. and Nadri, S., "A protocol for isolation and culture of mesenchymal stem cells from mouse bone marrow.," *Nature Protocols*, vol. 4, no. 1, pp. 102–106, 2009.

[130] Solon, J., Levental, I., Sengupta, K., Georges, P. C., and Janmey, P. A., "Fibroblast adaptation and stiffness matching to soft elastic substrates.," *Biophysical Journal*, vol. 93, pp. 4453–4461, Dec. 2007.

[131] Sommer, C., Straehle, C., Kothe, U., and Hamprecht, F. A., "ilastik: Interactive learning and segmentation toolkit," in *8th IEEE International Symposium on Biomedical Imaging (ISBI 2011)*, pp. 230–233, IEEE, 2011.

[132] Sordel, T., Kermarec-Marcel, F., Garnier-Raveaud, S., Glade, N., Sauter-Starace, F., Pudda, C., Borella, M., Plissonnier, M., Chatelain, F., Bruckert, F., and Picollet-D'hahan, N., "Influence of glass and polymer coatings on CHO cell morphology and adhesion.," *Biomaterials*, vol. 28, pp. 1572–1584, Mar. 2007.

[133] Stewart, M. H., Bossé, M., Chadwick, K., Menendez, P., Bendall, S. C., and Bhatia, M., "Clonal isolation of hESCs reveals heterogeneity within the pluripotent stem cell compartment.," *Nature methods*, vol. 3, pp. 807–815, Oct. 2006.

[134] Stewart, Morag H, Bossé, Marc, Chadwick, Kristin, Menendez, Pablo, Bendall, Sean C, and Bhatia, Mickie, "Clonal isolation of hESCs reveals heterogeneity within the pluripotent stem cell compartment," *Nature methods*, vol. 3, no. 10, pp. 807–815, 2006.

[135] Subramanian, A., Tamayo, P., Mootha, V. K., Mukherjee, S., Ebert, B. L., Gillette, M. A., Paulovich, A., Pomeroy, S. L., Golub, T. R., Lander, E. S., and Mesirov, J. P., "Gene set enrichment analysis: a knowledge-based approach for interpreting genome-wide expression profiles.," *Proceedings of the National Academy of Sciences of the United States of America*, vol. 102, pp. 15545–15550, Oct. 2005.

[136] Suresh, S., "Biomechanics and biophysics of cancer cells.," *Acta Biomaterialia*, vol. 3, pp. 413–438, July 2007.

[137] Swift, J., Ivanovska, I. L., Buxboim, A., Harada, T., Dingal, P. C. D. P., Pinter, J., Pajerowski, J. D., Spinler, K. R., Shin, J.-W., Tewari, M., Rehfeldt, F., Speicher, D. W., and Discher, D. E., "Nuclear lamin-A scales with tissue stiffness and enhances matrix-directed differentiation.," *Science*, vol. 341, p. 1240104, Aug. 2013.

[138] Tan, D., Ficker, L. A., and Buckley, R. J., "Limbal transplantation," *Ophthalmology*, vol. 103, no. 1, pp. 29–36, 1996.

[139] Tan, Y., Kong, C.-w., Chen, S., Cheng, S. H., Li, R. A., and Sun, D., "Probing the mechanobiological properties of human embryonic stem cells in cardiac differentiation by optical tweezers.," *Journal of Biomechanics*, vol. 45, pp. 123–128, Jan. 2012.

[140] Tasadduq, B., Wang, G., El Banani, M., Mao, W., Lam, W., Alexeev, A., and Sulchek, T., "Three-dimensional particle tracking in microfluidic channel flow using in and out of focus diffraction," *Flow Measurement and Instrumentation*, vol. 45, pp. 218–224, Oct. 2015.

[141] Tee, S. Y., Fu, J., Chen, C. S., and Janmey, P., "Cell shape and substrate rigidity both regulate cell stiffness.," *Biophysical Journal*, vol. 100, pp. L25–L27, Mar. 2011.

[142] Titushkin, I. and Cho, M., "Modulation of cellular mechanics during osteogenic differentiation of human mesenchymal stem cells.," *Biophysical Journal*, vol. 93, pp. 3693–3702, Nov. 2007.

[143] Trapnell, C., Cacchiarelli, D., Grimsby, J., Pokharel, P., Li, S., Morse, M., Lennon, N. J., Livak, K. J., Mikkelsen, T. S., and Rinn, J. L., "The dynamics and regulators of cell fate decisions are revealed by pseudotemporal ordering of single cells.," *Nature biotechnology*, vol. 32, pp. 381–386, Apr. 2014.

[144] Treiser, M. D., Yang, E. H., Gordonov, S., Cohen, D. M., Androulakis, I. P., Kohn, J., Chen, C. S., and Moghe, P. V., "Cytoskeleton-based forecasting of stem cell lineage fates.," *Proceedings of the National Academy of Sciences of the United States of America*, vol. 107, pp. 610–615, Jan. 2010.

[145] Trickey, W. R., Vail, T. P., and Guilak, F., "The role of the cytoskeleton in the viscoelastic properties of human articular chondrocytes," *Journal of Orthopaedic Research*, vol. 22, pp. 131–139, 2004.

[146] Truong, T. T., Huynh, K., Nakatsu, M. N., and Deng, S. X., "SSEA4 is a potential negative marker for the enrichment of human corneal epithelial stem/progenitor cells.," *Investigative ophthalmology & visual science*, vol. 52, pp. 6315–6320, Aug. 2011.

[147] Tseng, S. C., "Concept and application of limbal stem cells.," *Eye (London, England)*, vol. 3 (Pt 2), pp. 141–157, 1989.

[148] Tsuji, Y., Yoshimura, N., Aoki, H., Sharov, A. A., Ko, M. S. H., Motohashi, T., and Kunisada, T., "Maintenance of undifferentiated mouse embryonic stem cells in suspension by the serum- and feeder-free defined culture condition," *Developmental Dynamics*, vol. 237, pp. 2129–2138, Aug. 2008.

[149] Tuomi, J. M., Voorbraak, F., Jones, D. L., and Ruijter, J. M., "Bias in the Cq value observed with hydrolysis probe based quantitative PCR can be corrected with the estimated PCR efficiency value.," *Methods*, vol. 50, pp. 313–322, Apr. 2010.

[150] Tusher, V. G., Tibshirani, R., and Chu, G., "Significance analysis of microarrays applied to the ionizing radiation response.," *Proceedings of the National Academy of Sciences of the United States of America*, vol. 98, pp. 5116–5121, Apr. 2001.

[151] Vandesompele, J., De Preter, K., Pattyn, F., Poppe, B., Van Roy, N., De Paepe, A., and Speleman, F., "Accurate normalization of real-time quantitative RT-PCR data by geometric averaging of multiple internal control genes.," *Genome biology*, vol. 3, p. RESEARCH0034, June 2002.

[152] Vater, C., Kasten, P., and Stiehler, M., "Culture media for the differentiation of mesenchymal stromal cells.," *Acta Biomaterialia*, vol. 7, pp. 463–477, Feb. 2011.

[153] Wagner, O., Zinke, J., Dancker, P., and Grill, W., "Viscoelastic properties of f-actin, microtubules, f-actin/α-actinin, and f-actin/hexokinase determined in microliter volumes with a novel nondestructive method," *Biophysical Journal*, vol. 76, no. 5, pp. 2784–2796, 1999.

[154] Wang, G., *Microfluidic Cell Separation based on Cell Stiffness*. PhD thesis, Georgia Institute of Technology, Atlanta, GA, Feb. 2015.

[155] Wang, G., Crawford, K., Turbyfield, C., Lam, W., Alexeev, A., and Sulchek, T., "Microfluidic cellular enrichment and separation through differences in viscoelastic deformation.," *Lab on a Chip*, vol. 15, pp. 532–540, Jan. 2015.

[156] Wang, G., Mao, W., Byler, R., Patel, K., Henegar, C., Alexeev, A., and Sulchek, T., "Stiffness dependent separation of cells in a microfluidic device.," *PLoS ONE*, vol. 8, no. 10, p. e75901, 2013.

[157] Wang, G., Turbyfield, C., Crawford, K., Alexeev, A., and Sulchek, T., "Cellular enrichment through microfluidic fractionation based on cell biomechanical properties," *Microfluidics and Nanofluidics*, vol. 19, pp. 987–993, June 2015.

[158] Willoughby, N. A., Bock, H., Hoeve, M. A., Pells, S., Williams, C., McPhee, G., Freile, P., Choudhury, D., and De Sousa, P. A., "A scalable label-free approach to separate human pluripotent cells from differentiated derivatives.," *Biomicrofluidics*, vol. 10, p. 014107, Jan. 2016.

[159] Xie, R., Everett, L. J., Lim, H.-W., Patel, N. A., Schug, J., Kroon, E., Kelly, O. G., Wang, A., D'Amour, K. A., Robins, A. J., Won, K.-J., Kaestner, K. H., and Sander, M., "Dynamic Chromatin Remodeling Mediated by Polycomb Proteins Orchestrates Pancreatic Differentiation of Human Embryonic Stem Cells.," *Cell stem cell*, Jan. 2013.

[160] Xu, J., Wirtz, D., and Pollard, T. D., "Dynamic cross-linking by alpha-actinin determines the mechanical properties of actin filament networks.," *The Journal of biological chemistry*, vol. 273, pp. 9570–9576, Apr. 1998.

[161] Xu, W. and Chahine, N., "Extreme hardening of PDMS thin films due to high compressive strain and confined thickness.," *Langmuir : the ACS journal of surfaces and colloids*, vol. 27, pp. 8470–8477, July 2011.

[162] Xu, W., Mezencev, R., Kim, B., Wang, L., and McDonald, J., "Cell stiffness is a biomarker of the metastatic potential of ovarian cancer cells," *PLoS ONE*, vol. 7, no. 10, p. e46609, 2012.

[163] Yang, C., Tibbitt, M. W., Basta, L., and Anseth, K. S., "Mechanical memory and dosing influence stem cell fate.," *Nature materials*, vol. 13, pp. 645–652, June 2014.

[164] Yeung, T., Georges, P. C., Flanagan, L. A., Marg, B., Ortiz, M., Funaki, M., Zahir, N., Ming, W., Weaver, V., and Janmey, P. A., "Effects of substrate stiffness on cell morphology, cytoskeletal structure, and adhesion.," *Cell motility and the cytoskeleton*, vol. 60, pp. 24–34, Jan. 2005.

[165] Yourek, G., Hussain, M. A., and Mao, J. J., "Cytoskeletal changes of mesenchymal stem cells during differentiation.," *ASAIO journal*, vol. 53, pp. 219–228, Feb. 2007.

[166] Yu, H., Tay, C. Y., Leong, W. S., Tan, S. C. W., Liao, K., and Tan, L. P., "Mechanical behavior of human mesenchymal stem cells during adipogenic and osteogenic differentiation.," *Biochemical and Biophysical Research Communications*, vol. 393, pp. 150–155, Feb. 2010.

[167] Zhang, C. and Xing, D., "Miniaturized PCR chips for nucleic acid amplification and analysis: latest advances and future trends.," *Nucleic Acids Research*, vol. 35, no. 13, pp. 4223–4237, 2007.

[168] Zhang, J., Rao, R. V., Spilman, P., Mangada, J., Xie, L., Vitelli, C., Gorostiza, O. F., Madden, D. T., Zeng, X., Jin, K., Hart, M. J., Bredesen, D. E., and Galvan, V., "Endogenously EGFP-Labeled Mouse Embryonic Stem Cells.," *Aging and disease*, vol. 2, pp. 18–29, Feb. 2011.